ÉCOLE CENTRALE LYON

N° d'ordre: 2013-15 Juillet 2013

THÈSE

présentée devant

L'ÉCOLE CENTRALE DE LYON
École Doctorale MEGA

en vue d'obtenir le titre de

DOCTEUR

par

Chiara Nironi

Concentration fluctuations of a passive scalar in a turbulent boundary layer

Soutenue le 2 Juillet 2013 devant la Commission d'Examen

Rapporteur: A. ROBINS

Rapporteur: F. ANSELMET

Directeur de thèse: R.J. PERKINS

Co-Directeur de thèse: P. SALIZZONI

President: J-N. GENCE

Examinateur: E. FERRERO

Abstract

This experimental study analyses the dynamics of concentration fluctuations in a passive plume emitted by a point source within the turbulent boundary layer. We aim to extend the popular study of Fackrell and Robins (1982) about concentration fluctuations and fluxes from point sources by including third and fourth moments of concentration. We also further inquire into the influence of source conditions, such as the source size, source elevation and emission velocity, on higher order concentration moments. The data set is completed by a detailed description of the velocity statistics within the TBL, with exhaustive information on both the temporal and spatial structure of the flow.

The experimental data-set has been used to test two different modeling approaches: an analytical meandering plume model (in one and in three dimensions) and a Lagrangian stochastic micro-mixing model.

Keywords: concentration fluctuations, concentration PDF, turbulent boundary layer, atmospheric dispersion, plume meandering model, Lagrangian stochastic model, micromixing

Résumé

Cette étude, menée principalement par des moyens expérimentaux, analyse la dynamique des fluctuations de concentration produites au sein d'un panache d'un scalaire passif émis par une source ponctuelle dans une couche limite turbulente. En étendant le travail de Fackrell and Robins (1982) sur les fluctuations de concentration, on décrit l'évolution des quatre premiers moments de la concentration et on étudie l'influence des conditions à la source (telles que la taille et la hauteur de la source et la vitesse de sortie) sur les moments mêmes. L'étude est complétée par une description détaillée des statistiques du champ de vitesse dans la couche limite, comprenant des informations sur la structure spatiale et temporelle de la turbulence.

Cette base de données expérimentale a été utilisée pour valider deux différentes approches à la modélisation de la dispersion: un modèle analytique de meandering et un modèle Lagrangien stochastique avec un schéma de micro mélange.

Mots clès: fluctuations de concentration, fonction densité de probabilité, couche limite atmosphérique, dispersion atmosphérique, modèle analytique de meandering, modèle Lagrangian stochastique, micro mélange

Remerciements

Je tiens à remercier mon directeur de thèse Richard Perkins pour m'avoir fait confiance tout au long de ces trois années. Je remercie Alan Robins et Fabien Anselmet, pour avoir accepté d'être rapporteurs de cette thèse et pour leurs précieux commentaires.

Merci à Pietro Salizzoni, le co-directeur de cette thèse, qui m'a tout appris de la dispersion atmosphérique et du monde de la recherche. On a beaucoup travaillé ensemble, merci Pietro pour ta patience et ton soutien à travers les haut et les bas que j'ai rencontré au long de cette aventure. Ce travail n'aurait jamais pu aboutir sans Patrick Méjean, qui a été mon maître dans le monde complexe de la mesure expérimentale. Merci Patrick pour ta gentillesse, ta patience et pour la compétence avec laquelle tu mènes ton travail. Je remercie Massimo Marro, c'est grâce à lui si j'ai beaucoup appris sur le traitement des données. Toutefois, son soutien et son amitié ont également été fondamentaux.

Je remercie toute l'équipe AIR du LMFA, qui m'a accueilli d'une façon chaleureuse dés le dèbut et dont je me suis toujours sentie aidée et à l'aise. En particulier je remercie Lionel Soulhac pour sa sagesse et ses explications toujours très claires. Merci à François-Xavier Cierco et à Guillevic Lamaison pour leur disponibilité. Merci à Natalie Grosjean, pour son aide et sa générosité.

Je remercie très chaleureusement mes compagnons Julien Le Clanche, Nabil Ben-Salem, Radi Sadek et Hervé Gamel, avec qui j'ai partagé les joies et les douleurs de la recherche et qui ont été ma famille centralienne. Merci aussi à Alexandre Pieri, Magdalena Neuhauser, Jorge Morales, Shyam Gopalakrishnan et aux autres doctorants du LMFA.

Contents

Chapter 1

INTRODUCTION

Considerable attention has been focused, in recent years, on the prediction of the Probability Density Functions (PDFs) of passive scalar concentration downwind a source of pollutant in the turbulent boundary layer. This is due to an increased interest in environmental problems, a more strict regulation about emissions in the atmosphere, the risk assessment of hazardous releases of toxic or flammable substances, and on problems related to odours.

When dealing with such issues, the knowledge of the concentration mean and standard deviation is not sufficient to predict peak concentrations, which requires information about higher order moments of the concentration PDF.

To these purposes several modelling approaches have been developed.

Between them, the most simples are analytical meandering models, whose conceptual framework was formulated by Gifford (1959), and that have been revised and generalised by many other authors (e.g. Sawford and Stapountzis (1986), Yee et al. (1994), Yee and Wilson (2000)).

In the family of Lagrangian stochastic models, two schemes were developed to model scalar fluctuations in plumes: two-particles models and micro-mixing models. A first model for the two-particles separation was proposed by Durbin (1980, 1982) whereas a more recent formulation was provided by Franzese and Borgas (2002). The rigorous applications of these models to calculate the full probability density function in a realistic atmosphere (not homogeneous) are still some way off (Sawford, 2004). This requires therefore the adoption of micro-mixing models, that are multi-particle models simulating the mass exchanges by molecular diffusion taking place between particles (Pope (1998), Sawford (2004), Cassiani et al. (2005a), Cassiani et al. (2007), Postma et al. (2011a)).

The Lagrangian stochastic models have been also used in coupling with meandering models for inhomogeneous anisotropic turbulence (Luhar et al. (2000), Franzese (2003)) or with hybrid Puff-particle models (De Haan and Rotach, 1998). In this case they are used to calculate the PDF due to the meandering motion of the plume mass centre, and a parametrisation is used for the plume relative dispersion.

The reliability of these models has however to be tested against field or experimental data providing a detailed description of concentration and velocity statistics. The motivation of our work is to provide a complete data-set describing the evolution of a fluctuating pollutant plume within the Turbulent Boundary Layer (TBL). We aim to extend the popular study of Fackrell and

Robins (1982a), about concentration fluctuations and fluxes from point sources by including measurements of concentration skewness and kurtosis. We also further inquire into the influence of source conditions, such as the source size, on higher order concentration moments. The data set is completed by a detailed description of the velocity statistics within the TBL, with exhaustive information on both the temporal and spatial structure of the flow.

The experimental data-set has been used to test two different modeling approaches: an analytical meandering plume model (in two and in three dimensions) and a Lagrangian stochastic micro-mixing model.

The thesis is divided in two parts: Measurements and Modelling. In the first part (Measurements) are reported experimental results for what concerns the investigation of the velocity and concentration fields, respectively in Chapter 2 and Chapter 3. In the second part (Modelling), the meandering plume model and a Lagrangian stochastic micro-mixing model are presented and compared with exprimental results, respectively in Chapters 4 and 5.

Part I

MEASUREMENTS

Chapter 2

THE VELOCITY FIELD

2.1 ABSTRACT

Understanding the effects of roughness on the turbulent boundary layer is of practical importance in the prediction of pollutant dispersion. The main purpose of this study is to describe accurately the turbulent boundary layer developed on a rough wall and to measure several quantities that are needed to parametrise turbulence in dispersion models. With this aim we have carried out detailed hot-wire anemometry and particle image velocimetry measurements within a turbulent boundary layer developing over a rough-wall. The velocity field description includes one-point velocity statistics, two-points spatial correlations, integral length scales, spectra, probability density functions, turbulent kinetic energy budget, Lagrangian time scales and turbulent diffusivities. Analogies and differences with previous experiments carried out by other authors are analysed and shortcomings of the similarity theory discussed.

2.2 INTRO

The study of Turbulent Boundary Layers (TBLs) has benefits for understanding the dynamics of atmospheric flows and their role in the dispersion of pollutants. Several experimental measurements in wind tunnel and on the terrain were realised to describe the structure of the turbulent boundary layer over a rough-wall and to identify the mechanisms responsible for substance dispersion. Universal aspects of flows over rough walls were discussed by Raupach et al. (1991) in his review of the theoretical and experimental knowledge of rough-wall TBLs.

Much of the recent literature concerns the effects of different types of roughness on the TBLs, since it has been suggested that the details of the wall may influence the flow across the whole boundary layer. The structure of TBLs which develop over rough and smooth walls was examined by Antonia et al. (1990) and Krogstad and Antonia (1994, 1999), who investigated the effects of the roughness on the velocity statistics, integral length scales and momentum absorption (Raupach et al., 2006). A review about differences between different types of roughness was written by Jimènez (2004). Salizzoni et al. (2008) studied the interaction between small- and large-scale roughness elements in different flow regimes. Measurements with new techniques as particle image velocimetry

and planar laser induced fluorescence were carried out over a two-dimensional rough-wall by Djenidi et al. (2008) and by Vesely et al. (2009).

Developed turbulent flows are similar in a generic sense, but the request of finding universal parameters is perfunctory satisfied. Based on the similarity theory, the TBL consists, in the simplest view, of an outer and an inner region. It is generally assumed that if a proper set of scales is chosen, each region can be described by some form of similarity solution.

In the outer region, where the surface boundary conditions are ignored, the flow is supposed to be in a state called "moving equilibrium" (Yaglom, 1979) with the boundary layer height (δ) and the friction velocity (u_*) varying sufficiently slowly stream-wise (x-direction), that their variation can be disregarded. Then both u_* and δ can be considered as local scales at any particular x.

In the inner region, the length scale for the flow close to the surface is the roughness length z_0, that depends on the size and orientation of the roughness elements. u_* is the only velocity scale, to which all velocity components are proportional. The bulk properties of the mean velocity distribution $\overline{u}(z)$ are derivable by a classical asymptotic matching process. Matching is a technique by which one requires that the outer and the inner layer similarities are identical in the double limit process $z/z_0 \to \infty$ (looking upwards from the surface layer) and $z/\delta \to 0$ (looking down towards the surface) (Tennekes, 1982). The result of this matching process is the familiar logarithmic law:

$$\frac{\overline{u}(z)}{u_*} = \frac{1}{k} ln \frac{z}{z_0}, \tag{2.1}$$

where k is the Von Karman constant ($k \simeq 0.4$). The overlap region where the two laws are valid is called inertial sublayer, in reference to the analogy with the inertial subrange in the turbulent kinetic energy spectrum. In this layer the wind shear $\partial\overline{u}/\partial z$ is independent of all lengths except the distance from the wall z. A crucial condition for the existence of the inertial sublayer is the separation between the outer and the inner length scales, so that $z_0 << \delta$.

According to the velocity defect law, the surface geometry is seen as a boundary condition only affecting the velocity distribution in the roughness region, of the order of a few roughness heights away from the wall. Further out, the flow characteristics are assumed to be independent of the surface geometry. Hence, flows at sufficiently high Reynolds number should lead to identical distributions of the non-dimensional velocity statistics (normalized by u_*) as function of z/δ, independently on the roughness of the surface, except very close to the wall (e.g. Hinze (1975), Townsend (1976)).

A wide number of experimental results indicate however that details of the wall roughness elements influence the flow across the whole boundary layer, providing experimental evidences of the shortcomings of the similarity theory. Krogstad and Antonia (1994) observed a relatively efficient transfer of information between the wall and the outer region of the turbulent boundary layer, so that the effects of the surface roughness on the mean velocity and on the turbulent stresses are not confined in the wall region, but influence the entire boundary layer. Large scale coherent structures, that are the main sources of Reynolds shear stress, appear to have higher average inclination and less longitudinal length compared to the smooth-wall case.

Krogstad and Antonia (1999) provided further evidence that the turbulent mixing properties are affected throughout the boundary layer by the surface ge-

ometry. They compared data from smooth surface and from two rough surfaces having the same effective hydrodynamic roughness but quite different geometries and length scales. Although mean velocity profiles were very similar in the three cases, suggesting that roughness effects are restricted to the wall region, the turbulent velocities presented important differences. Considerable effects of the surface conditions in the outer layer are found in the normal stress perpendicular to the wall, σ_w/u_*, and on the Reynolds stress $\overline{u'w'}/u_*^2$, while σ_u/u_* was only slightly affected.

Poggi et al. (2003) experimentally investigated the small scale turbulence and its degree of anisotropy and intermittency as a function of the wall distance, for smooth and rough wall conditions. They concluded that the interaction of the roughness with the organised motion near the wall induces a strong reduction of the levels of anisotropy and intermittency. Such differences in the turbulence structure were attributed to the injection of turbulent energy by the roughness elements in the flow near the wall.

These studies show that the adoption of similarity relations to depict the statistics of a turbulent boundary layer can induce to significant errors, especially for what concerns the structure of the larger scale motion. In wind tunnel experiments reproducing the atmospheric boundary layer another element of criticism is introduced, due to the vortex generators used to thicken the boundary layer and to accelerate its stream-wise development. Vortex generators fix the size of large scale structures (Robins, 1979). However, their interaction with the scales of turbulence is still unclear and we can not exclude that they could in some way modify the flow structure and in particular the transverse integral length scales.

When creating a data set dedicated to the validation of dispersion models, velocity statistics from experimental measurements should be as accurate as possible, to allow the models to reproduce the features of the velocity field. The main purpose of this study is to describe accurately the turbulent boundary layer developed on a rough wall and to discuss analogies and differences with experiments carried out in the past by other authors. Two measurement techniques were adopted, hot-wire anemometry and particle image velocimetry, to determine velocity statistics, two-points spatial correlations, integral length scales, spectra, triple correlations, probability density functions, turbulent kinetic energy budget. We also estimated the Lagrangian time scale and the turbulent diffusivity.

In what follows, our measurements are systematically compared to three data sets: Fackrell and Robins (1982a), hereafter referred to F&R, that represent the reference data set for the validation of pollutant dispersion models, Raupach et al. (1991) and Krogstad and Antonia (1994), that provide accurate description of velocity higher order statistics and of integral length scales. Two measurement techniques were adopted, hot-wire anemometry and particle image velocimetry, to determine velocity statistics, two-points spatial correlations, spectra, triple correlations, probability density functions, turbulent kinetic energy budget. Particular emphasis is put on the estimates of the integral length scales from two-point correlations of the three velocity components. From these we could infer information for the parametrisation of Lagrangian time scales and turbulent diffusivities.

2.3 EXPERIMENTAL METHODS

The experiments were performed in the atmospheric wind tunnel of the Laboratoire de Mécanique des Fluides et d'Acoustique de l'Ecole Centrale de Lyon, France. The flow dynamics above the obstacle array were investigated by means of hot wire anemometry, using an X-wire probe with a sampling frequency of 5000 Hz. Hot wire data provided information about the temporal evolution of the velocity. They were supported by a series of measurements with Stereo Particle Image Velocimetry (Stereo-PIV), which allowed a complete knowledge of the spatial variability of the velocity field.

2.3.1 Wind Tunnel set-up

The wind tunnel measures 24 m long, 7.4 m high and 7.2 m wide (Figure 2.3.1). The working section measures 14 m long, 2.5 m high and 3.7 m wide.

The aerodynamic circuit is composed by an axial fan driven by a direct current motor having a power of 50 kW (pression: $200Pa$, discharge: $100m^3/s$). The flow speed can be set continuously from 0.5 to 10 m/s. Flow straighteners are present downstream of the fan blades to remove the swirl generated by the fan. A heat exchanger system allows to adjust the air temperature in the test section with a precision of $\pm 0.5°$C. A converging system is placed before the entrance of the test section to force the incident wind flow to be approximately parallel to the test section centre line, and to increase the flow uniformity in the transverse direction. A diverging system is placed at the exit of the test section. Vanes are present in every elbow to bend the flow in each sharp turn. An upwind grid was placed at the entrance of the test section to generate homogeneous turbulence.

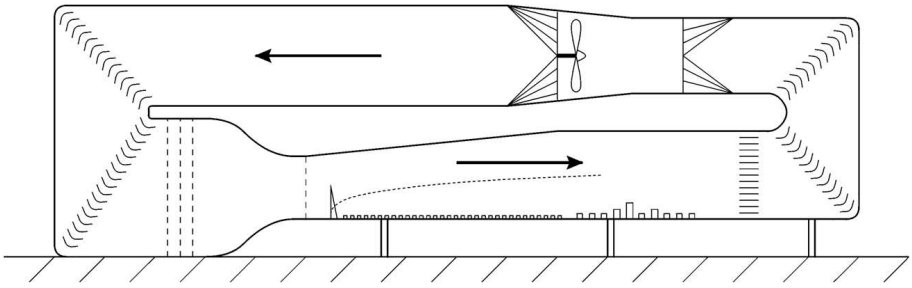

Figure 2.1: The atmospheric wind tunnel of the Laboratoire de Mécanique des Fluides et d'Acoustique de l'Ecole Centrale de Lyon, France.

In the wind tunnel, a neutrally stratified boundary layer was generated by combining the effect of a row of spires at the beginning of the test section and floor roughness elements (Irwin, 1981). The spires were of the Irwin type (Irwin, 1981) with a height of 0.5 m. Their role is to thicken the boundary layer accelerating the stream-wise development of the larger scale eddies. The entire working section floor was overlaid with cubes of side H=0.02 m distributed in rows which acted as roughness elements. These elements assured a production of turbulence near the floor. This experimental set-up allowed us to reproduce a boundary layer whose depth δ was approximately 0.8 m. The reference free-

stream velocity U_∞ at the boundary layer height was set at 5 m/s. The Reynolds number $Re = \delta U_\infty/\nu \approx 2.6 \cdot 10^5$ has a value which is generally assumed as sufficiently high to ensure the adequate simulation of a fully rough turbulent flow (Jimènez, 2004).

2.3.2 Hot Wire Anemometry

The velocity field above the obstacles array was investigated with a hot-wire anemometer equipped with a X-wire probe with a velocity-vector acceptance angle of $\pm 45°$. Longitudinal and transverse components of the velocity could be thus measured simultaneously. Several vertical and transverse profiles of velocity were recorded along the entire working section to completely characterise the flow in the TBL. For each measurement point 120 s time series were acquired with a sampling frequency of 5000 Hz.

The hot wire sensors are thin metallic wires made of platinum or tungsten heated by an electric current (Joule effect). The wires are cooled by the incident flow, which act by virtue of its mass flux and its temperature, through various effects, but with forced convection usually predominant (Comte-Bellot, 1976). The heat loss can be obtained by measuring the change in wire temperature under constant current, or the current required to maintain a constant wire temperature (or resistance). This loss is converted into a flow velocity in accordance with convective theory.

A constant-temperature anemometer was adopted. In this set-up the hot wire is included in a Wheatstone bridge, and the unbalance voltage is amplified and fed back to the bridge to suppress the resistance (and temperature) changes of the wire. This feedback signal represents the changes occurring in the flow variables. The advantages of constant-temperature anemometers were recognized at an early stage. A rapid variation in the heating current compensate for instantaneous changes in the flow velocity (Bruun, 1995), making this type of anemometers suitable for high turbulence intensity flows.

The X-wire probes and the anemometer used in this research are produced by Dantec Dynamics. Data acquisition was performed with a LabView routine. The calibration was carried out by exposing the probe to a set of known velocities and then recording the voltages. The points are fitted with a curve that represents the transfer function used to convert data records from voltages into velocities. The yaw coefficients are used in order to decompose the calibration velocities from the X-probe into the U and V components (Jorgensen, 2002). Calibration was carried out in the wind tunnel and a pitot-tube was used as velocity reference.

Errors are well known to affect turbulence measurements with hot-wire probes close to the surface due to the enhanced turbulence intensity (Castro and Dianat, 1990). These errors are responsible for the misbehavior in measuring Reynolds shear stress just above the roughness; the most obvious symptom is the decrease in the measured shear stress $\overline{uw}$ for vertical distances of the order of the obstacles height (Raupach et al., 1991). Error analysis on X-wire probes were made by Legg et al. (1984) and Perry et al. (1987). The main problem arising from these studies is the limited velocity-vector acceptance angle of $\pm 45°$ in a conventional X-wire probe. Perry et al. (1987) showed that acceptable Reynolds stress measurements can be obtained using a probe with an higher acceptance angle ($\pm 60°$) or a flying probe in the stream-wise direction to reduce

the turbulence intensity. Legg et al. (1984) and Smalley et al. (2001) suggested that, even using the usual $\pm 45°$, the velocity fluctuation measurements are reliable when the fluctuation intensity is smaller than 0.35 and the Reynolds stress measurements when the fluctuation intensity is minor than 0.25.

2.3.3 Particle Image Velocimetry

A second series of velocity measurements was made with a Stereo Particle Image Velocimetry (Stereo-PIV) system. This technique allows a high spatio-temporally resolved field description for the three velocity components. The Stereo-PIV measurements support with spatial information the temporal data acquired with hot-wire anemometry, and integral length scales can be inferred from spatial two-points correlations.

Particle Image Velocimetry (PIV) is an established non-intrusive optical technique for the measurement of flow velocities on a plane. The measuring principle consists of obtaining the velocity of a fluid by measuring the velocity of tracer particles in suspension (Raffel et al., 1998; Westerweel, 1997). The measuring volume is a small region within the fluid, where the flow is considered to be sufficiently uniform.

PIV requires the determination of particle displacements between two images separated by a time interval, which is typically of order of μs. Using the auto-correlation approach, image pairs are divided into small interrogation areas and the particle displacement is found as the location of a peak in the correlation map. Once the particle displacement is determined this is divided by the time-step between the two images resulting in a velocity (Lourenco and Krothapalli, 1995).

The fluid flow was seeded with nominally neutrally buoyant particles generated by a smog generator, so that the motion of the particles was representative of the motion of the fluid elements. A planar region of the flow was lighted with a pulsed laser and tracer position was recorded as a function of time in doubly exposure photographs.

Stereo-PIV profiles were collected at a distance of 7.5δ from the entrance of the test section, corresponding to the source position. Velocities were recorded on two planes: a yz plane perpendicular to the flow direction and a xz plane parallel to the flow, allowing the measurement of the stream-wise, transverse and vertical velocity components. The image resolution was 1280x1024 pixels and the observation field measured approximately 150x100 mm for xz planes and 215x150 mm for yz planes. In both cases several planes were recorded at different heights to cover the entire boundary layer height. Images were processed using a cross-correlation algorithm. The interrogation window for the correlation cells was fixed to 32x32 pixels with a round form and a standard 50% overlap, providing a spatial resolution of about 2 mm for xz planes and 2.5 mm for yz planes. A total set of 10000 image pairs was acquired sequentially for time-averaged computations. The sampling frequency was 4 Hz.

2.4 MEAN VELOCITY FIELD

As predicted by the similarity theory (Tennekes and Lumley, 1972), in the lower part of the boundary layer the vertical profile of mean horizontal velocity fits

well a logarithmic law. The only length scale is the distance from the ground z. Care is needed in defining the origin of z, since the roughness of the surface displaces the entire flow upwards. To account for this, the logarithmic law is written including the displacement height d:

$$\frac{\overline{u}(z)}{u_*} = \frac{1}{k} ln \left(\frac{z-d}{z_0} \right). \tag{2.2}$$

Thom (1971) found experimentally and Jackson (1981) verified theoretically that, whatever the origin of z, the displacement height adjusts the reference level for the velocity profile to the height at which the mean surface shear appears to act. This definition satisfies the constraint $0 < d < \delta$. Several techniques have been proposed for the measurement of the displacement height, as discussed briefly by Raupach et al. (1991). We chose to calculate d and the roughness height z_0 by fitting the log-law to a measured velocity profile, for a known value of u_*, determined from profiles of $\overline{u'w'}$.

The friction velocity u_* is the only relevant velocity scale in the TBL and depends on the nature of the surface and on the magnitude of the wind. Since the surface stress equals the turbulent momentum flux in the air just above the surface, u_* is in some sense representative of the turbulent wind fluctuations in the lower layers of the atmosphere (Kaimal and Finnigan, 1994). There exists various similar definitions of the friction velocity that were compared by Weber (1999). We chose the definition given by Panofsky and Dutton (1984), Garratt (1992) and Kaimal and Finnigan (1994), according to whom u_* is given by:

$$\tau_0 = -\rho\overline{u'w'} = \rho u_*^2, \tag{2.3}$$

where τ_0 is the surface stress at the roughness level $z = z_0$ and ρ is the density of air. This definition assumes that the horizontal Reynolds stress vector $(-\rho\overline{u'w'}, -\rho\overline{u'v'})$ reduces to $(-\rho\overline{u'w'}, 0)$ if the u-axis is aligned with the mean wind. In the atmosphere this is not true in general (Weber, 1999), however in the lower part of the boundary layer the quantity $\overline{u'v'}$ is very small compared to $\overline{u'w'}$ (Figure 2.2). Over the same distance, from $(z-d)/\delta \simeq 0$ to 0.2, $\overline{u'w'}$ varies so slowly that can be considered effectively constant: this identifies the constant stress layer.

	u_* (m/s)	z_0 (m)	d (m)
Method 1	0.185	$1.133 \cdot 10^{-4}$	0.0129
Method 2	0.2393	$5.848 \cdot 10^{-4}$	0

Table 2.1: Boundary layer parameters u_*, z_0 and d.

We estimated the boundary layer parameters in two ways, and the results are shown in Table 2.1. In the first way (Method 1), z_0 and d where computed by fitting the log-law to a measured mean velocity profile, assuming that $u_*^2 = \overline{u'w'}$. u_* was calculated by averaging the $\overline{u'w'}$ data in the lower part of the flow field. In the second way (Method 2), z_0 and u_* were obtained with the fit of the log-law to a mean velocity profile assuming that $d = 0$. In all cases, the fitting has to be applied to the velocity profile in the inertial region, as no theoretical basis supports the validity of the logarithmic law in the roughness sublayer.

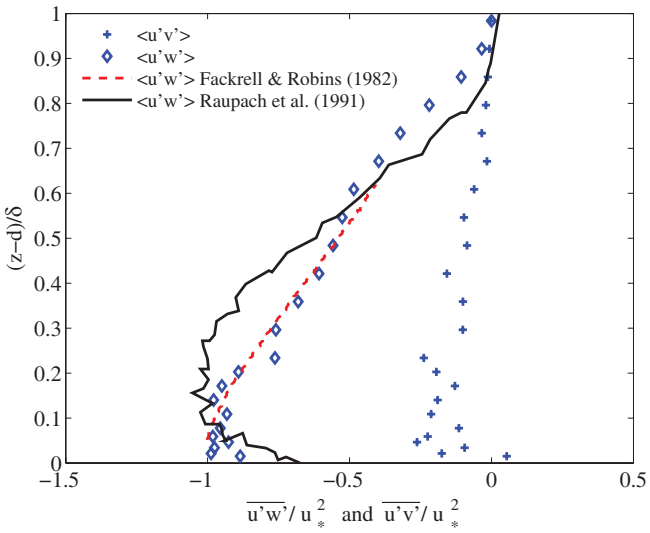

Figure 2.2: Measured $\overline{u'v'}$ and $\overline{u'w'}$ and comparison with literature data from Fackrell and Robins (1982b) and Raupach et al. (1991).

Parameters calculated with Method 1 will be the ones adopted from now on. The value of the friction velocity calculated with the first method is smaller than the one obtained with the second method. As it was observed from Weber (1999), the definition given in Equation 2.3 uses only the longitudinal component of the Reynolds stress vector and can lead to a slight underestimation of u_*.

	δ (m)	z_0/δ	u_*/U_∞
Present study	0.8	$7.31 \cdot 10^{-4}$	0.037
F&R	1.2	$2.4 \cdot 10^{-4}$	0.047

Table 2.2: Boundary layer characteristics: comparison with literature data from Fackrell and Robins (1982b), referred to as F&R in the Table.

A comparison with Fackrell and Robins (1982b) is given in Table 2.2. As predicted by the theory, and as shown in Figure 2.3, Equation 2.2, fits the velocity profile in a region that slightly exceeds the extent of the inertial region, for $0.025 \leq (z-d)/\delta \leq 0.25$. Conversely, a good fit of the mean velocity profile in the whole TBL extent can be obtained by a power law of the form:

$$\frac{\overline{u}(z)}{U_\infty} = \left(\frac{z-d}{\delta-d}\right)^n, \tag{2.4}$$

with the exponent $n = 0.21$.

The evolution of the boundary layer is shown in Figure 2.3, where vertical profiles of the non-dimensional mean stream-wise velocity $\overline{u}$ are plotted at different distances x/δ from the entrance of the wind tunnel. Profiles show that the boundary layer is slightly evolving in the stream-wise direction, particularly

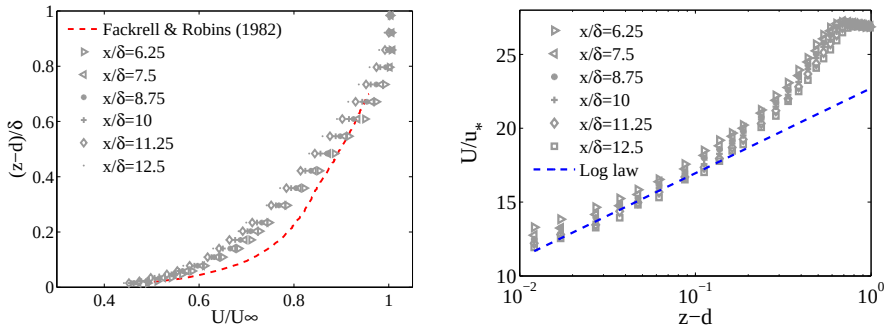

Figure 2.3: Vertical profiles of non-dimensional mean stream-wise velocity $\overline{u}$, comparison with literature data from Fackrell and Robins (1982b).

close to the entrance ($x/\delta < 7$) and the exit of the test section ($x/\delta > 12$), where the flow feels the presence of the converging/diverging systems. For this reason velocity measurements (as well as the concentration measurements presented in the second part of this study) where carried out in the central area of the wind gallery, starting from $x/\delta = 7.5$, where we considered the flow to be fully developed. Also, at this distance we assume that the development of coherent structures in the wake of the vortex generators has already reached an equilibrium condition (Salizzoni et al., 2008).

The profile of $\overline{u}/U_\infty$ is compared to data from F&R, in Figure 2.3a. The difference in the parameter z_0/δ can be the reason for the discrepancies that we observe between the curves, since the profile from F&R shows a higher mean gradient close to the wall, resulting in a higher ratio u_*/U_∞ (Table 2.2).

2.5 TURBULENT VELOCITY FIELD

A consequence of the similarity theory is that vertical profiles of single point velocity statistics should collapse to common curves when normalised with u_* and δ, independent of wall roughness. Figure 2.5 shows normalised profiles of $\overline{u'w'}$ and of the standard deviations $\sigma_u = (\overline{u'^2})^{1/2}$, $\sigma_v = (\overline{v'^2})^{1/2}$, $\sigma_w = (\overline{w'^2})^{1/2}$ at various distances downwind, measured with HWA and compared with experiments from Fackrell and Robins (1982b). Non-dimensional profiles of σ_w and $\overline{u'w'}$ collapse to common curves, while discrepancies are observed for σ_u and σ_v. Data were also compared to Raupach et al. (1991), whose measurements were made on a variety of surface roughness. Profiles of the standard deviations collapse, except in the inertial region, that extends close to the surface from $(z-d)/\delta \simeq 0$ to 0.2. Significant differences are found in the Reynolds stress profile all along the boundary layer.

The discrepancies that exist between these experiments can be due to three main reason. The first is the difference in the flow configuration that can result from the choice of the devices to thicken the boundary-layer, as for example the vortex generators. Such variations are expected to affect the largest scales of motion, of the order of the characteristic size and spacing of the thickening

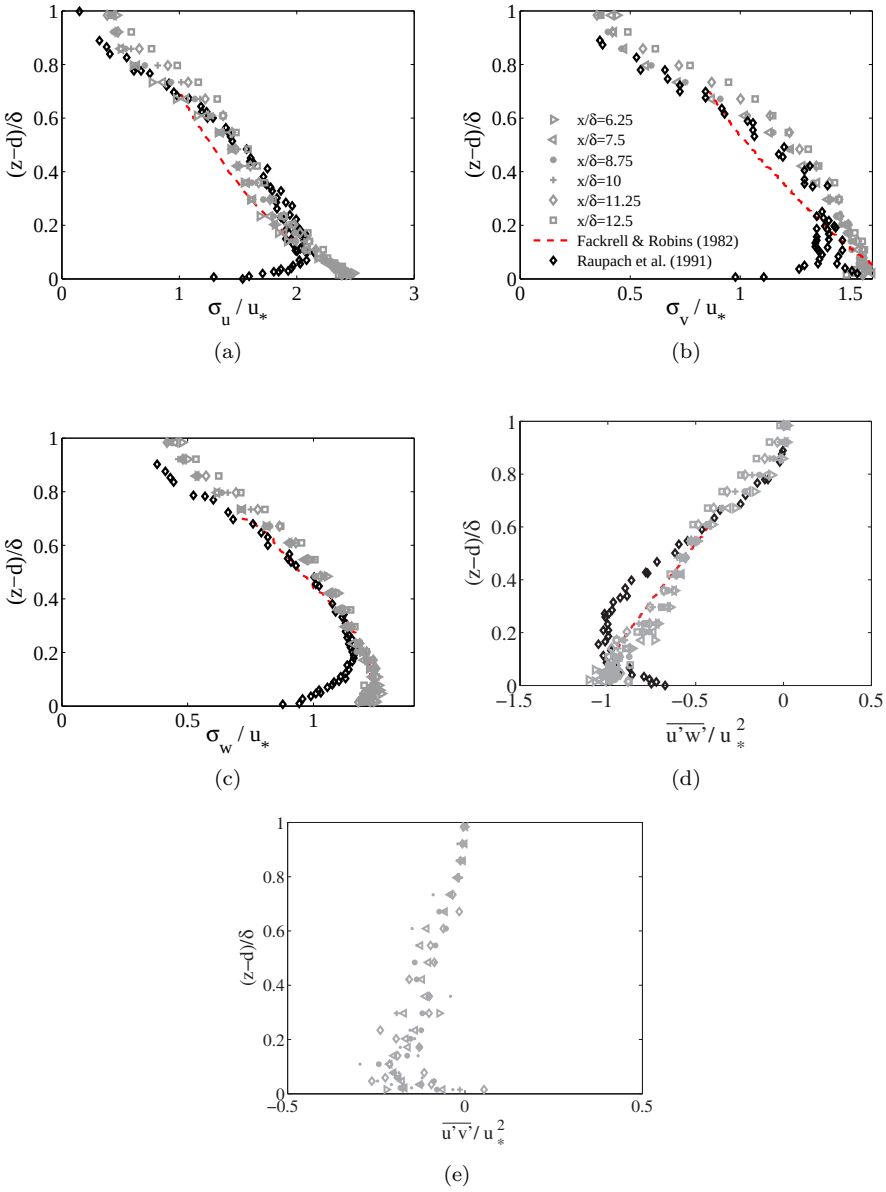

Figure 2.4: Velocity statistics from HWA measurements.

device, and hence the turbulent velocities in the outer layer. We can not exclude that such devices could in some way influence the scales of transverse and vertical fluctuating velocities. For this reason Raupach et al. (1991) suggested that the best approach is to compare measurements taken in the same experimental situation, provided that the large-scale flow geometry is held constant. The second cause of discrepancies are errors affecting turbulence measurements with X-wire probes close to a rough surface. The errors are responsible for the apparent decrease of $\overline{u'w'}$ and σ_w in the roughness sublayer, as can be observed in profiles from Raupach et al. (1991) and, with a minor extent, on our profiles of σ_w, $\overline{u'w'}$ and also on $\overline{u'v'}$. To make clear if there were such systematical errors in the HWA measurements, profiles were compared with Stereo-PIV measurements (Figure 2.5). Profiles of σ_u, σ_v and σ_w superpose, while Reynolds stresses from Stereo-PIV result higher than the ones measured with HWA. This is especially true for $\overline{u'w'}$, that however conserves the same shape of the HWA profile and apparently do not show any decrease near the surface. Such a decrease is instead evident in $\overline{u'v'}$, even though in this case comparisons are made difficult by the noise affecting the results. For what concerns the mean field, PIV measurements are little overestimating the corresponding HWA profile at $x/\delta = 7.5$, nevertheless they are included within the range of variation of HWA measurements. The third reason is connected with the differences in the wall roughness, that may alter the conditions of self-similarity, as demonstrated by Krogstad and Antonia (1994).

2.5.1 Turbulent kinetic energy budget

The turbulent kinetic energy budget in a boundary layer in steady conditions where the diffusive fluxes are neglected is:

$$-\frac{\partial}{\partial x_j}\left(\rho\overline{u}_j q^2\right) - \frac{\partial}{\partial x_j}\left(\frac{\rho}{2}\overline{u'_j u'_i u'_i}\right) - \frac{\partial}{\partial x_j}\overline{p u'_j} - \rho\overline{u'_i u'_j}\frac{\partial \overline{u}_i}{\partial x_j} - \varepsilon = 0, \qquad (2.5)$$

where $q^2 = (\sigma_u^2 + \sigma_v^2 + \sigma_w^2)/2$ is the turbulent kinetic energy, p is the fluctuating kinematic pressure and ε is the average energy dissipation rate. Tensor notation is used where convenient. The first term in Equation 2.5 is the advection term, the second is the transport by means of the fluctuating velocity, the third is the mechanical power transmitted by the pressure stress, the fourth is the production term and the last is the dissipation, defined as:

$$\varepsilon = \overline{\frac{\nu}{2}\left(\frac{\partial u'_i}{\partial x_j} + \frac{\partial u'_j}{\partial x_i}\right)^2}. \qquad (2.6)$$

In the hypothesis of homogeneity in the horizontal planes and considering the term $\frac{\partial}{\partial z}(\rho W q^2)$ to be negligible, since the vertical mean velocity $W \simeq 0$, the budget becomes:

$$-\frac{\partial}{\partial z}\left[\frac{\rho}{2}\left(\overline{w'u'u'} + \overline{w'v'v'} + \overline{w'w'w'}\right)\right] - \frac{\partial}{\partial z}\overline{pw'} - \rho\overline{u'w'}\frac{\partial \overline{u}}{\partial z} - \varepsilon = 0. \qquad (2.7)$$

In a zero-pressure gradient boundary layer with a slow stream-wise development, as in our case, it is generally assumed that an equilibrium layer exists near the surface in which the Reynolds stress is almost constant ($\overline{u'w'} = u_*^2$), as in

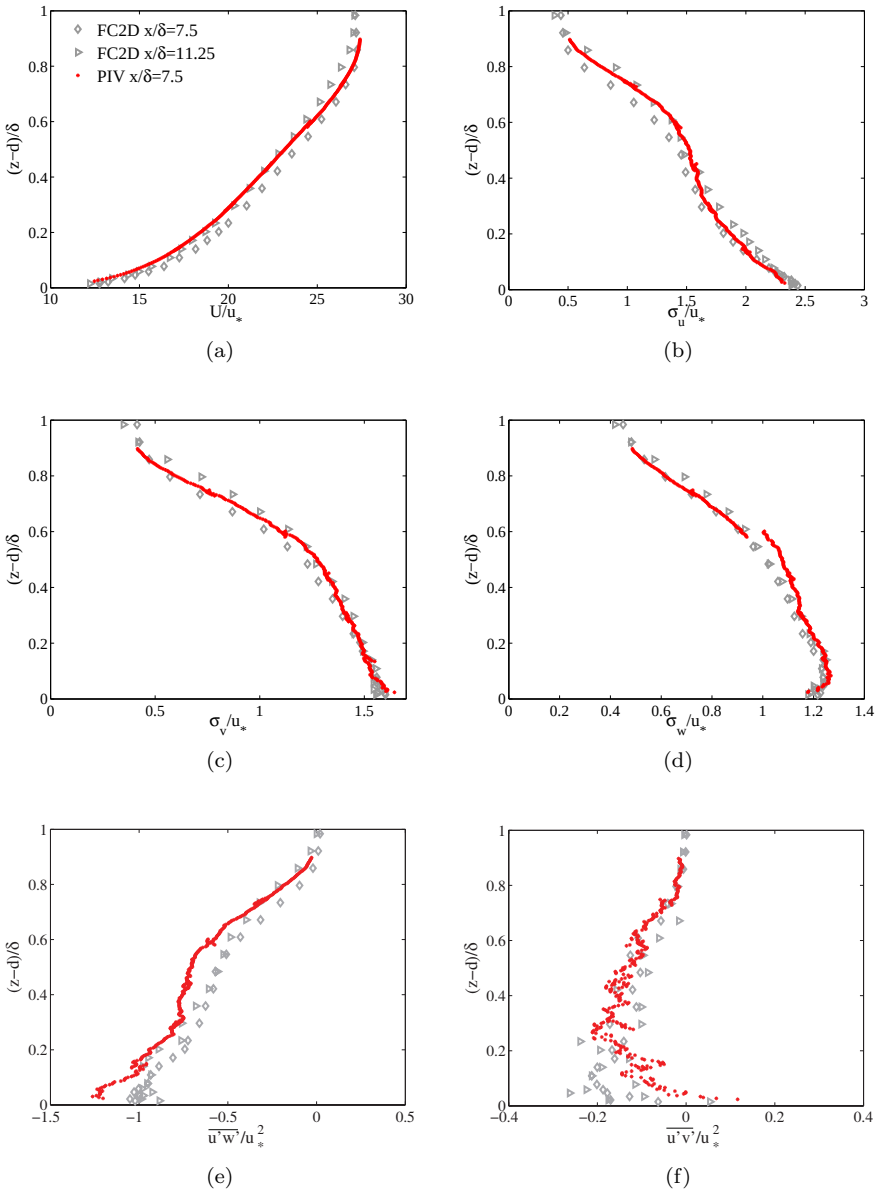

Figure 2.5: Comparison between velocity moments from HWA and Stereo-PIV measurements.

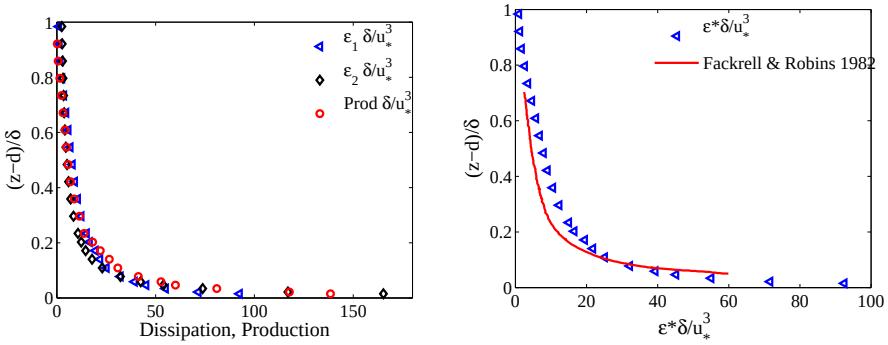

Figure 2.6: Dissipation and production of turbulent kinetic energy. (a) ε_1 is calculated through Equation 2.10, while ε_2 through Equation 2.11. (b) Comparison with Fackrell and Robins (1982b) of the non-dimensional vertical profile of dissipation.

(Figure 2.5e). The theory of the equilibrium layer was developed by Townsend (1976), who also specified two conditions that must be satisfied for the layer in order to be in local equilibrium. The first condition is that the equilibrium layer thickness must be much smaller than the boundary layer height δ, so that production and dissipation rates within it are independent of the large-scale flow geometry. The second condition is the equilibrium of the turbulent kinetic energy budget, that occurs when production and dissipation are so large that the other terms (transport by means of the fluctuating velocity and the mechanical power transmitted by the pressure stress) becomes negligible. Then Equation 2.7 reduces to:

$$\rho\overline{u'w'}\frac{\partial\overline{u}}{\partial z} + \varepsilon = 0. \tag{2.8}$$

The equality between production and dissipation in our measurements is shown in Figure 2.6a.

The direct measurement of ε is rather difficult as it requires the evaluation of the spatial gradients of the instantaneous velocity at a scale of the order of the dissipative Kolmogorov scale η, that is given by (Kaimal and Finnigan, 1994)

$$\eta = \left(\frac{\nu^3}{\varepsilon}\right)^{1/4}. \tag{2.9}$$

Such type of measurements were carried out with PIV in stirred vessels by Baldi and Yianneskis (2004) and Baldi et al. (2004). They state that a spatial resolution of 2η allows the measurement of the 90% of the energy dissipation, η being the Kolmogorov length scales, while the 65% can be measured with a resolution of 9η. Since our PIV measurements did not reach such a resolution, we calculated the dissipation with the common isotropic approximation (Hinze, 1975)

$$\varepsilon_1 = \frac{15\nu}{\overline{u}^2}\overline{\left(\frac{\partial u'^2}{\partial t}\right)}, \tag{2.10}$$

where $\nu = \mu/\rho$. This approximation employs Taylor's hypothesis of frozen turbulence to convert spatial gradients to temporal gradients, through the transformation $x = \overline{u}t$. Such hypothesis assumes that the eddies change imperceptibly as they are convected by the mean wind past the sensor.

Given the equilibrium layer constraints, from the dimensional analysis of Equation 2.8 follows another relation for the dissipation rate, based on u_* and $z - d$, the only relevant velocity and length scales:

$$\varepsilon_2 = \frac{u_*^3}{k(z-d)}. \tag{2.11}$$

It is worth noting that a priori the estimate of ε by means of Equation 2.10 is not straightforward, due to inadequacies of hot wire response. The good agreement shown in Figure 2.6a suggests though the reliability of this method in present case study.

Figure 2.6b shows the dissipation in the non-dimensional form, $\varepsilon\delta/u_*^3$, compared to the experiments of Fackrell and Robins (1982b). Even in this case we can observe an overall good agreement between the two estimates, even though the vertical gradient of ε shows slight differences both in the upper ($z/\delta > 0.15$) and in the lower part ($z/\delta < 0.15$) of the velocity field. Assuming a local equilibrium (Equation 2.8), since $\overline{u'w'}$ is substantially the same in the two experiments (Figure 2.4d), the difference in ε can be interpreted as due to a varying $\partial\overline{u}/\partial z$. As shown in Figure 2.3, compared to our results $\partial\overline{u}/\partial z$ is higher for F&R in the surface layer ($z/\delta < 0.15$) and lower for $z/\delta > 0.15$.

2.5.2 Velocity skewness and probability density functions

Third moments $\overline{w'w'w'}$ and $\overline{u'u'u'}$ are reported in Figure 2.7, where they are compared to measurements from Raupach et al. (1991). Third moments are non-dimensionalised in two ways: to their rms value (Figures 2.7a and 2.7b) and to the friction velocity u^* (Figures 2.7c and 2.7d).

When plotted as $\overline{w'w'w'}/\sigma_w^3$ and $\overline{u'u'u'}/\sigma_u^3$, third moments are constant from $(z-d)/\delta \simeq 0$ to $(z-d)/\delta \simeq 0.4$. The behaviour of $\overline{w'w'w'}/\sigma_w^3$ in the inertial layer is similar to Raupach's measurements, as both profiles are constant with height. Nevertheless, discrepancies appear close to the ground, where Raupach's moments are lower than ours. In the case of $\overline{u'u'u'}/\sigma_u^3$, the difference with Raupach's data is marked all along the boundary layer. Discrepancies appear also in the outer part of the boundary layer, where our non-dimensional measurements exhibit lower third moments (in absolute value). This could be related with the presence of a turbulence grid with squared meshes placed at the entrance of the test section, which produces velocity fluctuations also above the boundary layer height (δ). To make clear the origin of such differences, third moments are non-dimensionalised to u^* (Figures 2.7c and 2.7d). This second non-dimensionalisation flattens the differences in the outer part of the TBL and highlights those in the lower TBL. The fluxes of turbulent kinetic energy we measured are almost constant in the z-direction, while Raupach's exhibit a stronger gradient. The discrepancies between the two data-sets observed in third moments profiles are much higher than those we discussed for second order moments.

Probability Density Functions (PDFs) of the three components of velocity, u', v' and w', are shown in Figure 2.8 for various distances from the wall. PDFs

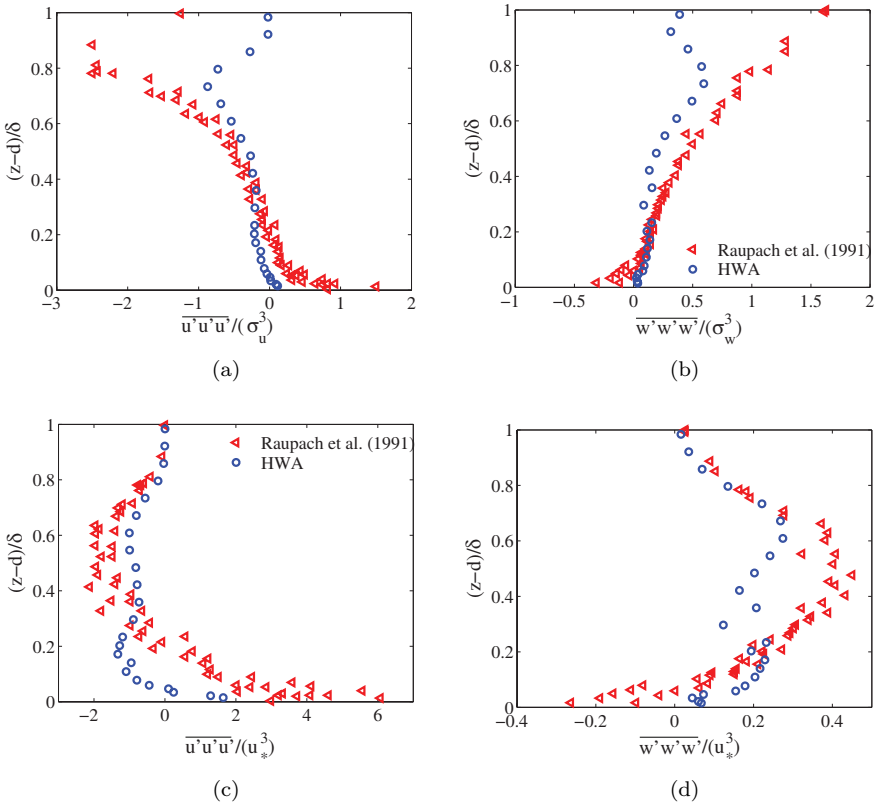

Figure 2.7: Velocity triple correlations. In (a) and (b) profiles are normalised to their rms value, while in (c) and (d) are normalised to u^*. Comparison with Raupach et al. (1991).

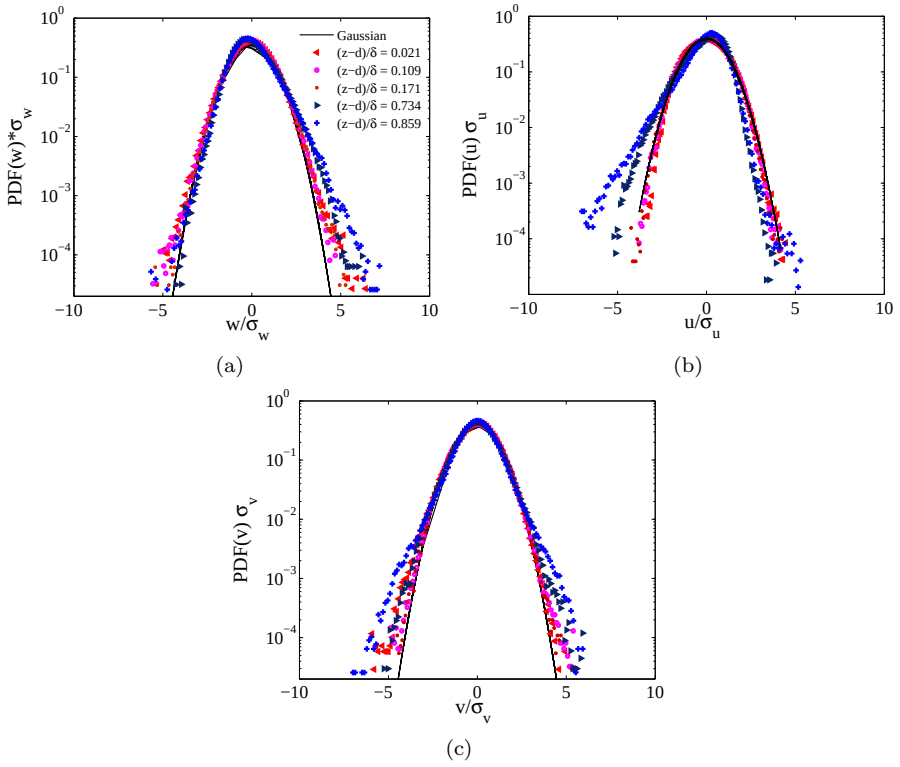

Figure 2.8: Probability density functions of the three velocity components at various elevations $(z-d)/\delta$ from the ground. The PDFs are normalised to their rms value.

are normalised to their rms to point out eventual departures from the Gaussian form. Since the hypothesis of Gaussian turbulence is widely assumed in stochastic dispersion models (Thomson, 1987), we are interested in understanding by which degree this hypothesis is satisfied in our boundary layer. Close to the wall, the PDFs of the three velocity components are very similar to a Gaussian distribution, such a behaviour is observed up to the limit of the inertial layer, at $z/\delta = 0.2$. On the contrary, in the outer layer ($z/\delta = 0.75$ and 0.875) the PDFs diverge substantially from the Gaussian distribution. For measurements in the outer layer, the PDFs of v' are symmetrical with respect to $v/\sigma_v = 0$, while the PDFs of w' and u' show a marked asymmetry. The PDF(w) is positively skewed, in agreement with the behaviour of the skewness $\overline{w'w'w'}$ that is positively asymmetric (Figure 2.7b). The same happens for the u-component, with $\overline{u'u'u'}$ that is negatively asymmetric (Figure 2.7a) and PDF(u) that is negatively skewed.

2.5.3 Velocity spectra

Scalar energy spectra $E(k)$ provide the distribution of energy in the wavenumber space. $E(k)$ represents the contribution to the total kinetic energy from Fourier modes with wavenumber magnitudes between k and $k + dk$. According to Kolmogorov theory of isotropic turbulence (Kolmogorov, 1941), velocity spectra consist of three ranges: the production range, which contains the bulk of the turbulent energy and where energy is produced by buoyancy and shear; the inertial subrange, where energy is neither produced nor dissipated but handed down to smaller scales; and the dissipation range, where kinetic energy is converted to internal energy. The characteristic length scale of the production range is the Eulerian integral length scale L. Such a scale corresponds roughly to the maximum of E(k) plotted against the wavenumber ($k \sim 1/L$). In the dissipation range, the scaling length is the so-called Kolmogorov microscale η. The existence of the inertial subrange is possible if there is a separation between the length scales in the boundary layer, so that the ratio $L >> \eta$. This will be verified in Paragraph 2.5.5.

In the inertial subrange the u-spectrum should be proportional to $\varepsilon^{2/3}k^{-5/3}$: the well known -5/3 power law. In this range turbulence is in a local isotropic condition and the following relation exists between u, v and w spectra (Kaimal and Finnigan, 1994):

$$F_v(k) = F_w(k) = \frac{4}{3}F_u(k). \tag{2.12}$$

We tested the existence of the inertial sublayer by verifying the respect of these conditions, as shown in Figure 2.9. All spectra fall off as $k^{-5/3}$. The spectra for v and w are placed higher than u and are separated by ratio that we estimated to be close to 4/3.

Since measurements are performed in frequency space, the conversion between spatial and frequency domain is done by invoking the Taylor's hypothesis of frozen turbulence. Our observations are defined in terms of the wavenumber k which corresponds to $2\pi f/\overline{u}$, where f is the frequency. Spectra of the three velocity components are shown in Figure 2.10, for growing distances from the wall. They are normalised using the distance z as a lenghtscale and the friction velocity u_* as a velocity scale, and plotted against the dimensionless frequency $n = fz/\overline{u}$.

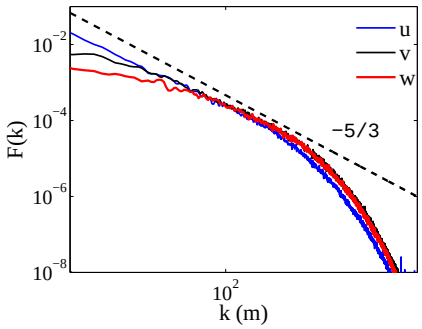

Figure 2.9: Velocity spectra of the three velocity components showing $-5/3$ slope in the inertial subrange and 4/3 ratio between the transverse (v, w) and stream-wise (u) components.

A model for u, v and w spectra $S_u(f)$, $S_v(f)$, $S_w(f)$ in the frequency domain was proposed by Kaimal et al. (1972), based on the Kansas experiments: a series of observations on wind and temperature fluctuations in stable conditions over a flat, uniform site. Such relations are valid in the inertial subrange, where they provide the expected -4/3 ratio and are represented by:

$$\frac{fS_u(f)}{u_*^2} = \frac{102n}{(1+33n)^{5/3}} \tag{2.13}$$

$$\frac{fS_v(f)}{u_*^2} = \frac{17n}{(1+9.5n)^{5/3}} \tag{2.14}$$

$$\frac{fS_w(f)}{u_*^2} = \frac{2.1n}{1+(5.3n)^{5/3}}. \tag{2.15}$$

The measured spectra show good agreement with Kaimal model in the inertial subrange, as shown in Figure 2.10. Outside the range the model is not valid and does not fit the measured velocity spectra anymore .

Note that the conversion from wavenumber to frequency domain can be done by means of the relation :

$$kF(k) = fS(f) = nS(n), \tag{2.16}$$

since these expressions represents the same numerical value. Thus, $fS(f)$ can be plotted as a function of k, f or n without any conversion of units (Kaimal and Finnigan, 1994).

2.5.4 Two-points spatial correlations

Two-points spatial correlations are the simplest statistics containing information on the spatial structure of the velocity field. The two-point spatial correlation coefficient is defined as:

$$\rho_{ii}(\mathbf{x},\mathbf{r}) = \frac{\overline{u_i'(\mathbf{x})u_i'(\mathbf{x}+\mathbf{r})}}{\sigma_i^2}, \tag{2.17}$$

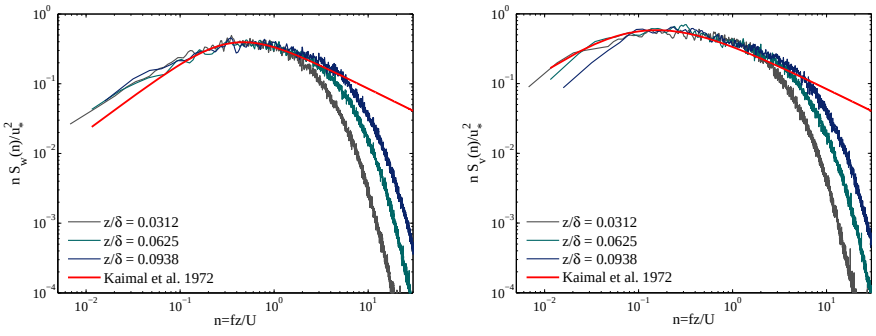

(a) $\frac{fS_w(f)}{u_*^2}$

(b) $\frac{fS_v(f)}{u_*^2}$

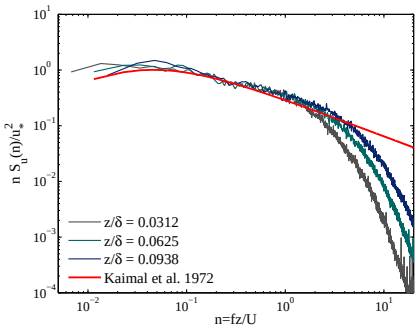

(c) $\frac{fS_u(f)}{u_*^2}$

Figure 2.10: Velocity spectra of the three velocity components for growing distances from the wall, z/δ. Comparison with a model extrapolated from field data (Kaimal et al., 1972).

where u_i' represents velocity fluctuations of u, v and w. Correlation coefficients were calculated from PIV measurements in the (x, z)- and (y, z)- planes, and maps of correlation were obtained for the three velocity components in both planes. We reported in Figure 2.11 the maps obtained for the (x, z)-plane at the level of the roughness sublayer and in Figure 2.12 for the outer part of the boundary layer. In the same figures are also shown profiles of correlation extracted along the x and z axis, perpendicular to the point of correlation. Given the limited size of the PIV images, the separation is unfortunately not sufficient to reveal any negative lobes in the correlations. For each velocity component, we indicate the correlation field as $\rho_{ii}(x, z)$, $\rho_{ii}(y, z)$ and the profiles as $\rho_{ii}(x)$, $\rho_{ii}(y)$, $\rho_{ii}(z)$.

Correlation coefficients in the three directions are sensibly different. $\rho_{ww}(x, z)$ is larger in the direction normal to the wall, showing that roughness elements are effective in imparting their influence to the turbulent flow (Krogstad and Antonia, 1994). The iso-correlation lines can be well approximated by ellipses whose semi-major axis is aligned in the z- direction. The spatial extent of $\rho_{ww}(x, z)$ and $\rho_{vv}(x, z)$ is similar, while the correlation $\rho_{uu}(x, z)$ is considerably wider. In the higher part of the boundary layer, correlations have a greather ex-

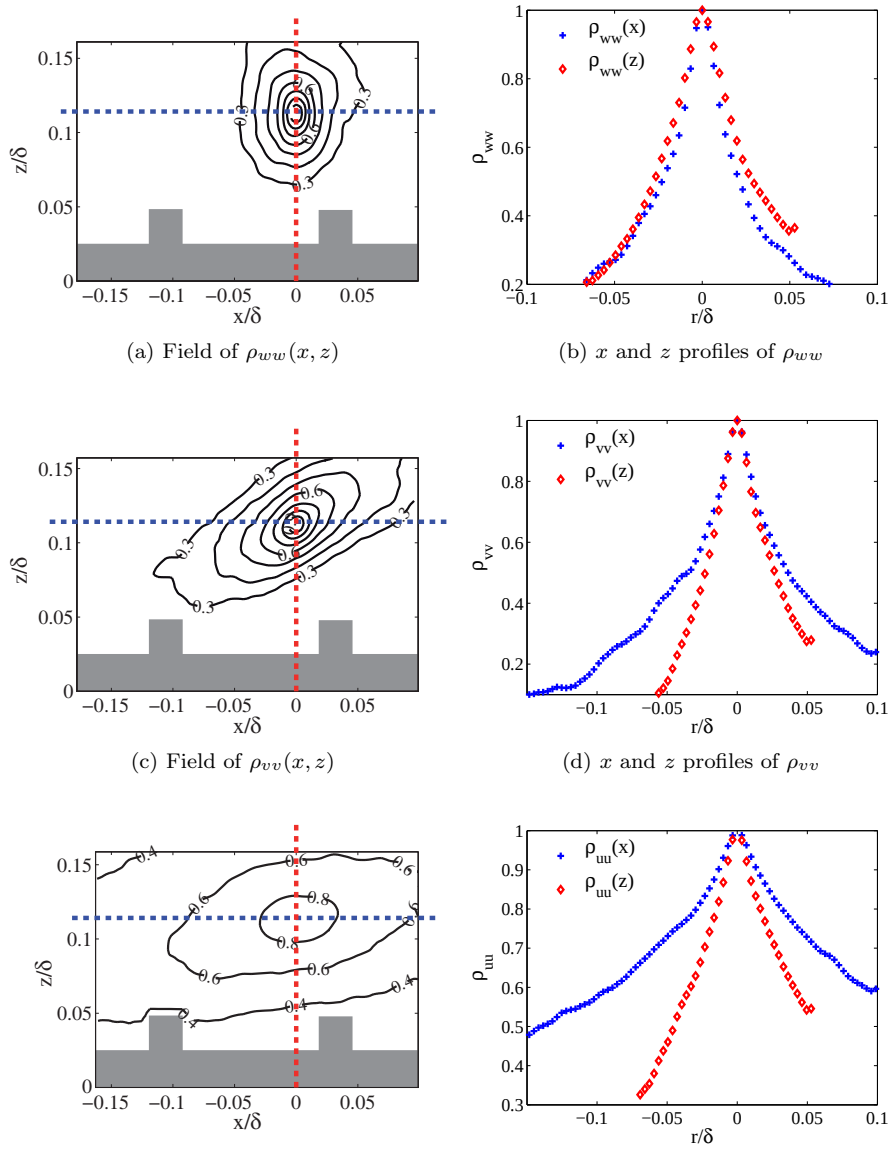

(a) Field of $\rho_{ww}(x,z)$ (b) x and z profiles of ρ_{ww}

(c) Field of $\rho_{vv}(x,z)$ (d) x and z profiles of ρ_{vv}

(e) Field of $\rho_{uu}(x,z)$ (f) x and z profiles of ρ_{uu}

Figure 2.11: Two-point spatial correlations in the lower part of the velocity field. Measurements in the xz-plane. Contours of the correlations in (a),(c),(e) with interval 0.3. The profiles are extracted perpendicular to the point, along the x and z axis.

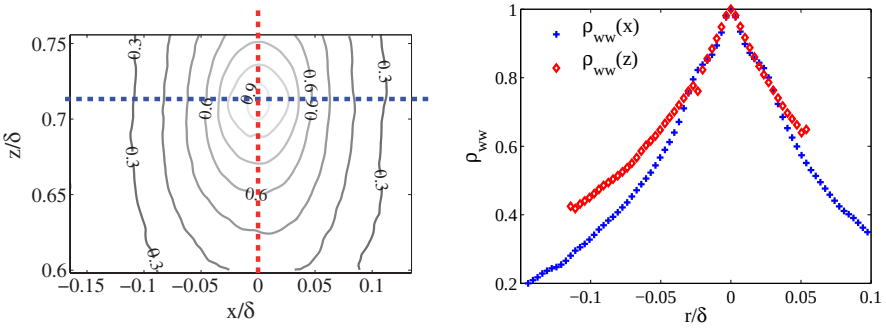

(a) Field of $\rho_{ww}(x,z)$ (b) x and z profiles of ρ_{ww}

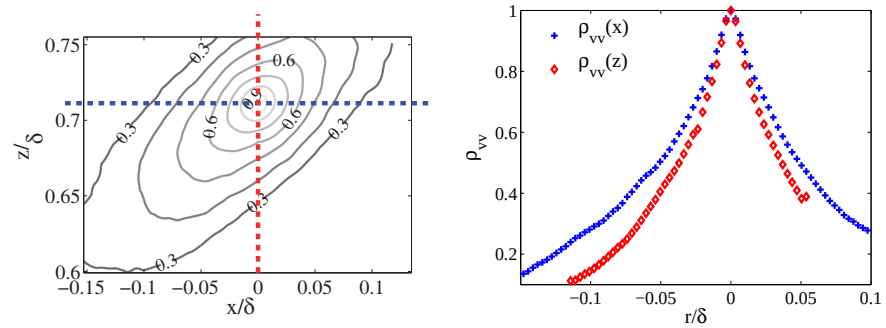

(c) Field of $\rho_{vv}(x,z)$ (d) x and z profiles of ρ_{vv}

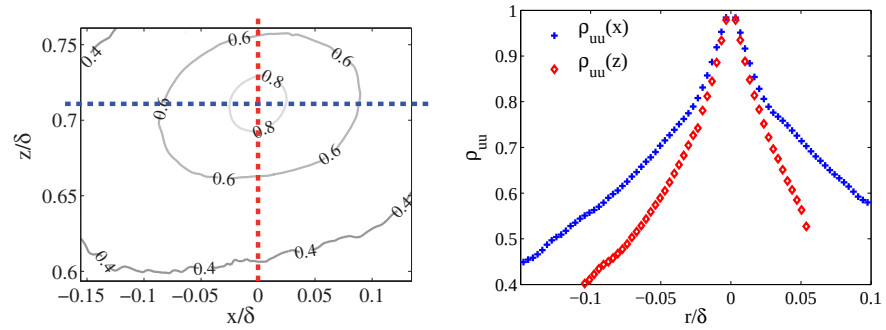

(e) Field of $\rho_{uu}(x,z)$ (f) x and z profiles of ρ_{uu}

Figure 2.12: Two-point spatial correlations in the outer region. Measurements in the xz-plane. Contours of the correlations in (a),(c),(e) with interval 0.3. The profiles are extracted perpendicular to the point, along the x and z axis.

tension compared to their equivalent close to the wall. The correlations $\rho_{vv}(x, z)$ and $\rho_{uu}(x, z)$ are tilted with respect to the horizontal due to the shear produced by the wall roughness, as demonstrated by Krogstad and Antonia (1994) who compared correlations on rough and smooth walls. Close to the wall the inclination is of 36° for $\rho_{vv}(x, z)$ and of 15° for $\rho_{uu}(x, z)$. In the higher part of the boundary layer $\rho_{uu}(x, z)$ becomes almost aligned in the x-direction. On the contrary, the tilt of $\rho_{vv}(x, z)$ is increased far from the surface and reaches 44°.

The profiles of the three correlation functions plotted in Figure 2.11 and in Figure 2.12 are characterised by a sharp peak at $r = 0$, that hides the presence of the horizontal asymptote of the curves for $r \to 0$. This is an evidence that the influence of viscous effects is limited to a tiny region, and that this characteristic viscous length scale is smaller than the PIV measuring volume.

2.5.5 Eulerian integral length scales

Eulerian Integral Length Scales (EILS) represent the distance over which the turbulence remains correlated and are a measure of the size of the energetic scales of turbulence. In isotropic turbulence, the spatial structure of the large scale turbulent flow can be fully characterised by a single parameter. This is of course not the case in the anisotropic and non-homogeneous turbulence within a boundary layer flow, which is characterised by a variety of scales (Carlotti and Drobinski, 2004). We therefore evaluated EILS in x, y, z directions for the three velocity components. Length scales were obtained from measurements carried out with hot-wire anemometry, where a temporal evolution of turbulence in the Eulerian sense is recorded, and from two-point spatial correlation from PIV measurements, allowing a distinction between the x, y and z direction. One advantage of using two-point correlations is that the length scale is directly measured from spatial information of flow fields without the use of Taylor's frozen turbulence hypothesis.

Eulerian integral length scales from velocity spectra

Eulerian integral length scales are derived from one-dimensional velocity spectra $F(k)$ as the maximum of the spectra plotted against the wavenumber: $k \sim 1/L$ (Kaimal and Finnigan, 1994). According to the velocity components available from HWA measurements, EILS are defined as $\mathcal{L}_{uu}$, $\mathcal{L}_{vv}$ and $\mathcal{L}_{ww}$. Since the Taylor's hypothesis of frozen turbulence were made in order to calculate velocity spectra (turbulence is frozen in time and transported horizontally past the observer), it is therefore implicitly assumed that EILS are to be intended in the mean flow direction (x). Scales $\mathcal{L}_{vv}$ and $\mathcal{L}_{ww}$ are shown in Figure 2.13, non-dimensionalised with the boundary layer depth δ. It was not possible to evaluate $\mathcal{L}_{uu}$ because we could not identify reliably a maximum in our measured u-spectra. The determination of $\mathcal{L}_{vv}$ and $\mathcal{L}_{ww}$ was easier close to the wall and outside the boundary layer, while more uncertainties affects the scales evaluation in the outer boundary layer, where the maximum of the spectra is identified with less precision.

We can observe that the scale associated to the transverse velocity $\mathcal{L}_{vv}$ is about two times the vertical scale $\mathcal{L}_{ww}$, on all the extension of the boundary layer. The two scales are equal in the region outside the boundary layer, were the field is influenced by the grid placed at the entrance of the test section. The

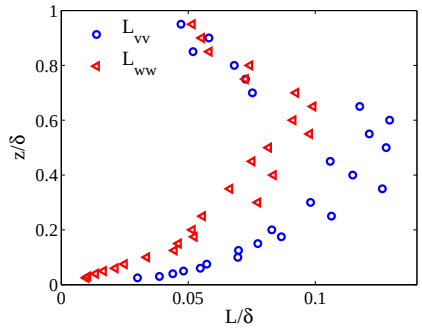

Figure 2.13: Integral length scales derived from velocity spectra.

grid have square meshes and generates a turbulence that is homogeneous and isotropic, so that structures in the vertical and transverse directions have the same size.

Eulerian integral length scales from two-points spatial correlations

Two-points spatial correlations from PIV measurements in the (x, z)- and (y, z)-planes were used here to estimate Eulerian integral length scales L_{uu}, L_{vv} and L_{ww} in the three directions x, y, z, as shown in Figure 2.14. Integral length scales are defined as:

$$L_{ii} = \int_0^\infty \rho_{ii}(\mathbf{x}, \mathbf{r}) d\mathbf{r}, \tag{2.18}$$

where $\rho_{ww}(\mathbf{x}, \mathbf{r})$ is the correlation coefficient (Eq. 2.17), that can be computed for the three velocity components.

In order to avoid the uncertainties related to the numerical estimate of the integral, we assume that the correlation coefficient is an exponential function of the type:

$$\rho_{ii}(\mathbf{x}, \mathbf{r}) = e^{-r/\Lambda_{ii}}, \tag{2.19}$$

and we assume the scale Λ_{ii} as a measure of the EILS (this corresponds to the distance at which the correlation function is equal to $e^{-1} \simeq 0.37$ (Tritton, 1988)). The choice of an exponential function is motivated by the form of the profiles of the correlation functions (see Figure 2.11 and in Figure 2.12), with an unnoticeable horizontal for $r \to 0$.

By fitting Eq. 2.19 to the data in the x, y, z directions we could compute nine different length scales, i. e. $L_{uu}(x)$, $L_{uu}(y)$, $L_{uu}(z)$, $L_{vv}(x)$, $L_{vv}(y)$, $L_{vv}(z)$, $L_{ww}(x)$, $L_{ww}(y)$, $L_{ww}(z)$. With our data, we could not find this value in every case without extrapolation. This is particularly true for the u component, whose correlation falls below 0.5 only in the velocity field acquired close to the ground. In these cases we chose to extrapolate the exponential function up to 0.37. The same disadvantage occurred to Bewley et al. (2012), who chose to calculate the scale as the separation at which the correlation functions fall below 0.5, and to Takimoto et al. (2013) who estimated length scales over surfaces with different roughness types and used the threshold $\rho_{ii} = 0.4$.

Integral length scales L_{uu}, L_{vv}, L_{ww} from PIV and $\mathcal{L}_{vv}$, $\mathcal{L}_{ww}$ from HWA measurements are shown in Figure 2.14. Scales from HWA were obtained by

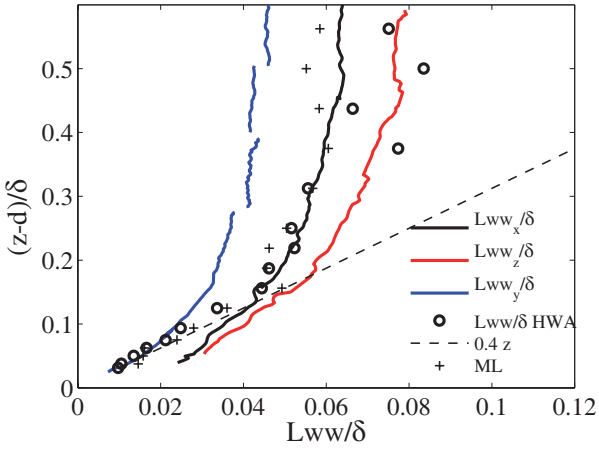

(a) L_{ww}/δ

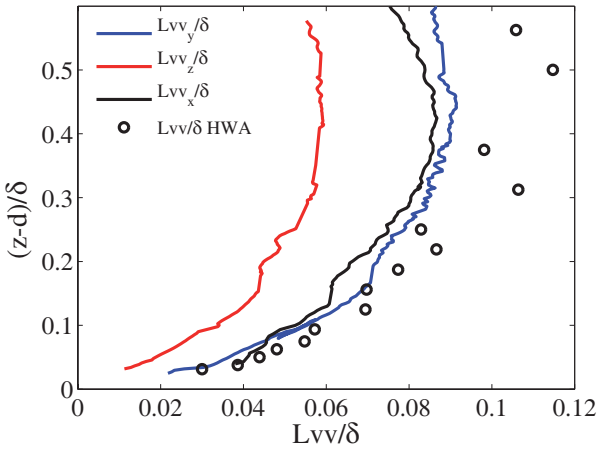

(b) L_{vv}/δ

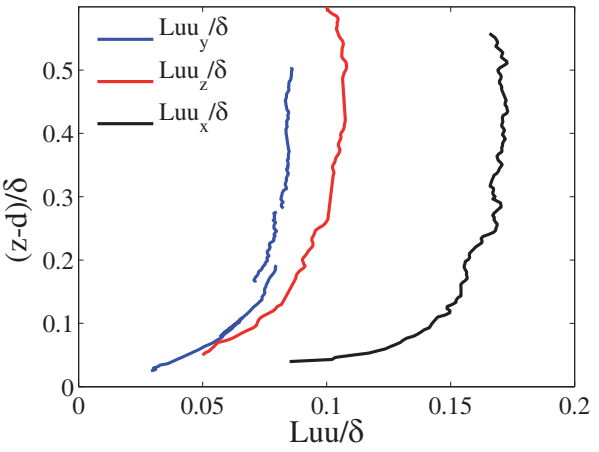

(c) L_{uu}/δ

Figure 2.14: Integral length scales from PIV and HWA measurements, for the three velocity components. In (a), comparison with the mixing length theory (referred to as ML).

means of Taylor's hypothesis and are intended in the mean flow direction x. The comparison with PIV measurements show that $\mathcal{L}_{ww}$ superpose with $L_{ww}(x)$ in the streamise direction. Also the transverse scale $\mathcal{L}_{vv}$ is in accord with $L_{vv}(x)$, but only in the inertial subrange, while better agreement is observed between $\mathcal{L}_{vv}$ and $L_{vv}(y)$.

A comparison is made between L_{ww} and the mixing length (l) from Prandtl's hypothesis, defined as (Schlichting and Gersten, 2000):

$$\overline{u'w'} = l^2 \left| \frac{\partial \overline{u}}{\partial z} \right| \frac{\partial \overline{u}}{\partial z}. \tag{2.20}$$

The mixing length is usually assumed as an estimate of the size of larger scale eddies. Figure 2.14a shows that the estimates of l are very close to $L_{ww}(x)$ and $\mathcal{L}_{ww}$. Figure 2.14a also shows that these quantities scales as $l \sim 0.4z$ in the lower part of the TBL, as predicted by the similarity theory (Garratt, 1992).

Another relation for L_{ww} that is widely used in the parametrisation of turbulence for pollutant dispersion was proposed by Sawford and Stapountzis (1986):

$$L_{ww} \sim \frac{\sigma_w}{\varepsilon \delta}, \tag{2.21}$$

with a proportionality constant that varies between 0.8 (Sawford and Stapountzis, 1986) and 1.8 (Postma et al., 2011a). As shown in Figure 2.15, Equation 2.21 provides an excellent estimate of L_{ww} assuming a proportionality coefficient equal to 0.6.

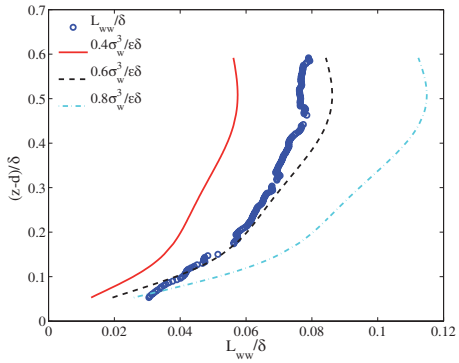

Figure 2.15: Integral length scale L_{ww} from PIV measurements, compared to Equation 2.21 where the proportionality constant assumes the values 0.4, 0.6 and 0.8.

In the case of the v-component, $L_{vv}(x)$ and $L_{vv}(y)$ are very close to each other, with $L_{vv}(y)$ becoming slightly bigger outside the inertial layer. The vertical scale $L_{vv}(z)$ is much smaller than the other two and is about half $L_{vv}(y)$.

The stream-wise component u is generally characterised by bigger length scales. The main direction of correlation is x and $L_{uu}(x)$ is by far the biggest integral length scale in our boundary layer. As observed by Krogstad and Antonia (1994), scales in the flow direction are highly influenced by the wall roughness. In the limit case of a smooth wall, the stream-wise extent of the correlation is much larger for a smooth surface than for a rough wall.

From the analysis of the integral length scales emerges all the complexity of the velocity field. Our results show that there exist a great variety of length scales in our boundary layer and that only one of them, i. e. $L_{ww}(z)$, scales with z according to the statement of the similarity theory. A study about length scales in wall-bounded turbulence was conducted by Carlotti and Drobinski (2004). By means of a combination of two tools (inhomogeneous rapid distortion theory and high-resolution large-eddy simulations) this study shed some light on the wide number of length scales needed to characterize the anisotropy of turbulence. Integral length scales are related to spectra and their asymptotic behaviour in the surface layer depends on the spectra shape. Carlotti and Drobinski (2004) show that there is always at least one length scale that does not scale with z, and that the assumption of proportionality with z is not compatible with the assumption of a spectrum decaying according to Kolmogorov's law, but rather with a spectrum following a -1 power law. Fortunately, such a -1 power law exists in spectra of high-Reynolds number wall-bounded turbulence.

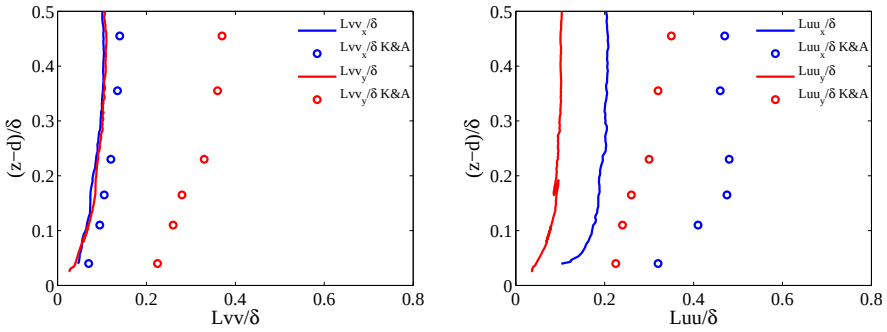

(a) L_{vv}/δ (b) L_{uu}/δ

Figure 2.16: Integral length scales compared to Krogstad and Antonia (1994).

Integral length scales were compared to the ones estimated by Krogstad and Antonia (1994), who investigated the effects of surface roughness on turbulent boundary layers. In this case, span-wise and stream-wise length scales are calculated as the widths, in the $x-$ and $y-$ directions, of the contours of the correlation function $\rho_{uu} = 0.3$ and $\rho_{vv} = 0.3$. A comparison with our measurements is shown in Figure 2.16, where our integral length scales are calculated by adopting the same definition used by Krogstad. Length scales from Krogstad are bigger than ours, in both directions and for both $u-$ and $v-$ components.

The existence of a fully developed turbulence, i.e. of an asymptotic dynamical regime independent of the Reynolds number, is based on the assumption that the macro scale L_m and the micro (dissipative) scale η characterizing the flow have to be separated of several orders of magnitude, so that an inertial region can develop between the two. The experimental estimates of L_m and η allows us to verify this assumption for the velocity field investigated here.

We calculated η from Equation 2.9 and we estimated a mean integral length scale L_m as:

$$L_m = 1/3(L_{uu}(x) + L_{vv}(y) + L_{ww}(z)), \tag{2.22}$$

where $L_{uu}(x)$, $L_{vv}(y)$ and $L_{ww}(z)$ are Eulerian integral length scales from PIV

measurements. Vertical profiles of η and L_m and the ratio L_m/η are reported in Figures 2.17a, 2.17b and 2.17c. The Kolmogorov microscale is of the order of 0.0001 m, while the mean integral length scale L_m is of the order of 0.01 m. Their ratio is therefore included between a minimum of about 145 close to the wall and a maximum of 230 in the core of the TBL (Figure 2.17c). We can therefore conclude that in our velocity field the requirement of the scales separation is satisfied.

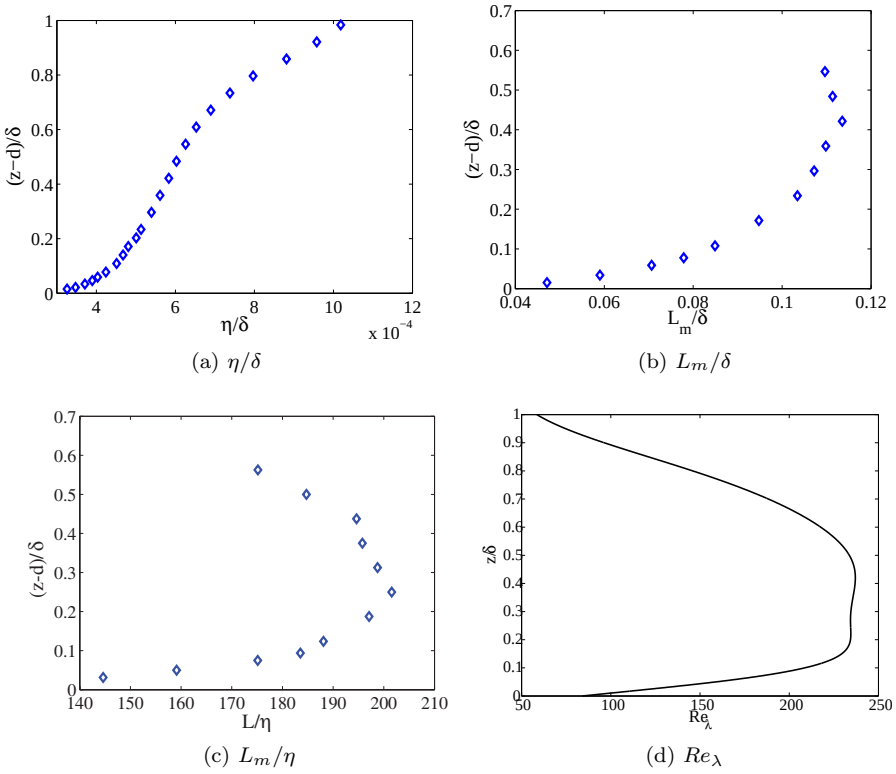

Figure 2.17: Vertical profiles of the Kolmogorov microscale η (a), of the mean integral length scale L_m (b), of the ratio L_m/η (c) and of Re_λ (d).

A further information on the dynamical state of the turbulence can be inferred by computing a Reynolds number, Re_λ, based on the Taylor micro scale as it is customary in homogeneous and isotropic turbulence. This is defined as:

$$Re_\lambda = \frac{2}{3} q^2 \frac{\lambda}{\nu}, \tag{2.23}$$

where q^2 is the turbulent kinetic energy and where the Taylor micro scale is computed as:

$$\lambda = \sqrt{15 \frac{2}{3} q^2 \frac{\nu}{\varepsilon}}. \tag{2.24}$$

As shown in Figure 2.17d, in most of the velocity field Re_λ is generally larger than 150. Based on theoretical considerations and previous DNS results

(Franzese and Cassiani, 2007), this value corresponds to a flow regime that is not far from an asymptotic state, but is not sufficiently large to prevent a slight influence of viscous effects on the turbulence dynamics.

2.5.6 Lagrangian time scales and turbulent diffusivity

Finally we focus on two key parameters of the flow which govern the dispersion mechanisms within a turbulent boundary layer: the Lagrangian time scale T_L and the turbulent diffusivity D_t.

The Lagrangian time scale is a measure of the correlation of fluid particles velocity in time. In Lagrangian models, T_L is the time scale governing turbulent relative dispersion and appears in the Langevin equation. T_L is also needed in Gaussian models to calculate the turbulent diffusion coefficient D_t, used to estimate the convective flux by means of a gradient law and the plume spread downwind the source. In an anisotropy and inhomogeneous velocity field, T_L is a local characteristic of the flow and is defined as:

$$T_L(x_i) = \int_0^\infty \rho_L(x_i, \tau) d\tau, \tag{2.25}$$

where $\rho_L(x_i, \tau) = \overline{U_i(x_i, t), U_i(x_i, t+\tau)}$ is the one point correlation function in time (Tennekes, 1982) and U_i are Lagrangian velocities. The correlaton decreases as time interval τ increases, and at large times τ the two velocities are uncorrelated.

The direct measurement of Lagrangian statistics is something hard to do. Experimentally, it should be necessary to mark a great number of fluid particles or, alternatively, to introduce in the flow a number of tracers that can be faithfully transported in the current and then measure the three components of their velocity while following them in their motion. However there have been measurements of the spread of puffs or clouds of tracer or of the separation of pairs of balloons in the atmosphere and in a wide range of conditions and scales (experiments are summarized in Monin and Yaglom (1975) and in Pasquill and Smith (1983)).

A great deal of effort has been spent in attempts to predict T_L from Eulerian data. This simple relation proposed by Hay and Pasquill (1959) to infer the Lagrangian time scale from the Eulerian one is widely used in dispersion models:

$$\beta = \frac{T_L}{T_E} = const, \tag{2.26}$$

where T_E is the Eulerian time scale and β is the ratio between Eulerian and Lagrangian time scales. Equation 2.26 establishes a connection between the spatial structure and the temporal evolution of a flow particle through the assumption of similarity in the Lagrangian and Eulerian spectra. This implies the idea that the turbulent flow evolves towards a statistically steady state, independently on the conditions that generated and maintain such a flow. Several experimental estimates of β are available and differ significantly one to the other: β is expected to range from 2-3 to almost 12. Such a variability does not satisfy the request of finding a universal law valid for all turbulent flows.

Our experimental apparatus does not allow us to measure Lagrangian time scales directly. Therefore, here we limit ourselves to an analysis of different

estimates of Lagrangian time scales in the vertical and transversal direction, hereafter referred to as T_{Lw} and T_{Lv}, given by two different parametrisations usually adopted in the literature and to a verification of their consistency one to the other. Moving from dimensional considerations, we can obtain an first estimate of T_{Lw} and T_{Lv} simply by evaluating a characteristic life time of the flow larger scale structures as:

$$T_{Lw1} \sim \frac{L_{ww}}{\sigma_w} \tag{2.27}$$

$$T_{Lv1} \sim \frac{L_{vv}}{\sigma_y}. \tag{2.28}$$

We compare this value with the estimates of the Lagrangian time scale that are widely adopted in the parametrisation used in pollutant dispersion models:

$$T_{Lw2} = \frac{2\sigma_w}{C_0\varepsilon} \tag{2.29}$$

$$T_{Lv2} = \frac{2\sigma_v}{C_0\varepsilon}, \tag{2.30}$$

where C_0 is the Kolmogorov constant, whose value in the literature varies between 2 and 8, and that is usually considered as a free parameter evaluated a posterori. We will discuss further this variability in Paragraph 4.4.1. The comparison between the two estimates in the y- and z-directions is plotted in Figure 2.18, assuming values for C_0 between 3 and 6 and shows that the best agreement is achieved for $C_0 \simeq 4 \div 5$. As we will see in the next chapters, a value of C_0 included in this same interval provides the best agreement between our experimental profiles and numerical results obtained with a Lagrangian stochastic model and an Eulerian analytical model.

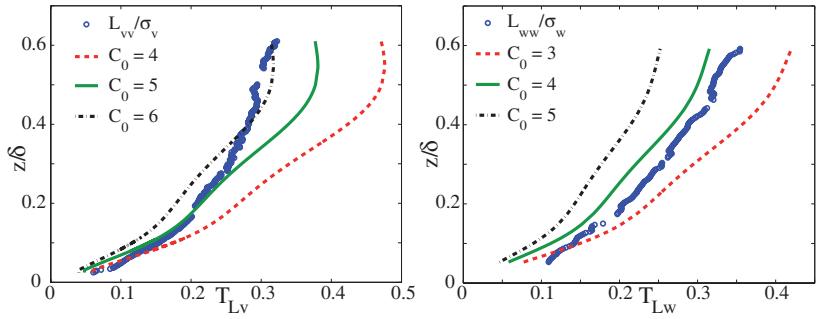

(a) T_{Ev},T_{Lv} (b) T_{Ew},T_{Lw}

Figure 2.18: Eulerian time scales T_{Ew} and T_{Ev} from Eqs. 2.27 and 2.28 (blue circles), compared to Lagrangian time scales T_{Lw} and T_{Lv} from Eqs. 2.29 and 2.30, where C_0 assumes the values 4,5 and 6.

Assuming the simple parametrisation of T_{Lw} and T_{Lv} given by Eqs. 2.27 and 2.28 we can finally compute the vertical and transverse turbulent diffusivity and

compare them to literature data. Turbulent diffusivity are estimated as:

$$D_{tz} = T_{Lw}\sigma_w^2 \simeq \sigma_w L_{ww} \tag{2.31}$$

$$D_{ty} = T_{Lv}\sigma_v^2 \simeq \sigma_v L_{vv}. \tag{2.32}$$

Figure 2.19 shows that D_{tz} and D_{ty} vary from about 0 close to the wall to an approximately constant value just above the inertial region, i. e. $z/\delta = 0.2$. As expected, values of D_{ty} are about two times larger than those of D_{tz}. However, it is worth noting that this difference is mainly due to an enhanced velocity standard deviation σ_v (see Figure 2.4b) rather than to a larger size of the large scale eddies, since L_{vv} is only about 25% larger than L_{vv} (see Figure 2.14). As far as we are aware no literature data are available providing direct estimates of D_{tz}, that can not therefore compared to any experimental value. Conversely, we could compare the modelled D_{tz} in Equation 2.31 with the experimental estimates provided by Fackrell and Robins (1982a), who calculated D_{tz} as:

$$D_{tz} = \frac{\overline{w'c'}}{\partial C/\partial z}, \tag{2.33}$$

where C is the mean scalar concentration and the correlation $\overline{w'c'}$ represents the vertical turbulent mass flux. The comparison (Figure 2.19) shows remarkable good agreement between our estimate and the experimental data.

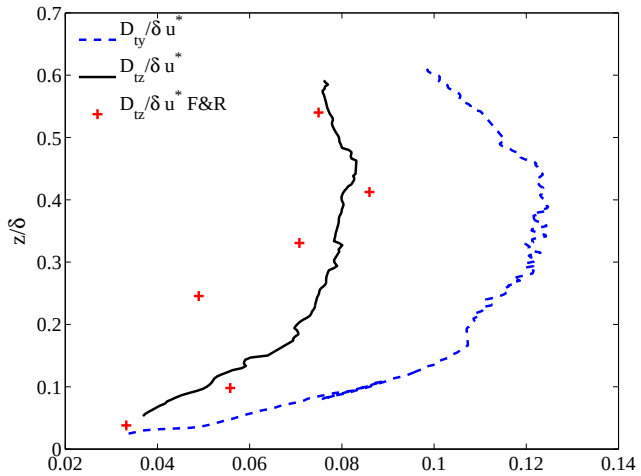

Figure 2.19: Vertical profile of the turbulent diffusivities D_{tz} and D_{ty}. Comparison with D_{tz} directly measured by Fackrell and Robins (1982a).

Chapter 3

THE CONCENTRATION FIELD

3.1 ABSTRACT

The prediction of the probability density function (PDF) of a pollutant concentration within atmospheric turbulent flows is of great importance in assessing the effects of toxic materials on human health or the hazard related to accidental releases of toxic or flammable substances. This need motivates studies aiming in characterising the concentration statistics of pollutant dispersing in turbulent boundary layers, and their dependence on the parameters controlling their emissions. Here we present a new experimental data set providing a detailed description of the temporal and spatial evolution of a fluctuating neutrally buoyant plume emitted by a point source within the turbulent boundary layer. As it is known from the studies conducted by Fackrell and Robins (1982a), concentration fluctuations are significantly influenced by the diameter of the source and by its elevation. In this study, we further inquire into the dependence on the source configuration, including source size, elevation and emission velocity, by studying its influence on higher order concentration moments. Vertical and transversal profiles of first four moments of concentration PDF are presented for several distances downwind. The data-set includes concentration PDFs, spectra, functional relationships between concentration moments, intermittency factors, concentration variance dissipation and production. Their analysis allow us to infer the main mechanisms controlling the scalar dispersion, depending on source configuration and emission conditions.

3.2 INTRO

The knowledge of the statistics of the concentration of a pollutant substance in air is useful in a wide range of situations. For example, mean concentrations have to be estimated in air quality studies in urban areas or in problems of chronic pollution in order to asses the chronical risk for a subject exposed to some environmental contamination. However, there are often situations where the knowledge of the sole mean is insufficient. In the case of a release of flammable

and explosive substances, what matters is if the instantaneous concentration locally falls in the limits of flammability (or explosivity). When studying the dispersion of odours, one is interested in peak concentrations, to whom human nose is sensitive. Similar needs are encountered in studies of exposure to and dosages of hazardous materials and peak-to-mean ratios. In all those cases, the necessity rises of estimating the PDF of concentration, or at least to characterise its lower moments or their peak values.

To that purpose several modelling approach have been developed. These include meandering models (Gifford (1959), Yee et al. (1994), Luhar et al. (2000), Franzese (2003)), particles Lagrangian stochastic models (Durbin (1980), Sawford and Stapountzis (1986)), micro-mixing Lagrangian models (Sawford (2004), Cassiani et al. (2005a), Cassiani et al. (2005b)).

The validation of all kind of dispersion models needs quality experimental data. For what concerns concentration fluctuations in neutrally buoyant plumes from point sources in the TBL, the study of Fackrell and Robins (1982a,b) has been largely used as a reference. In their study, F&R discussed phenomenological and dynamical aspects of the dispersion and the effects of the source size and of the source elevation. Yee et al. (1993) used dispersion measurements in a saline neutral plume from an elevated point source (from Wilson et al. (1991)) to test several functional forms for the PDF of scalar concentration. More recently, the meandering of a plume dispersing in a water channel was measured directly by Hilderman and Wilson (2007) using laser-induced fluorescence. All these studies however tend to focus mainly on the second order statistics and on the correlation between velocity and correlation fluctuations. Relatively little information is available concerning higher order concentration moments. This is a considerable lack for the modellers aiming in the prediction of the spatial evolution of the concentration PDFs.

Our study aims in extending the work on source size and elevation conducted by Fackrell and Robins (1982a,b) to high order concentration moments, with a detailed definition of the plume structure also in its initial phase of growth. To that purpose we have conducted a series of experiments on the dispersion of a passive scalar emitted by a source of varying size and height, within the TBL, whose dynamics is analysed in the first part of this study. We also investigate the influence of the emission velocity at the source, that is likely to influence concentration fluctuation measurements in a non negligible way.

Results are presented in a non-dimensional form, using length, velocity and mass scales for the non-dimensionalization, so that differences between source sizes are preserved. The data set includes vertical and transversal profiles of concentration statistics for several distances from the emission point, concentration PDFs, functional relationships between concentration moments, spectra, dissipation of concentration fluctuations, intermittency factor, plume spreads and peak concentrations.

3.3 CHARACTERISTICS OF SCALAR DISPERSION

Because of the chaotic nature of turbulent flows, the concentration $c(x_j, t)$ of a passive scalar transported within a turbulent boundary layer has to be con-

sidered as a random variable and is fully described by its Probability Density Function (PDF). By adopting the Reynolds decomposition, the concentration can be written as the sum of a mean value C and a fluctuation c':

$$c = C + c'. \tag{3.1}$$

Follow on from the introduction of these quantities, the concentration field can be described in terms of mean values C and fluctuations $\overline{c'^n}$, and all the moments can be calculated by means of the PDF, $p(c; x_j, t)$, with the relations:

$$C(x_j) = \int_{-\infty}^{\infty} c \;\; p(c; x_j) \;\; dc \tag{3.2}$$

$$\overline{(c - C)^n} = \overline{c'^n} = \int_{-\infty}^{\infty} [(c - C)^n] \;\; p(c; x_j) \;\; dc \tag{3.3}$$

On the other side, if the moments of the distribution are known, $p(c; x_j, t)$ can be mathematically inferred because the PDF and its moments are in bi-unique correspondence (Tennekes and Lumley, 1972). Therefore, the ensemble of the infinite moments and the PDF are equivalent in the description of the random process.

Considering a passive scalar dispersing in a neutral boundary layer, the equation for the temporal evolution of the instantaneous concentration is:

$$\frac{\partial c}{\partial t} + \frac{\partial}{\partial x_j}(u_j c) = \frac{\partial}{\partial x_j}\left(D \frac{\partial c}{\partial x_j}\right), \tag{3.4}$$

where the terms $u_j c$ and $D\partial c/\partial x_j$ represents the advection and the diffusion mass fluxes respectively. By averaging Eq. 3.4 we obtain an equation of the evolution of the mean concentration:

$$\frac{\partial C}{\partial t} = -\frac{\partial}{\partial x_j}\left(\overline{u}_j C + \overline{u'_j c'} - D \frac{\partial C}{\partial x_j}\right), \tag{3.5}$$

where the correlation $\overline{u'_j c'}$ represents the coupling of velocity and concentration fluctuations.

The presence of the unknown term $\overline{u'_j c'}$ in Eq. 3.5 makes the problem unclosed. To solve Eq. 3.5 in the x-direction, the convective flux can be modelled by means of an analogy with Fick law for molecular diffusion, according to the gradient-transfer theory (Pasquill and Smith, 1983):

$$\overline{u'c'} = -D_{tx} \frac{\partial C}{\partial x}. \tag{3.6}$$

In Equation 3.6, the convective flux is assumed proportional to the mean concentration gradient as in molecular diffusion processes. The turbulent diffusion coefficient D_t appears as a propriety of the fluctuating velocity field and it differs from the molecular diffusivity D because of its greater order of magnitude. Even if this closure hypothesis is helpful, as it allows the solution of the equation, it is questionable from a physical point of view. Unlike molecular diffusion, convective dispersion do not have a local nature and can transport a scalar at distances of the same order of the flow characteristic length scales.

The convective term can not be neglected, on the contrary his role in dispersing the contaminant is of primary importance, as it can be demonstrated

with an analysis of its order of magnitude. The order of magnitude of $\overline{u_j' c'}$ is estimated as $\sigma_u \sigma_c$. The molecular term $D\partial C/\partial x_j$ has a magnitude of the order of $D(d\vartheta/\delta)$, where $d\vartheta$ is the variation of C and δ is the boundary layer height. The difference between $d\vartheta$ and σ_c can not be too large, because concentration fluctuations in the atmospheric boundary layer are on average close to the maximal spatial variation of the mean C. If $d\vartheta$ and σ_c are considered to have the same magnitude, the ratio of molecular and convective terms results $\sim D/(\delta\ \sigma_u)$. Since this ratio is a very small number, the molecular diffusion can be neglected and Equation 3.5 becomes:

$$\frac{\partial C}{\partial t} = -\frac{\partial}{\partial x_j}\left(\overline{u}_j C + \overline{u_j' c'}\right). \tag{3.7}$$

The difference between concentration statistics for a real scalar and one with zero diffusivity is negligible for the mean concentration at high Reynolds numbers and high Peclet numbers, except very close to a small source (with respect to the integral lenght scale and therefore for sources having a size comparable to the diffusive lenght scale) or a boundary (Sawford, 2001).

Assuming a Lagrangian point of view, in the hypothesis of negligible molecular diffusion and of divergence of the velocity equal to zero, Equation 3.4 can be rewritten as:

$$\frac{Dc}{Dt} = 0 \tag{3.8}$$

so that on the trajectory $dy_i = U_i dt$ of a particle emitted from the source (U_i is the Lagrangian velocity), the concentration is conserved ($c = cost$). Lagrangian models use this principle to simulate the dispersion of a scalar in a turbulent field. They reproduce a number N of trajectories and calculate the mean concentration by counting the number of particles that falls in a volume of fluid, at a given position downwind. Since molecular diffusion is neglected, the pollutant fluid particles do not exchange their mass with the surrounding flow. The concentration decreases moving far from the source as a consequence of the dispersion of the released N particles around an imaginary mean trajectory, a purely convective phenomena.

On the contrary, molecular diffusion processes are not negligible in moments of concentration other than the mean. This is demonstrated by means of a dimensional analysis of the terms in the equation for the evolution of the concentration variance, described by the following equation:

$$\frac{\partial \sigma_c^2}{\partial t} = -\frac{\partial}{\partial x_j}\left(\overline{u}_j \sigma_c^2 + \overline{u_j' c'^2} - k\frac{\partial \sigma_c^2}{\partial x_j}\right) - 2\overline{u_j' c'}\frac{\partial C}{\partial x_j} - 2D\left(\overline{\frac{\partial c'}{\partial x_j}\frac{\partial c'}{\partial x_j}}\right) \tag{3.9}$$

On the left side of Equation 3.9, the terms under the divergence operator are fluxes of convective or diffusive origin. Their role is to redistribute the variance in the flow. The second term on the left side of the equation is a source of variance. The last term is the dissipation of variance ε_c.

To evaluate the orders of magnitude of the terms in Equation 3.9 and to better understand the role of molecular diffusion in a scalar transport, such equation is written in a non-dimensional form. To this purpose, an appropriate set of scales is chosen for the turbulent boundary layer: the length scales are the boundary layer depth δ and the Kolmogorov lenght scale η (defined in Equation 2.9), the velocity scale is the free stream velocity U_∞, and $\Delta c = M_q/(U_\infty \delta^2)$

is the concentration scale, M_q being the mass flow of contaminant. The non-dimensional quantities are defined as: $x_i^* = x_i/\delta$, $u_i^* = u_i/U_\infty$, $C^* = C/\Delta c$ and $\sigma_c^* = \sigma_c/\Delta c$. Assuming steady conditions and introducing non-dimensional variables, Equation 3.9 can be rewritten as:

$$\frac{U_\infty \Delta c^2}{\delta}\left(\overline{u}_j^* \frac{\partial \sigma_c^{2*}}{\partial x_j^*}\right) = -\frac{U_\infty \Delta c^2}{\delta}\left(\overline{u_j'^* c'^{*2}}\frac{\partial C*}{\partial x_j^*}\right) - \frac{U_\infty \Delta c^2}{2\delta}\left(\frac{\partial}{\partial x_j^*}\overline{c'^{2*}u_j'^*}\right) - \\ + \frac{D\Delta c^2}{\delta^2}\left(\frac{\partial^2 \sigma_c^{2*}}{\partial x_j'^2}\right) - \frac{D\Delta c^2}{\eta^2}\left(\frac{\partial c'^*}{\partial x_j^*}\right)^2. \tag{3.10}$$

Dividing by $(U_\infty \Delta c^2)/\delta$, we have:

$$\overline{u}_j^* \frac{\partial \sigma_c^{2*}}{\partial x_j^*} = -\overline{u_j'^* c'^{*2}}\frac{\partial C^*}{\partial x_j^*} - \frac{1}{2}\frac{\partial}{\partial x_j^*}\overline{c'^{2*}u_j'^*} + \frac{D}{U_\infty \delta}\left(\frac{\partial^2 \sigma_c^{2*}}{\partial x_j'^2}\right) - \frac{D}{U_\infty \eta}\left(\frac{\partial c'^*}{\partial x_j^*}\right)^2. \tag{3.11}$$

The term $\frac{D}{U_\infty \delta}\left(\frac{\partial^2 \sigma_c^{2*}}{\partial x_j'^2}\right)$ is the transport of variance by molecular diffusion. This phenomenon transports σ_c (an average value) on length scales of the order of the boundary layer depth δ. The coefficient $D/U_\infty\delta$ is equal to the reciprocal of the Peclet numbers and, being very small in atmospheric turbulent flows, can be neglected. The last term on left side, $\frac{D}{U_\infty \eta}\left(\frac{\partial c'^*}{\partial x_j^*}\right)^2$, is the dissipation of concentration fluctuations by molecular diffusion. This phenomenon transports a fluctuating quantity on a length scale η, the Kolmogorov length scale, where $\eta << \delta$, characteristic of mass transfers by molecular diffusion. The Kolmogorov length scale η can be estimated as (Tennekes and Lumley, 1972):

$$\frac{\eta}{\delta} \sim \frac{U_\infty \eta}{\nu} \sim Re^{-3/4}. \tag{3.12}$$

The dependence on Re explicits the influence of the flow conditions on the transport of a scalar and on the statistics of concentration. The term $D/U_\infty\eta$ is of order of ~ 1 and can not be neglected in Equation 3.11. Equations for the third and fourth moments of concentration are dependent on the Reynolds number, as it is the case of the variance. For brevity these equations are not reported since they do not provide further information from the conceptual point of view.

Re is not the only parameter influencing the transport of a scalar in the TBL. Dispersion phenomena also depends on other parameters that arise when imposing specific boundary conditions.

Generally speaking, considering the dispersion of a pollutant plume emitted by a localised source, the concentration statistics at a given position (x, y, z) is function of a series of controlling parameters:

$$(c - C)^n = f\left(x, y, z, d, h_s, u_s, M_q, z_0, u_*, U_\infty, \delta, D, \nu\right). \tag{3.13}$$

Some of them depend on the source characteristics, as the source diameter d, the source elevation h_s and the source outlet velocity u_s. Others are fixed by the

characteristics of the turbulent boundary layer, this is the case of the roughness length z_0, the friction velocity u_*, the free stream velocity U_∞, the boundary layer depth δ, the molecular diffusivity D and the kinematic viscosity ν.

To identify the other governing parameters we can express Equation 3.13 in non-dimensional form as:

$$\frac{\overline{(c-C)^n}}{\Delta c} = f_2\left(\frac{x}{\delta}, \frac{y}{\delta}, \frac{z}{\delta}, \frac{z_0}{\delta}, \frac{u_*}{U_\infty}, \frac{u_s}{U_\infty}, \frac{h_s}{\delta}, \frac{d}{\delta}, Re, Sc\right), \tag{3.14}$$

where $Sc = \nu/D$ is the Smidth number.

If we assume that the dispersion process takes place within a fully turbulent boundary layer, characterised by the asymptotical conditions $z_0/\delta \to 0$ and $Re \to \infty$, implying a self-similarity of the velocity field, the ratio u_*/U_∞ becomes an invariant dynamical parameter. This allows the reduction of Equation 3.14 to

$$\frac{\overline{(c-C)^n}}{\Delta c} = f_3\left(\frac{x}{\delta}, \frac{y}{\delta}, \frac{z}{\delta}, \frac{u_s}{U_\infty}, \frac{h_s}{\delta}, \frac{d}{\delta}, Re, Sc\right). \tag{3.15}$$

When measuring the dispersion of a scalar, one wish to suppress the influence of the source, as if the scalar was emitted by an infinitely small source whose presence does not influence the flow dynamics. In our experimental campaign we have tested the influence of three parameters: d/δ, h_s/δ and u_s/U_∞.

To understand the influence of the source size d/δ on concentration fluctuations, it is useful to refer to the conceptual framework developed by Gifford (1959). In Gifford model, the spread of a plume of contaminant is led by two phenomena: a meandering movement of the instantaneous plume, causing the displacement of the mass center, and the relative dispersion, or spreading, of the plume particles relative to the mass center position. The plume mean concentration profiles are Gaussian and their spread σ is calculated by summing the meandering and the relative dispersion contributions, respectively σ_m and σ_r :

$$\sigma^2 = \sigma_r^2 + \sigma_m^2. \tag{3.16}$$

These phenomena can be considered as statistically independent, since they are related to length scales separated by some orders of magnitude. The predominance of one of the two phenomena depends on the plume scales compared to the turbulence scales, at a given distance downwind. In the near field, if a small enough source (having a small size compared to the local turbulence scales) is considered, meandering is the major contribution to concentration fluctuations. To understand the influence of the source size on the meandering motion, for a short fetch downstream x we can write (Fackrell and Robins, 1982a):

$$\sigma_m^2 \sim \sigma_v x/\overline{u} \tag{3.17}$$

σ_v is the lateral turbulence level and $\overline{u}$ the mean wind speed, whereas:

$$\sigma_r^2 \sim \delta_v x/\overline{u} \tag{3.18}$$

where δ_v is the initial relative dispersion speed of the instantaneous plume. Since $\delta_v << \sigma_v$, the intensity of concentration fluctuations, σ_c, can be written as:

$$1 + \sigma_c \simeq \sigma_m^2/\sigma_r^2 \simeq (\sigma_0^2 + (\sigma_v x/\overline{u})^2)/\sigma_0^2 \tag{3.19}$$

σ_0 is the initial spread due to the source size and is equal to the source diameter. Thus, for $\sigma_\theta = \sigma_v/\overline{u}$, it follows that:

$$\sigma_c \simeq (\sigma_\theta x/\sigma_0)^2. \tag{3.20}$$

At a given position, the smallest source generates the highest concentration fluctuations. Moving far from the source, meandering is not the only source of fluctuations. Since the instantaneous plume begins to spread and develops a fine scale structure also resulting in fluctuations, the relative dispersion becomes more and more influent. Far downwind relative dispersion prevails and the influence of the source size on the concentration statistics is negligible. The role of the source elevation h_s/δ can be expressed by similar arguments, since plumes from ground level and elevated sources are subjected to different turbulence scales and feel the influence of the wall with a different degree.

We finally discuss the influence of u_s/U_∞. In this representation of the problem (Equation 3.15), it is implicitly assumed that the parameter u_s/U_∞ is the sole characterising the dynamical conditions of the flow particles emitted at the source. It is usually supposed, even if not explicitly proved, that if the emission is isokinetic the influence of the emission conditions on the particles trajectories is minimized since, once ejected, the flow particles rapidly take the statistics of the external velocity field. It is therefore recommended that the outlet velocity at the source equals the average velocity of the flow over its height (Fackrell and Robins, 1982a). In this condition, the ratio $u_s/\overline{u}_s = 1$, where $\overline{u}_s$ is the mean velocity in the field at the stack height, and $\overline{u}_s/U_\infty = f(h_s/\delta)$. Therefore, for a given h_s the ratio $u_s/U_\infty = const$ and one expects that the influence of the source, at least for what concerns the mean concentration, is left behind for distances of about ten times the source diameter. Since this aspect deserves to be studied in depth, we analysed the influence of the variation of the ratio u_s/U_∞.

3.4 EXPERIMENTAL SET-UP

The experiments were performed in the atmospheric wind tunnel of the Laboratoire de Mécanique des Fluides et d'Acoustique de l'Ecole Centrale de Lyon, France. Dispersion took place in the TBL described in Chapter 2. The boundary layer height δ was equal to 0.8 m. The reference free-stream velocity U_∞ at the boundary layer height was set at 5 ms^{-1} and the friction velocity was equal to 0.185 ms^{-1}.

Dispersion phenomena from a point source above the array of obstacles were studied by injecting ethane (C_2H_6), a passive tracer neutrally buoyant in air. Concentrations were measured by a Flame Ionization Detector (FID), with a sampling frequency of 1000 Hz. Three source configurations were chosen to investigate the effects of source size and source elevation on the plume dispersion:

GLS. Ground Level Source with an elevation $h_s/\delta = 0.0625$ and a diameter of 3 mm,

ES 3mm. Elevated Source with $h_s/\delta = 0.19$ and a diameter of $d/\delta = 0.00375$ (3 mm),

ES 6mm. Elevated Source with $h_s/\delta = 0.19$ and a diameter of $d/\delta = 0.0075$ (6 mm).

The sources consisted in a metallic tube in form of L and were placed at a distance of 7.5δ from the beginning of the test section, where the boundary layer was fully developed. With the intent of reducing the influence of the vertical bar on the tracer dispersion, the horizontal side was approximately 30 times the source diameter. The source was fully streamlined. Source diameter to boundary layer height ratios (d/δ) are equal to 0.0037 and 0.0075. Given these low values of d/δ and since the first measurement profile is located at a distance of approximately $100d$, according to Fackrell and Robins (1982a), the sources can be effectively considered as point sources. It is also important to notice that the diameters are comprised between the Kolmogorov microscale ($\eta/\delta \sim 0.0001$) and what we identified (in Paragraph 2.5.5) as a mean integral length scale ($L_m/\delta \sim 0.01$). This condition allows for a distinction between the behaviour of a plume issued from the small source (3 mm) with respect to a plume from the big (6 mm) source, since they interact differently with the scales of motion. The meandering motion is predominant on the relative dispersion until the plume size is smaller than the turbulence scale (Gifford, 1959), e. g. L_m, at a certain distance from the source. The mechanism of relative dispersion prevails if the plume scales are of the same order of, or bigger than, L_m.

For each source configuration, the ethane flow was injected in isokinetic conditions, i.e. with an outlet (spatially averaged) velocity $\overline{u}_s$ equal to that in the surrounding at the source height $\overline{u}_s = \overline{u}(z = h_s)$. In this way the release rate employed was low ensuring that the gas was quickly diluted and that passive diffusion started near the source. To investigate the influence of the outlet velocity at the source, we also performed measurements in hypokinetic conditions, that is to say that the outlet velocity was slower than the velocity field at the same height($u_s = 0.03\overline{u}_s$).

Data acquisition was performed with a LabView routine recording time series of the concentration and the volume flow rate injected at the source. Temperature in the test section and atmospheric pressure are also recorded.

3.4.1 Fast Flame Ionisation Detector

Concentration measurements were performed with a Fast Flame Ionisation Detector (FID) by detecting a gas tracer continuously discharged from a point source. Ethane (C_2H_6) was used as tracer in the experiments and was released mixed with air. This gas is not reactive and has a density similar to air - about 1.2 kg/m^3 at 22°C (the temperature in the test section during experiments) and ambient pressure. Thus the release obtained was neutrally buoyant and passive.

The fast flame ionisation detector measures hydrocarbons concentration in air. The physical phenomenon exploited is that when a hydrocarbon is burnt, significant quantities of ions are formed. The amount of ions produced by the combustion is proportional to the concentration of hydrocarbons. Air containing hydrocarbons is aspirated continuously by a tube, which is very thin not to perturb the flow, and is injected into a hydrogen flame. A current is induced by the ions collected to an electrode that is proportional to the concentration of ethane in air (Fackrell, 1980).

The instrument used in this research was an HFR400 Fast FID, produced by Cambustion LTD. The sampling tube was 0.3 m long. The sampling frequency was 1000 Hz, so that concentration spectra were calculated with a frequency up to 300 Hz (Figure 3.1).

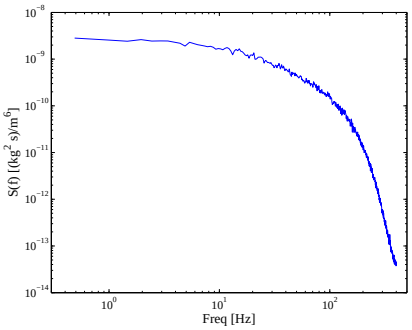

Figure 3.1: A measured concentration spectra.

3.4.2 The experimental protocol

To describe the dispersion from a point source vertical and transversal profiles of fluctuating concentration were recorded at various distances downwind. The first measurement station was placed at $x = 0.3125\delta$ from the source in the x-direction, while the last station was at $x = 5\delta$. The recorded concentration signals were all strongly intermittent. Some characteristic signals are reported in Figure 3.2. In the first image (a) is shown a signal from the elevated source with diameter 6 mm, recorded near the source. This signal is extremely intermittent with its bulk about zero and high peaks with intensity 30 times greater than the mean concentration. At the latest station downstream (Figure 3.2b), the signal becomes less intermittent as the plume entrain clean air and get more mixed. However, concentrated peaks (up to 12 times the mean) are still frequently recorded, due to concentrated puffs advectively transported downwind. A different behaviour in the far field is shown by the ground level source (Figure 3.2c). In this case the signal oscillate about its mean and the intermittency is low. This signal is representative of a plume efficiently mixed by the surface generated turbulence.

While measuring very intermittent signals we have to deal with a wide range of concentration levels and we found that this caused two main difficulties. The first was due to the recording of the signal on the data acquisition card, as we expected a satisfactory dynamic in the lower part of the signal (to record all events happening about zero) and at the same time we wanted the sparks to be recorded too. The second difficulty was connected to the calibration of the instrument, as we wanted the entire signal to be within the limits of calibration. To overcome these two constraints we acted on two fronts: the calibration of the instrument and the concentration level at the source.

Calibration of the FID

The calibration procedure consists in exposing the FID to gases with a known and controlled concentration and in measuring the instrument response in form of voltage (Volt). The relation between concentration in the gas and tension response is usually supposed to be linear. The slope of the calibration line interpolating the data is the calibration coefficient, representing the sensitivity of the instrument (S, measured in ppm/V). By means of the sensitivity, the

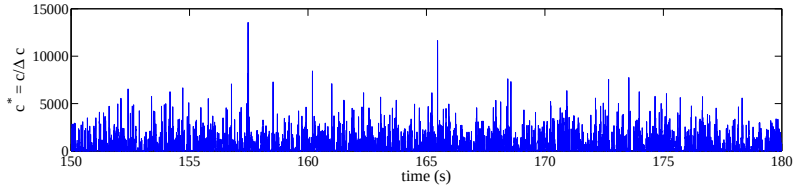

(a) $x/\delta = 0.3125$ ES 6mm, $C^* = 466.88$, $\gamma_c = 0.639$

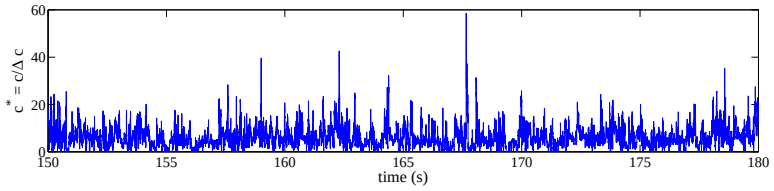

(b) $x/\delta = 5$ ES 6mm, $C^* = 5.80$, $\gamma_c = 0.927$

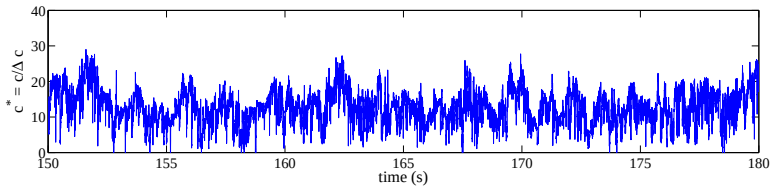

(c) $x/\delta = 5$ GLS, $C^* = 12.80$, $\gamma_c = 0.996$

Figure 3.2: Concentration signals in the near and far fields, on the plume centerline, for elevated and ground level sources. C^* is the signal mean and γ_c its intermittency factor (see Paragraph 3.5.8).

output signal is converted into a concentration signal. The calibration was carried out two-times a day using a mixture from the commerce having a certified concentration equal to 0, 500, 1000 and 5000 ppm. We chose to work with gas bottles because this allowed a controlled concentration easy to be managed compared to the case of using self-made mixtures. At each measurement station, the concentration level of the emitted gas was chosen to assure a good dynamic in the measure and to be within the limits of calibration. This means that for measurements near the source, we worked with very low ethane concentrations to be within the limits of calibration and that far from the source, we increased the tracer to have a satisfactory dynamic. Difficulties in coping with very intermittent signals were also found by other authors (e.g. Fackrell and Robins (1982a)).

The flow control system

The gas emitted at the source was a mixture of air and ethane. Ethane was stocked in bottles, while air was provided by an air compressor. Air passed through an oil-separator and a filter before being injected, to reduce residual oil and dust. The flow control system was composed by two lines (ethane and air) being structured in the same way. The gas flow was adjusted with a mass flow controller and than checked with a flowmetre. In the ethane line, the mass flow controller worked in the range 0-2 Nl/min and should be used for flows within 10 and 100% of the nominal range. The flowmetre allowed a continuous control on the flow. The information was sent to the LabView routine where mass flow was converted in volume flow rate, knowing the temperature in the test section and the atmospheric pression. The volume flow rate was recorded on a file during the concentration acquisition, with a frequency corresponding to the FID sampling one. For each time series of concentration, the correspondent time series of ethane and air flow were recorded too. This was a solution to reduce systematic errors occurring in the flow control stage, but also an advantage for the adimensionalisation of concentration measurements. At last, ethane and air lines converge through a valve and the flow is directed to the source to be injected in the test section.

A second control on the ethane flow was realised *una tantum* with a volumetric counter. The percent difference between the two techniques (mass flow controller and volumetric counter) was calculated as $(Q_{counter} - Q_{meter})/Q_{counter} * 100$ (Figure 3.3). In the range of operation of the mass flow controller (from 12 to 120 l/h) the percent difference was 0.5 to 1.5%. At the occurrence, for measurements very close to the source, we worked with ethane flow rates about 3 l/h. In this case we were situated outside the working range of the instrument and the percent difference reached $\pm 3\%$. Therefore, we expect that the measurements near the source are affected by a greater error due to inaccuracies in the ethane flow rate.

Background concentration

The tracer emitted from the source recirculates in the wind tunnel and tend to accumulate in the test section. This causes the Background Concentration (BC) to raise considerably before reaching a steady condition. To integrate this variation in the measurements, the background concentration is measured before

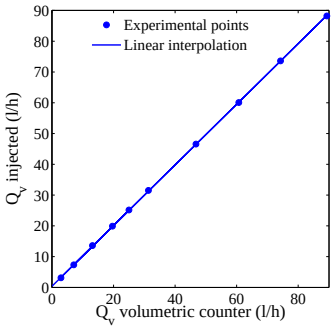

Figure 3.3: Comparison between the ethane volume flow rate injected in the test section (y-axis) and the volume flow rate measured with a volumetric controller (x-axis). The injected flow is measured with a mass flowmetre and converted to a volume flow by the acquisition routine, as atmospheric pressure and test section temperature are known. The points are linearly interpolated with a line of equation y=0.98x+0.4.

and after each measurement point. Two cases can take place: the background rises so that $BC(t = 0s) < BC(t = 300s)$ or the background is stationary, so that $BC(t = 0s) \sim BC(t = 300s)$. The difference between the BC at times 0 and 300 s is then equally shared on the output signal. For a given measurement point, the concentration is obtained as the difference between the output signal and the background noise.

Atmospheric aerosol sampling

Similarly to what has been observed in previous studies (Hall and Emmott, 1991), during the wind tunnel experiments, we found abnormal spikes in the FID output signal. It is believed that their apparition is due to the sampling of atmospheric aerosol. The spikes we measured were of short duration and had peaks equivalent in shape to the ethane signal. Since the FID reacts to ionisable gases, as the tracer, as well as to small combustible particles in the flow, so atmospheric aereosol can interact with the tracer to form anomalous pics. Such peaks were specially visible in the far field, were the plume is diluted, but also present in the near field, still detectable but most of the time camouflaged within the signal. Their intensity was independent of the position. The spike presence does not affect the mean concentration measurements, but is particularly annoying because it hamper the convergence of high order concentration moments which are much more sensibles to anomalies in the signal.

To inquire the origin of the peaks, the background noise was recorded in the wind tunnel while the source was not emitting. In the background noise the spikes produced a strong signal of very short duration with intensity up to 700 ppm (around 7 V). Compared to the concentration signal, the peaks in the background noise had unchanged intensity but smaller amplitude. Output signals are reported in adimensionalised form (Figure 3.4), using a concentration scale $\Delta c = M_q/U_\infty \delta^2$, where M_q is the ethane mass flow injected at the source in kgs^{-1}, U_∞ is the free stream velocity and δ is the boundary layer height. The

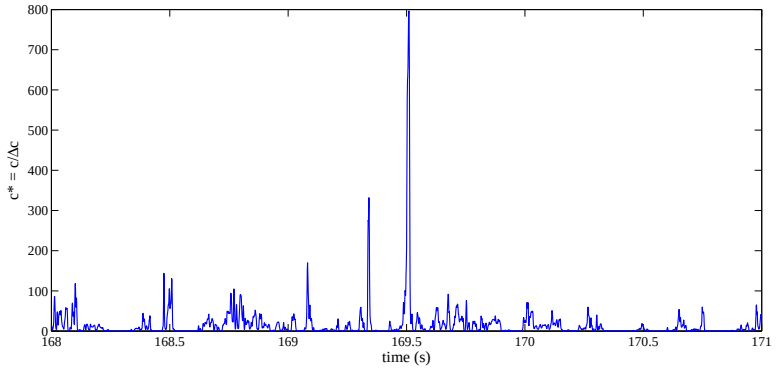

(a) *Signal with atmospheric aerosol sampling (3 seconds).*

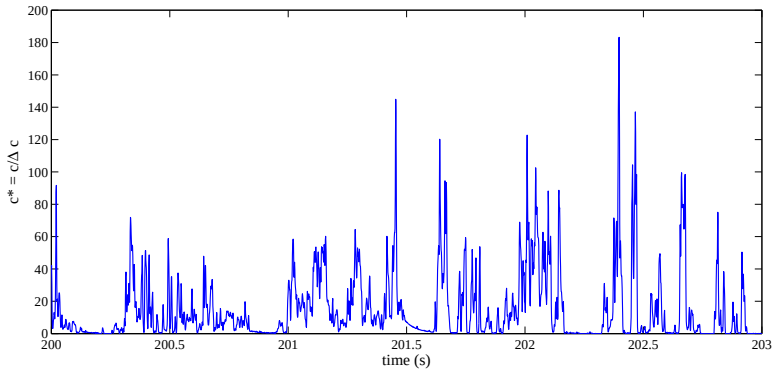

(b) *Signal without atmospheric aerosol sampling (3 seconds).*

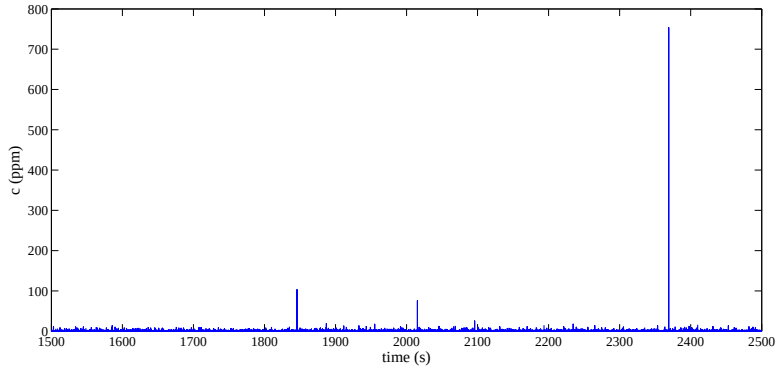

(c) *Background noise with atmospheric aerosol sampling (1000 seconds).*

Figure 3.4: Comparison between adimensionalised concentration signal $c*$ with (a) and without (b) sampling of atmospheric aerosol. Figures refer to the same point situated at a distance $x/\delta = 1.25$, at the centre of the wind tunnel. Figure (c) represents the background noise, concentration is measured in ppm.

background noise is reported in *ppm*.

Two solutions were proposed by Hall and Emmott (1991) to reduce the scale of particulate generated spikes in the output signal. The first was to trap the particles in the sampling line by filtering the line using a small cyclone separator, which was made by winding a few turns of the sampling line into the FID around a small diameter former. However, the performance of the instrument are critically dependent on the low internal volume and short length of the sampling line. We therefore decided not to adopt this technique in order to preserve the 300 Hz frequency response. We retained Hall and Emmott second proposal to filter the output signal applying a low-pass filter. To filter the signal and separate the noise we need to set a threshold frequency. This task was revealed not to be easy. When atmospheric aereosol and ethane puffs are sampled together, the output signal results from some combination of the two effects and spikes have a more complex form. What is more, spikes of medium intensity can not be distinguished from the real signal. This produces an overestimation of the third and fourth moments of concentration. We tested the frequency threshold looking at the impact of filtering the signal on the third and fourth moments. We saw that every small changes in the signal produced a huge effect on the moments and that no threshold allowed the convergence to some result.

As the atmospheric aerosol show pronounced seasonal variations, a new set of concentration measurements was then performed during the months of October and November 2012 and signals compared with the measurements of spring and summer 2012. A study about the seasonal variability in the composition of aerosols was conducted for the northwestern Mediterranean region by Bergametti et al. (1989), who considered some elements which are indicators of the major aerosol sources (soil erosion: aluminium Al and silicon Si; pollution: lead Pb and sulfur S). High variability of atmospheric concentration is observed on times scales of the order of the day, specially for Al and Si showing high concentration episodes frequently observed during summer and spring. Low concentration levels where observed for all elements when the atmosphere was locally washed by rain. Short-term variations of atmospheric concentration are superimposed on a seasonal pattern. Two period of the year are distinguished: higher aerosol concentrations are measured from May to October, and lower from October to April. This difference is due to a seasonal change in continental source strengths and a different removal rate for atmospheric particles between these two periods.

The reduction of aerosols in aerosol concentration in the atmosphere greately reduced the number of spikes in the October and November FID measurements. These measurements cover the entire campaign and we decided not to apply any filter. Consequently, spikes remain in the output signal and contribute to the uncertainty in the measurements.

Convergence and experimental errors

For each measurement point an averaging time of 300 seconds was chosen as it allowed the convergence to be achieved for the moments of concentration. The statistics extracted from the time series include the mean, the standard deviation, the third and the fourth moments of concentration. The convergence of concentration statistics (showed in Figure 3.5) is estimated by means of the

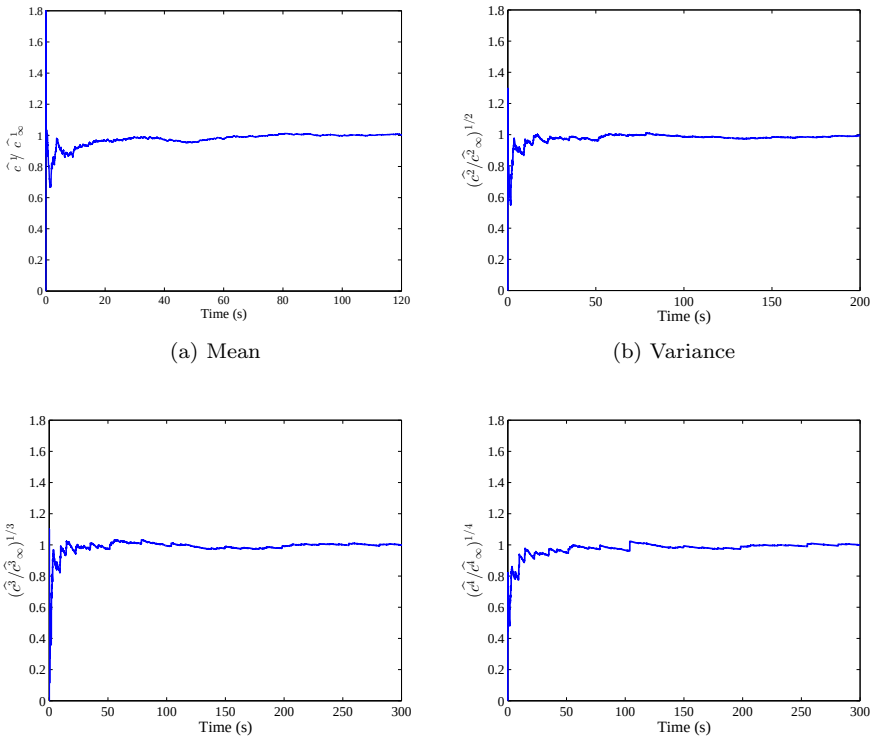

(a) Mean

(b) Variance

(c) Third moment

(d) Fourth moment

Figure 3.5: Convergence of the time series concentration statistics.

ratio $\widehat{c^n}/\widehat{c^n}_\infty$, where $\widehat{c^n}$ is the cumulative mean and $n = 1, 2, 3, 4$ is the order of the moment. $\widehat{c^n}$ is calculated as:

$$\widehat{c^n} = \left(\frac{\sum_{i=1}^{N_t} c_i^n}{N_t} \right)^{1/n} \tag{3.21}$$

where $N_t(t)$ is the number of points composing the signal until the instant t. $\widehat{c^n}_\infty$ is the value of the cumulative mean at the end of the record, after 300 seconds. The Relative Error (RE) is evaluated on the last 20 seconds of acquisition (Δt) as:

$$RE = \frac{\widehat{c^n}(\Delta t) - \widehat{c^n}_\infty}{\widehat{c^n}_\infty} * 100. \tag{3.22}$$

Mean and maximum RE, that are reported in Table 3.1, are about 1%, meaning that a sampling time of 300 seconds is sufficient to reach the convergence of the concentration moments. While increasing the order of the moment, the maximum error becomes slightly larger.

	mean(RE) %	max(RE) %
$\widehat{c^1}$	0.27	0.72
$\widehat{c^2}$	0.16	0.58
$\widehat{c^3}$	0.20	1.09
$\widehat{c^4}$	-0.14	0.95

Table 3.1: Mean and maximum RE of the concentration statistics.

There can be several sources of experimental errors. These include the stochastic uncertainty of the statistics calculated from finite length time series, the uncertainty due to limitations of instrumentation, the calibration errors, the sampling of atmospheric aerosols and the error in the source flow rate. The relative influence of each of these factors is however difficult to estimate a priori. Therefore, in order to quantify the global error characterising the experimental uncertainty, we have collected 20 measurements in four fixed locations with respect to the source. These measurements were performed in different days, with a time interval of several weeks one to the other, and therefore take into account all incertitudes due to the experimental chain. The error was then estimated as two times the standard deviation of the distribution of the 20 values collected for each point. The results are given in Table 3.2 and show that, in the far field, the first two moments of the concentration are affected by an error of 2 %, whereas for the third and the fourth order moments the errors rise up to 4.5 %. In the near field, the measurements were affected by a higher error in the source flow rate, as explained in Paragraph 3.4.2. The uncertainty in the source strength, is reflected linearly on the concentration moments and enhance in particular the error on the first two moment, on the mean and on the standard deviation, whose uncertainty becomes close to that of the source flow control system, i.e. $\pm 3\%$.

	$\widehat{c^1}$	$\widehat{c^2}$	$\widehat{c^3}$	$\widehat{c^4}$
Near field ($x/\delta \leq 0.625$)	2	2	3.5	4.5
Far field ($x/\delta \geq 0.625$)	3	3	3.5	4.5

Table 3.2: Global experimental error (%) of the concentration statistics.

3.5 RESULTS

Concentration measurements are presented in a non dimensional form. The non-dimensional instantaneous concentration c^* is calculated as:

$$c^* = \frac{c}{\Delta c} \; ; \; \Delta c = \frac{M_q}{U_\infty \delta^2} \tag{3.23}$$

where c is the time-dependent concentration, M_q is the ethane mass flow injected at the source and recorded at every time step (kgs^{-1}), U_∞ is the free stream velocity, δ is the boundary layer height. The non-dimensional concentration signal was used to calculate all the statistics in this document.

Our analysis will mainly focus on horizontal profiles of concentration statistics. For completeness, all vertical profiles are presented in the Annexe 7.1.

3.5.1 Concentration PDFs

The one-point Probability Density Function (PDF) of concentration defines the distribution of scalar values found at a fixed point in the plume and provides statistical information on the frequency of concentration above a critical threshold value.

A qualitative analysis of the concentration Probability Density Functions (PDFs) is carried out to investigate the influence of the source size and elevation. PDFs are reported in the non-dimensional form $PDF/(Ndc)$, where N is the number of points on which the PDF is calculated and dc is the amplitude of the concentration classes.

Figure 3.6 shows the PDFs for the ground level source, measured on the plume center line at various distances downwind. The shape of the PDF evolves with increasing the distance from the source. We focused on the bulk of the PDF, that is found at small concentration, even if it is important to remember that also the tail of the distribution is essential in determining the characteristics of the concentration field as, for example, peak concentrations. Near the source the distribution has an exponential form. Going far downwind, the PDF evolves towards a Gaussian distribution, as the plume gradually feels the presence of the ground. At the last measurement station, $x/\delta = 5$, the distribution is perfectly Gaussian and symmetric, with its mean corresponding to the mean concentration.

The concentration distribution of a plume dispersing in the wake of a ground level source was studied by means of a conceptual model by Villermaux and Duplat (2003), who demonstrated that the concentration PDF is well described by a family of one-parameter gamma distributions with the following form:

$$p(\chi) = \frac{k^k}{\Gamma(k)} \chi^{k-1} exp(-k\chi), \tag{3.24}$$

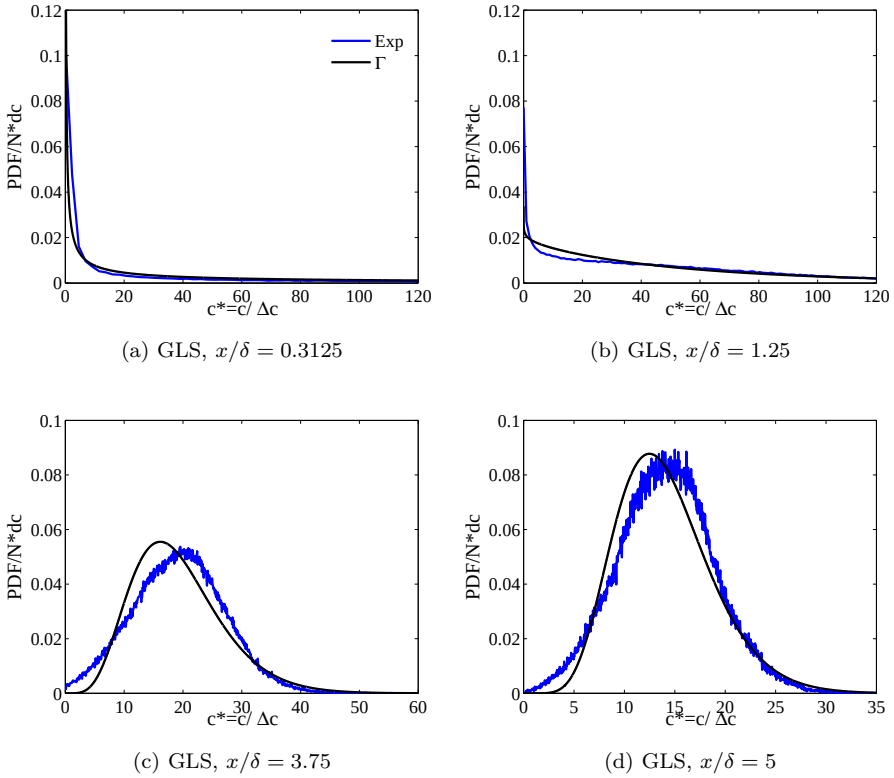

(a) GLS, $x/\delta = 0.3125$

(b) GLS, $x/\delta = 1.25$

(c) GLS, $x/\delta = 3.75$

(d) GLS, $x/\delta = 5$

Figure 3.6: Probability density functions on the plume centre line, at a growing distance downstream for the emission from a ground level source. Comparaison with the gamma distribution.

where $\Gamma(x)$ is the gamma function and $\chi \equiv c/\overline{c}$ is the normalised concentration ($\overline{c}$ being the ensemble average of the instantaneous concentration c). Equation 3.24 depends on a single parameter k, which specifies the gamma distribution, and that can be related to the concentration statistics as $k = \overline{c}^2/\sigma_c^2$, being σ_c^2 the concentration variance. Lately, Yee and Skvortsov (2011) showed by means of experimental data, that the gamma distribution well approximated the evolution of the concentration PDF along the mean-plume centreline of a ground level continuous point source in a wall-shear layer. They also provided a prediction of the downstream evolution of the parameter k and demonstrated that k has a power law dependency on x.

The gamma distribution was compared to our experimental PDFs in Figure 3.6 and in Figure 3.7. It is interesting to see that there is a general agreement between Equation 3.24 and experimental data, since the gamma distribution is rather efficient in changing shape while increasing the distance from the source, therefore passing from an exponential-like distribution to something close to a Gaussian. Particularly close to the source, the gamma distribution clearly agrees with experimental data. In the far field, however, we observe some discrepancies about the position of the maximum of the distribution.

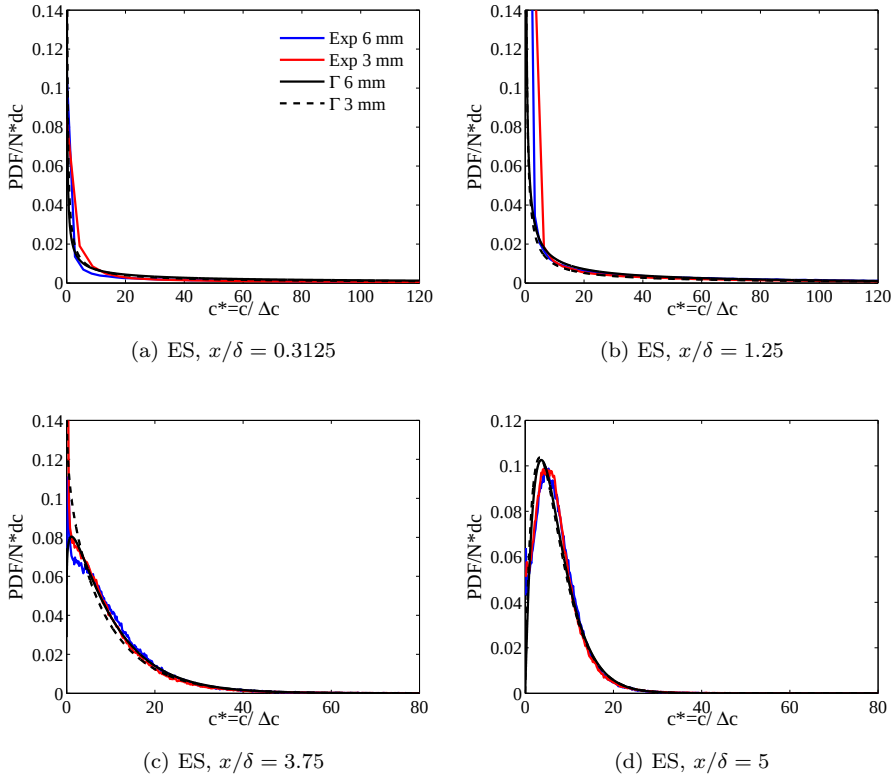

(a) ES, $x/\delta = 0.3125$

(b) ES, $x/\delta = 1.25$

(c) ES, $x/\delta = 3.75$

(d) ES, $x/\delta = 5$

Figure 3.7: Probability density functions on the plume centre line, at a growing distance from the source, for the two elevated sources with 3 mm and 6 mm diameter. Comparaison with the gamma distribution.

The gamma distribution was also compared to the experimental PDFs obtained with measurements in the case of the elevated sources. PDFs were measured on the plume center line at various distances from the source and are shown in Figure 3.7. Also in this case the shape of the PDF evolves for increasing distances from the source: from exponential-like to Gaussian.

The PDFs at increasing distances from the source for ground-level and elevated emissions are significantly different one to the other. However, differences between PDFs on signals within plumes emitted from sources of different size can not be clearly identified. Only small differences are observed between the experimental PDFs of the 3 mm and the 6 mm elevated source in the near field. Higher concentration values about zero are more frequently measured for the smaller 3 mm source, as a consequence of the more fluctuating character of the plume issued from a small point source. Moving far downwind the difference between the two sources almost disappears and it seems that the source size has no influence on the PDF. The gamma distribution do not allow for any direct distinction between the two source dimensions, even though the parameter k includes implicitly in its definition the consequences on concentration fluctuations that depend on the source size. Nevertheless, the plot of the gamma

distribution for the two source sizes in Figure 3.7 do not show a recognisable influence of the source size. To understand which are the effects of the source dimension on concentration fluctuations we can not rely on PDFs but we can instead investigate other concentration statistics.

3.5.2 Mean concentration field

The non-dimensional mean concentration C^* is calculated as:

$$C^* = \frac{1}{N}\sum_{j=1}^{N} c_j^*, \tag{3.25}$$

where c^* is the non-dimensional instantaneous concentration and N the number of samples in the time-series.

Transversal profiles of the mean concentration downwind the source are shown in Figure 3.8 for the case of the Elevated Sources (ES) and in Figure 3.9 for the case of the Ground Level Source (GLS). Vertical profiles are reported in Figure 3.10 for the case of the Elevated Sources (ES) and in Figure 3.11 for the case of the Ground Level Source (GLS).

For both ES and GLS, transverse profiles measured at the source height are satisfactory reproduced by a Gaussian distribution of the type:

$$C(x,y) = C_{max}(x)\ exp\left(-\frac{y^2}{2\sigma_y^2}\right). \tag{3.26}$$

Vertical profiles were measured on the plume axis. When the plume is at the ground level, the Gaussian distribution with total reflection on the ground is the most suited to reproduce the concentration distribution in the vertical direction:

$$C(x,z) = C_{max}(x)\left[exp\left(-\frac{(z+h_s)^2}{2\sigma_z^2}\right) + exp\left(-\frac{(z-h_s)^2}{2\sigma_z^2}\right)\right]. \tag{3.27}$$

For the ES, the plume touch the ground at $x/\delta = 2.5$, while in the GLS case the plume is at the ground level soon after the release. These Gaussian distributions were fitted to mean concentration profiles and used to estimate the plume spreads, σ_y and σ_z, in the y- and z- directions (see Paragraph 3.5.3).

Mean concentration profiles do not show any particular effect of the source size. Only the profile very close to the source ($x/\delta = 0.3125$) shows a little scatter, which should be attributed to the influence of the source conditions on the concentration field. This subject is analysed in Paragraph 3.5.7, where we examined the velocity field in the proximity of the emission point and we observed that the plume is affected by the wake of the source and by the jet effect resulting from the isokinetic emission.

The effect of source elevation is shown in Figure 3.9, where transversal profiles for the GLS and ES with the same size are compared. As soon as the GLS plume approaches the ground, its mean concentration becomes larger than the one measured for the ES, due to the plume reflection. The GLS maximum mean concentration is about two times the concentration reached by the ES plume. Only in the very near field the situation is reversed and the ES plume is found to have a higher concentration (Figure 3.9a). This situation can be explained by

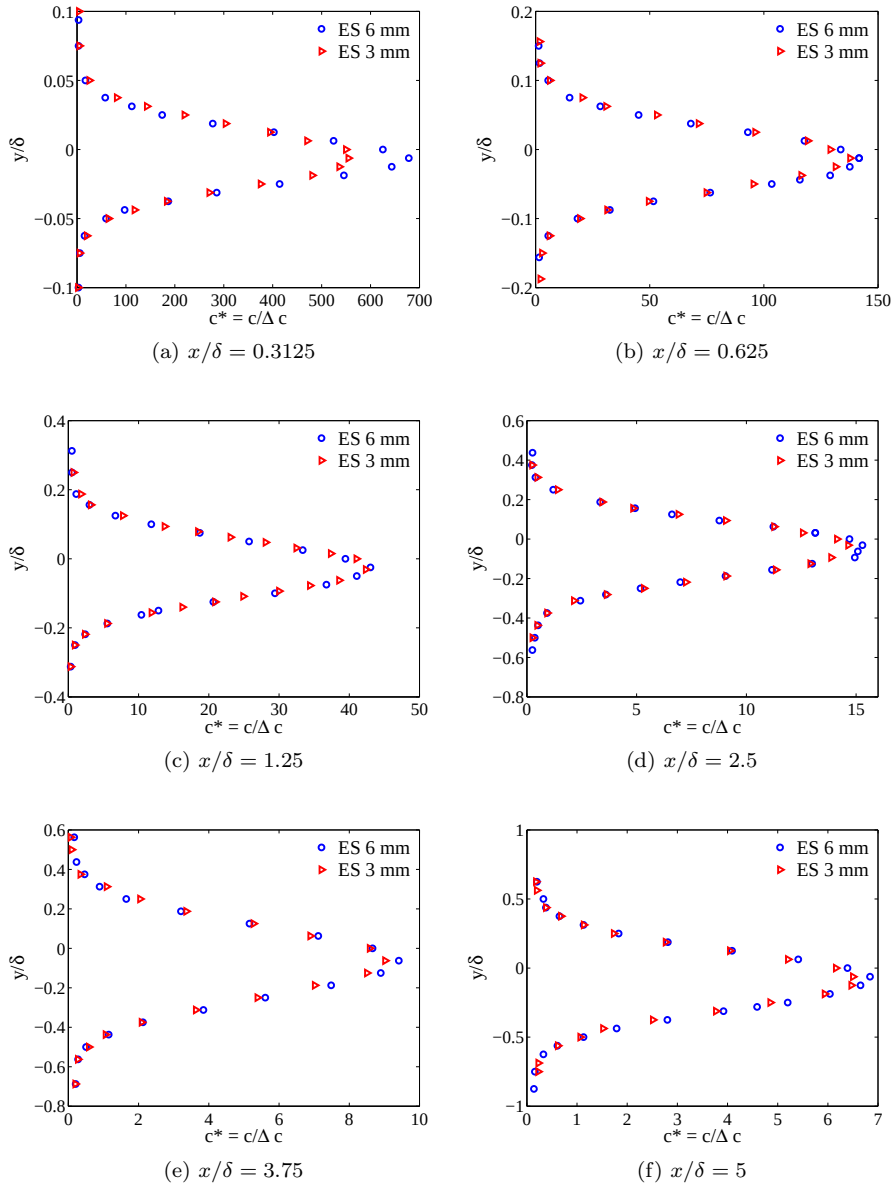

(a) $x/\delta = 0.3125$ (b) $x/\delta = 0.625$

(c) $x/\delta = 1.25$ (d) $x/\delta = 2.5$

(e) $x/\delta = 3.75$ (f) $x/\delta = 5$

Figure 3.8: Transversal profiles of non-dimensional mean concentration for the elevated sources, at various distances downwind. Profiles were measured at the source heigth, $z_s/\delta = 0.19$. Blue circles: source diameter 6 mm; red triangles: source diameter 3 mm.

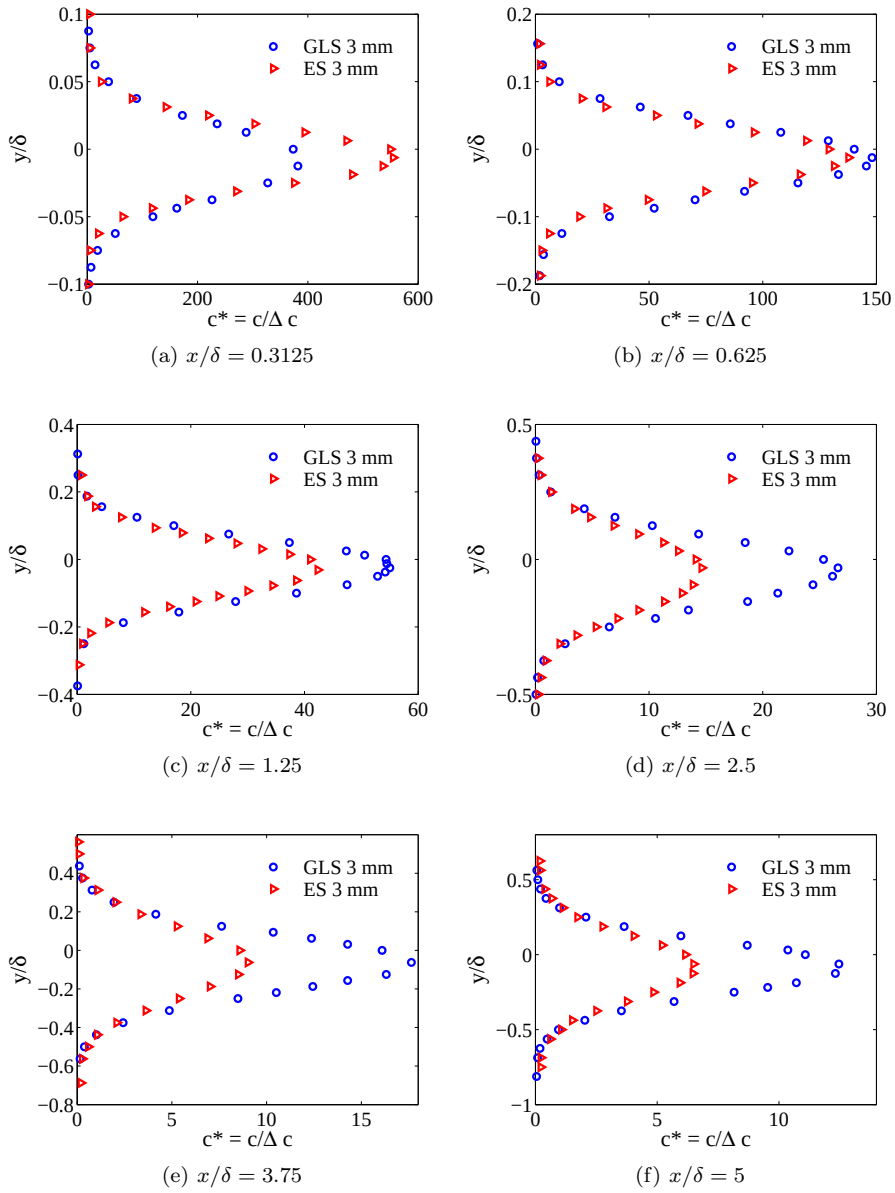

(a) $x/\delta = 0.3125$ (b) $x/\delta = 0.625$

(c) $x/\delta = 1.25$ (d) $x/\delta = 2.5$

(e) $x/\delta = 3.75$ (f) $x/\delta = 5$

Figure 3.9: Transversal profiles of non-dimensional mean concentration for the ground level source with diameter 3 mm, at various distances downwind. Profiles were measured at the source heigth, $z_s/\delta = 0.0625$. A comparison is made with the elevated source having the same diameter.

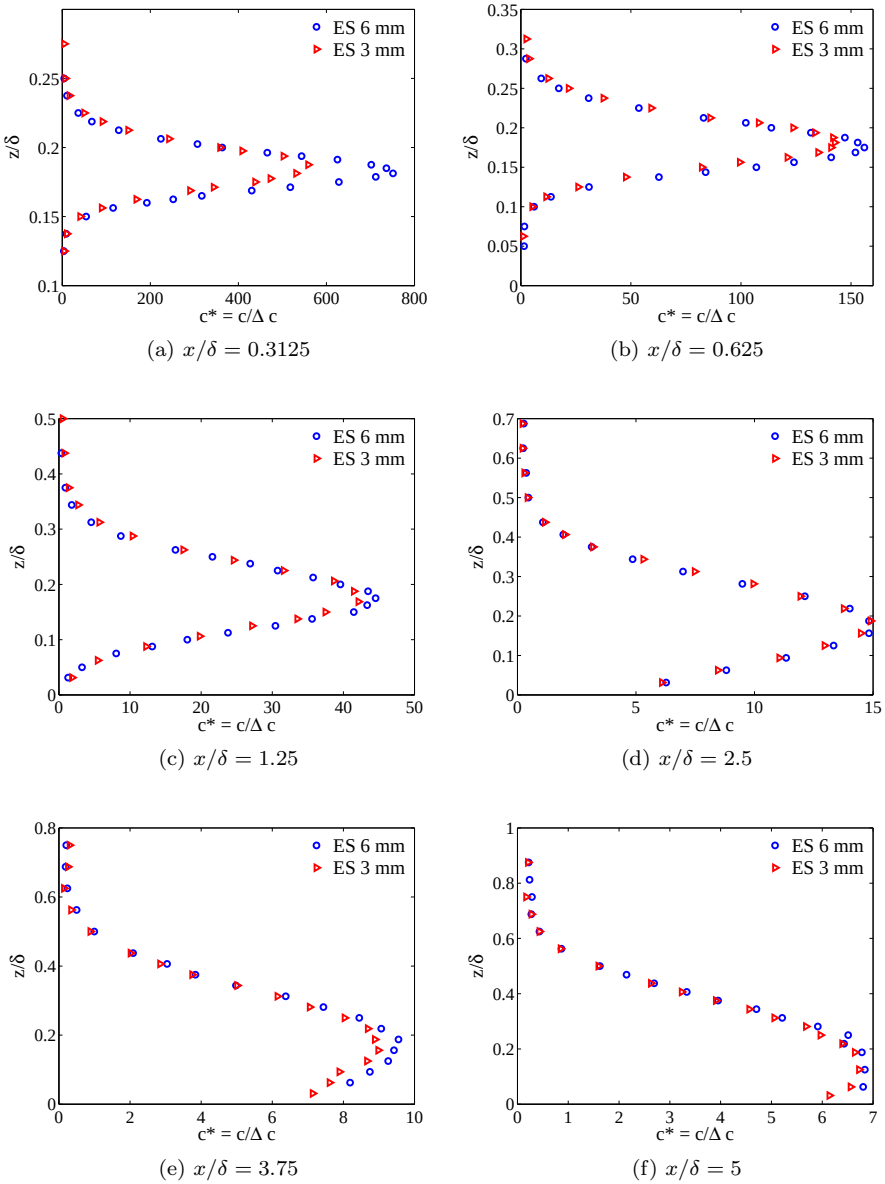

(a) $x/\delta = 0.3125$ (b) $x/\delta = 0.625$

(c) $x/\delta = 1.25$ (d) $x/\delta = 2.5$

(e) $x/\delta = 3.75$ (f) $x/\delta = 5$

Figure 3.10: Vertical profiles of non-dimensional mean concentration for the elevated sources, at various distances downwind. Profiles were measured on the plume axis. Blue circles: source diameter 6 mm; red triangles: source diameter 3 mm.

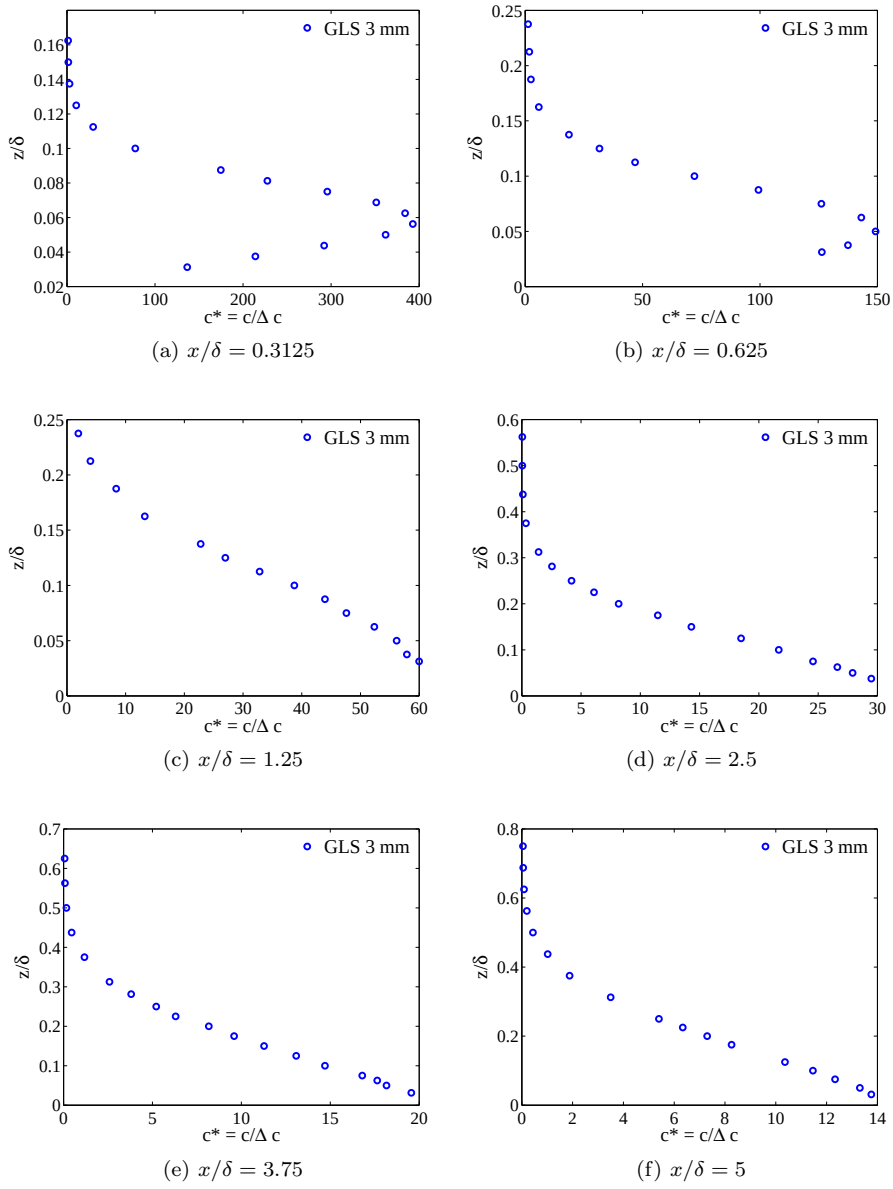

(a) $x/\delta = 0.3125$ (b) $x/\delta = 0.625$

(c) $x/\delta = 1.25$ (d) $x/\delta = 2.5$

(e) $x/\delta = 3.75$ (f) $x/\delta = 5$

Figure 3.11: Vertical profiles of non-dimensional mean concentration for the ground level source, at various distances downwind. Profiles were measured on the plume axis. The source diameter is equal to 3 mm.

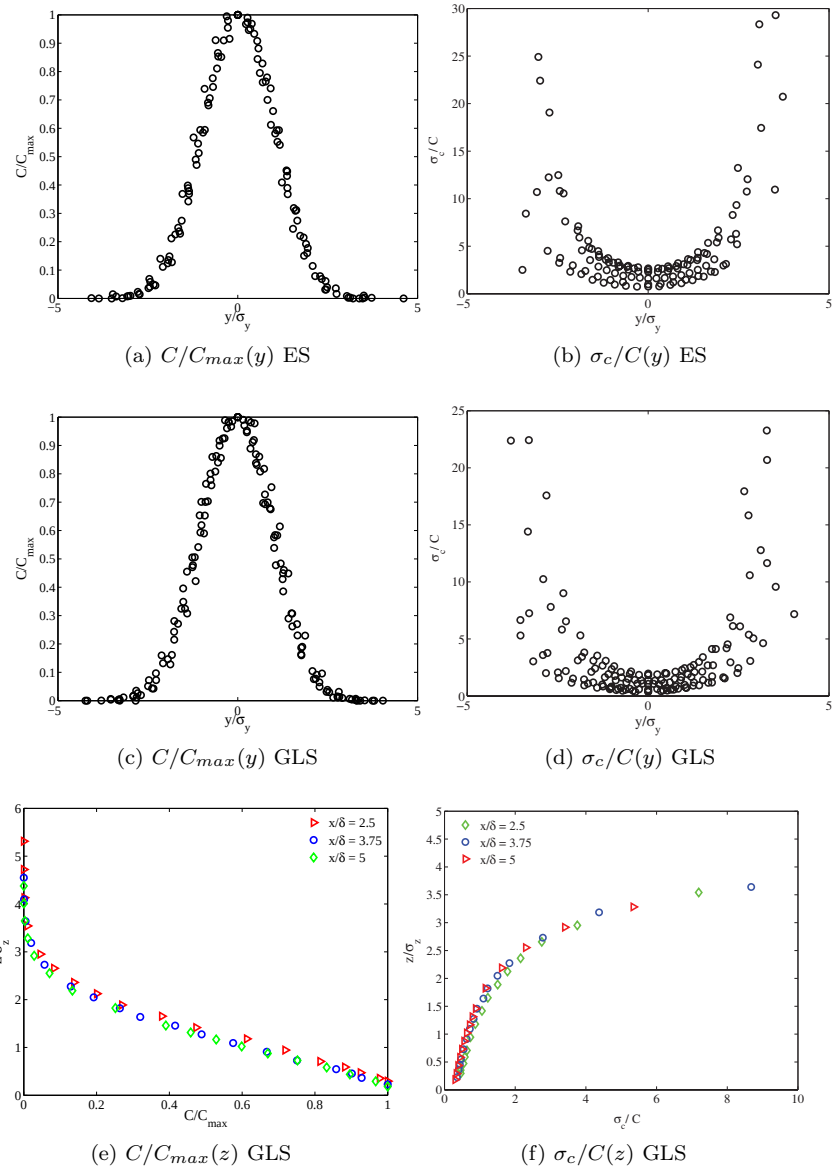

(a) $C/C_{max}(y)$ ES (b) $\sigma_c/C(y)$ ES

(c) $C/C_{max}(y)$ GLS (d) $\sigma_c/C(y)$ GLS

(e) $C/C_{max}(z)$ GLS (f) $\sigma_c/C(z)$ GLS

Figure 3.12: Self-similarity of transversal and vertical profiles of the non-dimensional mean concentration and of the intensity of concentration fluctuations. Elevated source: a) $C/C_{max}(y)$, b) $\sigma_c/C(y)$. Ground level source: c) $C/C_{max}(y)$, d) $\sigma_c/C(y)$, e) $C/C_{max}(z)$, f) $\sigma_c/C(z)$.

the fact that the GLS plume touches the ground immediately after the release, as it can be seen in Figure 3.11.

Transverse profiles of mean concentration have a self-similar form (as shown in Figure 3.12a for the ES case and in Figure 3.12c for the GLS case) when non-dimensionalised as C/C_{max} and plotted with respect to y/σ_y. The intensity of concentration fluctuations σ_c/C also approaches a similar form, especially when moving away from the source, when plotted with respect to y/σ_y, as shown in Figures 3.12b (ES) and 3.12d (GLS).

Conversely, vertical profiles are generally far from self-similarity. Vertical profiles of mean concentration becomes self similar only when the plume touch the ground and its maximum concentration is situated at ground level. The GLS concentration field becomes self-similar starting from $x/\delta = 2.5$, as shown in Figure 3.12e, where vertical mean concentration profiles C/C_{max} collapse when plotted with respect to z/σ_z. The same behaviour is observed for the intensity of concentration fluctuations (Figure 3.12f) which is self-similar in the vertical direction. For what concerns the elevated sources, in the range of distances investigated, vertical profiles never attain self-similarity.

3.5.3 Plume spreads

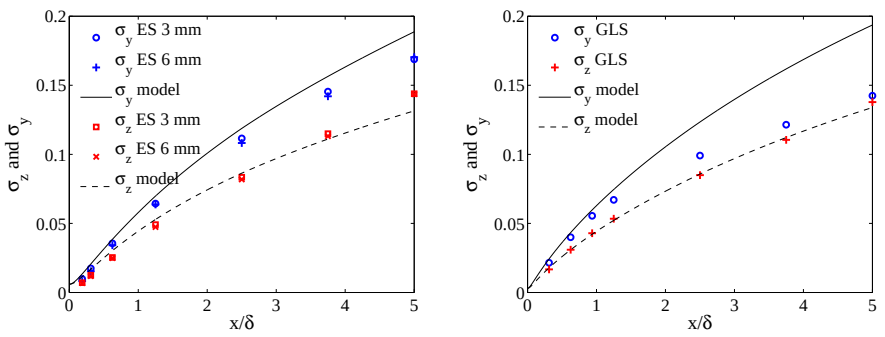

(a) σ_z *and* σ_y *for the ES case.*

(b) σ_z *and* σ_y *for the GLS case.*

Figure 3.13: Experimental and modelled plume spreads σ_z and σ_y downstream the source. The modelled spreads are calculated by means of Equation 3.29 and 3.28

Vertical and transversal plume spread (σ_z and σ_y) are shown in Figure 3.13. For both the ES and the GLS, in the near field as well as in the far field, vertical spread was observed to be less than lateral. The effect of the source size on the ES spreads is negligible: the two courbes collapse at every downwind station.

Plume spread are modelled moving from Taylor's dispersion statistical theory, that provides the following relations:

$$\sigma_y^2 = \sigma_0^2 + 2\sigma_v^2 T_{Lv}\left\{t - T_{Lv}\left[1 - \exp\left(-\frac{t}{T_{Lv}}\right)\right]\right\}, \tag{3.28}$$

$$\sigma_z^2 = \sigma_0^2 + 2\sigma_w^2 T_{Lw}\left\{t - T_{Lw}\left[1 - \exp\left(-\frac{t}{T_{Lw}}\right)\right]\right\}, \tag{3.29}$$

where t is the temporal coordinate, σ_w and σ_v are the r.m.s of the vertical and transversal velocity respectively, T_{Lw} and T_{Lv} represent the vertical and transversal Lagrangian time scales and σ_0 denotes the initial spread, that is equal to the source diameter.

Two different parametrisation of the Lagrangian timescales, widely adopted in the literature, have been tested. In the first case these are expressed as:

$$T_{Lw} = \frac{2\sigma_w^2}{C_0\varepsilon} \tag{3.30}$$

$$T_{Lv} = \frac{2\sigma_v^2}{C_0\varepsilon}, \tag{3.31}$$

where C_0 is the Kolmogorov constant and ε is the dissipation rate of turbulent kinetic energy. The best agreement between experimental and modeled plume spreads is obtained for $C_0 = 4.5$ (Figure 3.13). For the elevated source, the model agrees well with experimental data. A satisfactory agreement is also shown for σ_z in the ground level case, while σ_y is overestimated starting from $x/\delta = 1.25$. As shown in Paragraph 2.5.6, it is worth noting that, for this value of C_0, the Lagrangian time scales provided by Equations 3.30 and 3.31 are very close to those computed as:

$$T_{Lw1} \sim \frac{L_{ww}}{\sigma_w} \tag{3.32}$$

$$T_{Lv1} \sim \frac{L_{vv}}{\sigma_y}, \tag{3.33}$$

being L_{vv} and L_{ww} a transversal and a vertical Eulerian Integral Length Scale, respectively. Equation 3.33 is therefore shown to be a suitable and simple model for the Langrangian time scale.

A second model for the estimation of the mean plume spread is obtained through the assumption of similarity in the Lagrangian and Eulerian spectra (Hay and Pasquill (1959), Tennekes (1982) and Fackrell and Robins (1982a)). This is a classical model in which the spread of particles is related uniquely to measurable statistics of the turbulence. In the y-direction the plume spread is calculated as:

$$\sigma_y^2 = \sigma_0^2 + (\sigma_v^2/\overline{u}^2)x^2 \int_0^\infty F_E(k) \left(\frac{\sin kx/2\beta}{kx/2\beta} \right)^2 dk, \tag{3.34}$$

where $k = 2\pi f/\overline{u}$ is the wavenumber, f is the frequency and $F_E(k) = E_E(k)/\sigma_v^2$ is the normalized Eulerian spectrum. In writing Equation 3.34, it is assumed that Eulerian $E_E(k)$ and Lagrangian $E_L(k)$ spectra are related via:

$$E_L(f) = \beta E_E(\beta f), \tag{3.35}$$

β being the ratio between Eulerian and Lagrangian scales (Equation 2.26). Several experimental estimates of β are available and differ significantly one to the other: β is expected to range from $2-3$ to almost 12. Such a variability does not support the request of finding a universal law valid for all turbulent flows. According to Pasquill (1971), precise similarity in the Lagrangian and Eulerian spectra cannot be supported, but experience shows that the crucial requirement is to prescribe correctly the ratio of the integrals of the spectra, and then the

departure from similarity in shape is likely to be relatively unimportant. β is a function of the distance from the source and is calculated with the empirical formulation $\beta = \alpha\overline{u}/\sigma_v$, with $\alpha = 0.6$, as suggested by Fackrell and Robins (1982a). This gives $\beta = 7.33$, which falls in the middle of the a typical range of literature data.

The analogous of Equation 3.34 can be written for the vertical plume spread, with the vertical $F_E(k) = E_E(k)/\sigma_w^2$. To take into account the effect of the source dimension, the source diameter σ_0 is included:

$$\sigma_z^2 = \sigma_0^2 + (\sigma_w^2/\overline{u}^2)x^2 \int_0^\infty F_E(k) \left(\frac{\sin kx/2\beta}{kx/2\beta} \right)^2 dk. \tag{3.36}$$

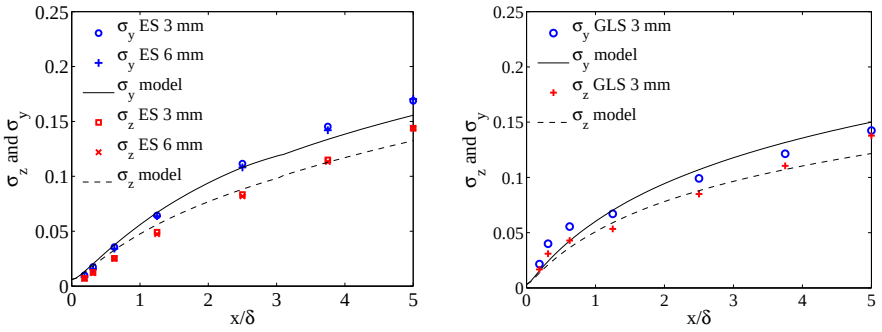

(a) σ_z *and* σ_y *for the ES case.*

(b) σ_z *and* σ_y *for the GLS case.*

Figure 3.14: Comparison between experimental and modelled (Equations 3.34 and 3.36) plume spreads σ_z and σ_y downstream the source.

The comparison of this model with the experimental mean plume spreads is shown in Figure 3.14. In computing the plumes spreads we used the velocity spectra (Paragraph 2.5.3) that were measured at the vertical coordinate of the plume centre of mass, considered at each different distances from the source. In this case, spreads from the ground level source plume are correctly reproduced by the model, that also gives a satisfactory agreement with the σ_z of the elevated source.

Finally, the standard deviations σ_y and σ_z were compared to parametrisations (Weil (1985), Venkatram (1992), Deardroff and Willis (1975)) adopted in several operational dispersion models, such as ADMS (CERC, 2001) and SIRANE (Soulhac et al., 2011). In neutral atmospheric conditions and for an elevated source, the transversal plume spread is given by:

$$\sigma_y^2 = \sigma_0^2 + \left[\frac{\sigma_v t}{(1 + 2.5(u_* t/\delta)^{1/2}} \right], \tag{3.37}$$

where $t = x/\overline{u}_s$, $\overline{u}_s$ being the mean velocity at the source elevation. The vertical plume spread is given by:

$$\sigma_z^2 = \sigma_0^2 + (0.4\sigma_w t)^2. \tag{3.38}$$

The comparison with experiments is reported in Figure 3.15. The agreement is satisfactory for the vertical spread σ_z, while the modelled transversal spread

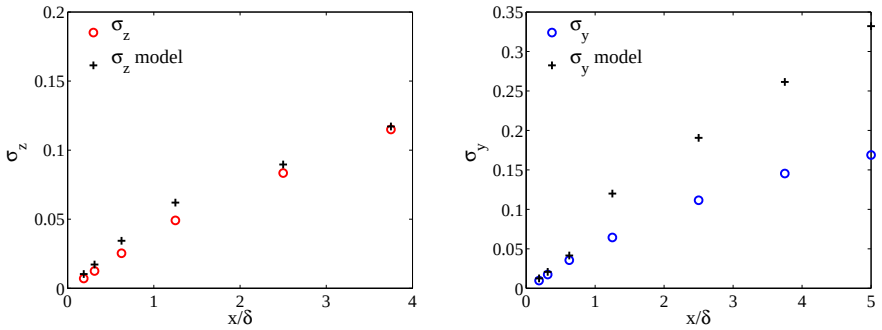

(a) σ_z *for the ES case.* (b) σ_y *for the ES case.*

Figure 3.15: Comparison between the experimental σ_z and σ_y and the ones calculated by means of Equations 3.37 and 3.38, at every downstream position.

σ_y diverge substantially from experiments in the far field. From an analysis of Equation 3.37 it can be shown that this formulation implicitly assumes a Lagrangian time scale $T_{Lv} = \delta/(5u)$, that is about three times the actual time scale, as estimated from experimental results (Paragraph 2.5.6). This difference may be due to the fact that Equation 3.37 takes into account a transversal plume spread due to meandering motion related to low-frequency fluctuations in the atmosphere that is not present in the simulated wind tunnel flow.

In order to compare the plume spread to those measured by Fackrell and Robins (1982b), we have also computed the plume half-widths δ_y and δ_z, defined as the distance in which the maximum concentration falls to its half value. This comparison is shown in Figure 3.16a for the elevated source and in Figure 3.16b for the ground level source. All along, for the ES case, our plume resulted slightly narrower in both the vertical and the transversal directions. Some more discrepancies appear for the GLS in the far field, since our plume seems to grow with a slower rate. However, the overall comparison is satisfying.

The variation of maximum mean concentration $max(C)$ on the planes (y, z) with downstream distance x is shown in Figure 3.16c for the elevated sources and in Figure 3.16d for the ground-level source. Our results are once again compared to Fackrell and Robins's (1982b). For the ES, the maximum approaches the ground, being at ground level only for the furthest downstream position. No influence of the source diameter can be detected, with the exception of the two nearer stations where there is a little scatter between the 3 mm and the 6 mm. Slight differences can be observed between our results and those of Fackrell and Robins (1982b), whose maximal concentrations in the plume axis are generally lower. These differences have to be attributed to the different ratio u_*/U_∞ characterising the two velocity fields (see Paragraph 2.4), that however appear to have a limited influence on the mean concentration field. For the GLS, the maximum mean concentration is situated at the ground level starting from $x/\delta = 1.25$. From this station on, our experimental data superpose with Fackrell and Robins's. Starting from $x/\delta = 1.25$, the GLS maximum mean concentration becomes bigger than the ES one.

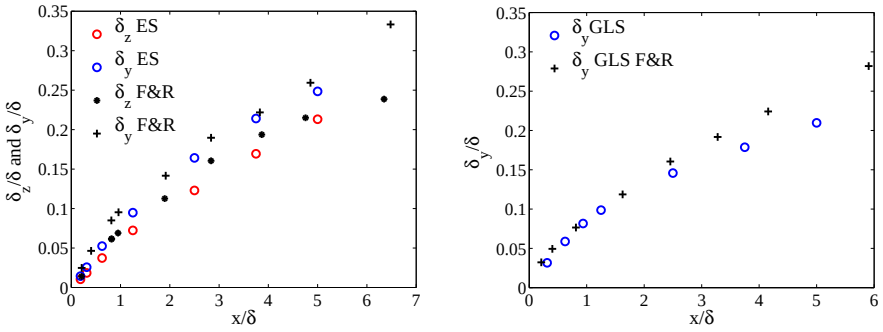

(a) ES: δ_y/δ and δ_z/δ (b) GLS: δ_y/δ

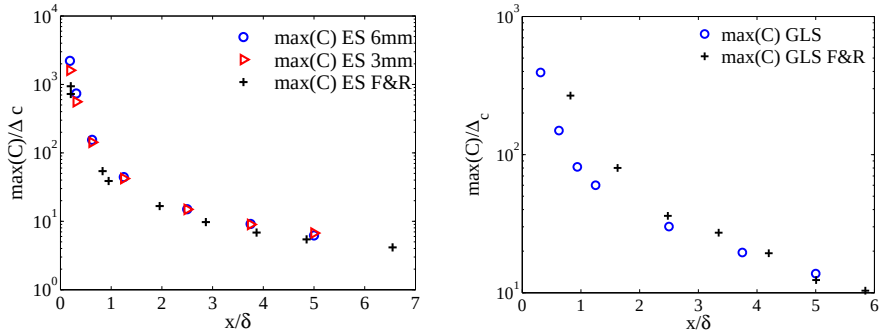

(c) ES: $max(C)/\Delta_c$ (d) GLS: $max(C)/\Delta_c$

Figure 3.16: Vertical and lateral plume half-widths and maximum concentrations, comparison with Fackrell and Robins (1982b) (F&R in the legends).

3.5.4 The concentration standard deviation

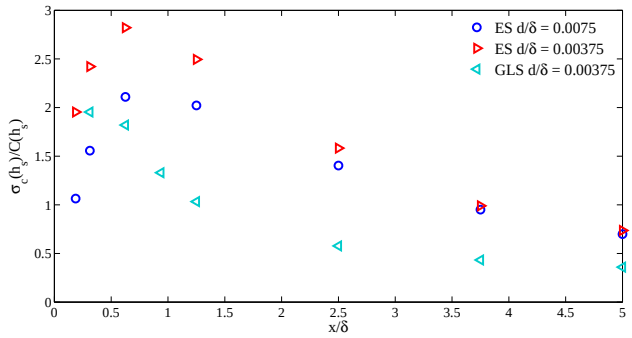

(a) $\sigma_c(h_c)/C(h_c)$

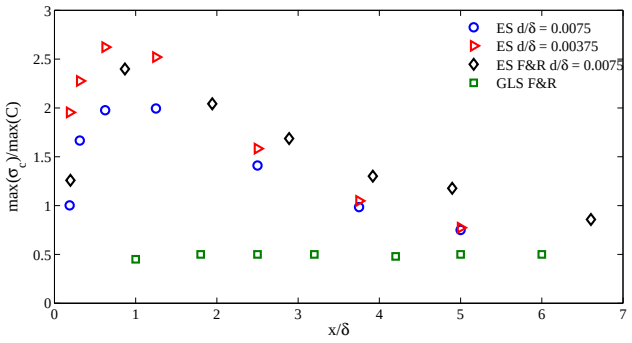

(b) $max(\sigma_c)/max(C)$

Figure 3.17: Development of the intensity of concentration fluctuations estimated as $\sigma_c(h_c)/C(h_c)$ (a) and as $max(\sigma_c)/max(C)$ (b), and comparison with Fackrell and Robins (1982b).

The non-dimensional concentration r.m.s, σ_c^* is calculated as:

$$\sigma_c^* = \left[\frac{1}{N} \sum_{j=1}^{N} (c_j^* - C^*)^2 \right]^{1/2} \tag{3.39}$$

where c^* is non-dimensional instantaneous concentration, C^* is the non-dimensional mean of the time-series and N is the number of samples in the time-series.

Even if the mean field seems not to be influenced by the source dimensions, the other statistics show instead strong source size dependence, and this dependence extends to a considerable fetch.

The intensity of concentration fluctuations at the source level is defined as the ratio $\sigma_c(h_s)/C(h_s)$ between the concentration standard deviation and the mean concentration evaluated at the source elevation (h_s). Figure 3.17a shows the downwind development of the intensity of concentration fluctuations, at every downstream position. We observe that the maximum of the fluctuation intensity occurs close to the source and thereafter the fluctuations decay. This

is particularly true for the elevated source, for which the effects of source size are larger. These effects are important close to the source, where the highest fluctuations result from the small size emissions. The source size influence decreases while increasing the distance from the source: at the latest station the curves seem to converge to a common far field behaviour. Since the ultimate fate of an elevated source is to approach the ground, becoming more or less indistinguishable from a ground level emission, it seems likely that the elevated source results tend towards the ground level ones in the far field.

At the point downwind where the curves converge, the only mechanism responsible of the generation of concentration fluctuations is the relative dispersion. At this point, the plume size is bigger than the turbulence scales and there is no meandering. Concentration fluctuations are generated by turbulent structures with size equal to the integral length scales, therefore it makes sense that the asymptotic value of $\sigma_c(h_s)/C(h_s)$ is dependent on the integral length scales.

The effects of source size on ground level emissions was investigated by Fackrell and Robins (1982a), according to whom the source size has no significant influence(or if there is an influence it is not distinguishable from the experimental scatter) and that details of source conditions and surface roughness are relatively unimportant in determining the fluctuating concentration field downwind of ground level sources. They argue that *"it seems likely that the local flow characteristics near the surface (high turbulence and high shear) and between the three-dimensional roughness elements effectively 'scramble' the concentration field and thereby eliminate the possibility of significant history effects"*. They also show that the fluctuation intensity is always constant downwind a point ground level emission. For what concerns our GLS measurements, the fluctuation intensity is higher close to the source and reaches a constant value at the last three stations downwind. This is due to the fact that our GLS was actually placed at $z/\delta = 0.0625$ (Fackrell and Robins's was at $z/\delta = 0$), so that the plume issued from this source behaves as a ground level starting from the moment when it reaches the ground, at about $x/\delta = 2.5$. Compared to the elevated emission, the ground level generates lower fluctuations. The fluctuation intensity is generally smaller than the one measured for the elevated emission with the same source size.

To compare our results with data from Fackrell and Robins (1982b), we calculated the intensity of concentration fluctuations as they did, that is to say as the ratio of the maximum r.m.s., $max(\sigma_c)$, to the maximum mean, $max(C)$, at every downstream position. The comparison is shown in Figure 3.17b for the ES case with source size $d/\delta = 0.0075$ (3 mm). The two plumes behaves similarly, even if our measurements reach the maximum closer to the source and they generally show a lower intensity of fluctuations. We believe that these differences could be attributed to the different structure of the flow reproduced in the two experiments, especially for what concerns the lateral integral length scales.

A very similar information about concentration fluctuations in the plume can be recovered from the ratios $m^*_{3c}(h_s)/C(h_s)$ and $m^*_{4c}(h_s)/C(h_s)$, reported in Figure 3.18. At growing distance from the emission point, their behaviour is analogous to what we already discussed for $\sigma_c(h_s)/C(h_s)$.

Transversal profiles of concentration standard deviation downwind the source for the elevated sources are presented in Figure 3.19, while for the ground level

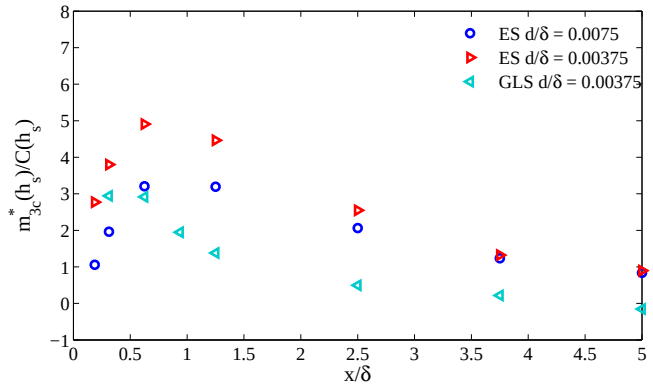

(a) $m^*_{3c}(h_s)/C(h_s)$

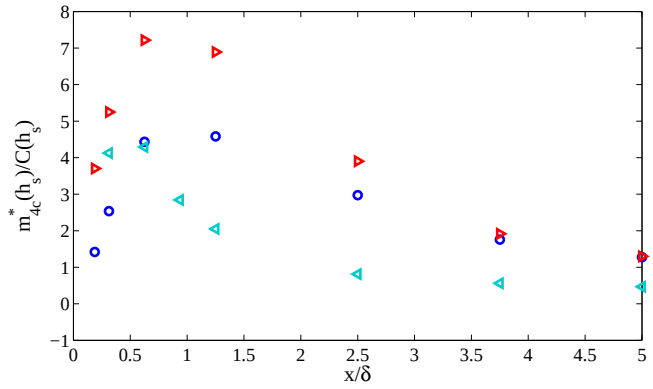

(b) $m^*_{4c}(h_s)/C(h_s)$

Figure 3.18: Stream-wise profiles of $m^*_{3c}(h_s)/C(h_s)$ and $m^*_{4c}(h_s)/C(h_s)$.

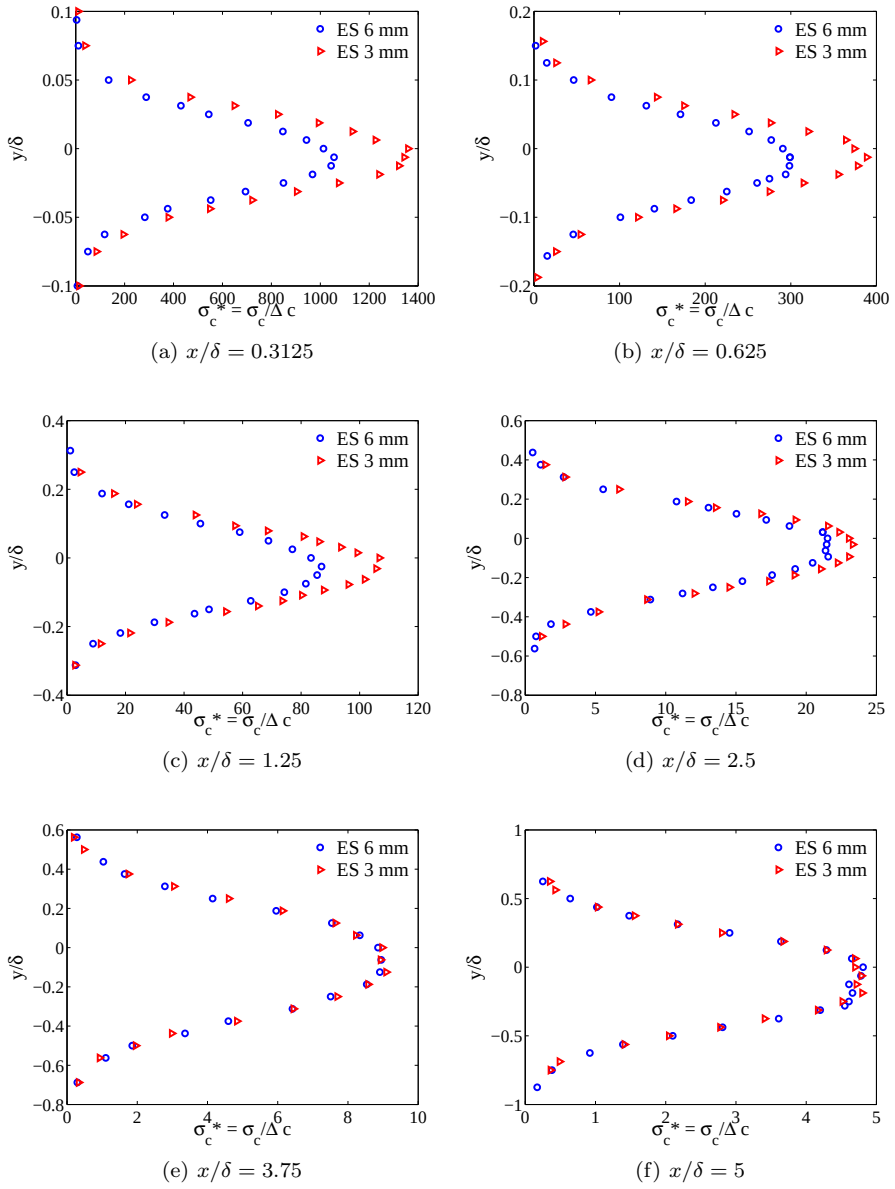

(a) $x/\delta = 0.3125$ (b) $x/\delta = 0.625$

(c) $x/\delta = 1.25$ (d) $x/\delta = 2.5$

(e) $x/\delta = 3.75$ (f) $x/\delta = 5$

Figure 3.19: Transversal profiles of non-dimensional concentration standard deviation for the elevate sources, at various distances downwind. Profiles were measured at the source heigth, $z_s/\delta = 0.19$. Blue circles: source diameter 6 mm; red triangles: source diameter 3 mm.

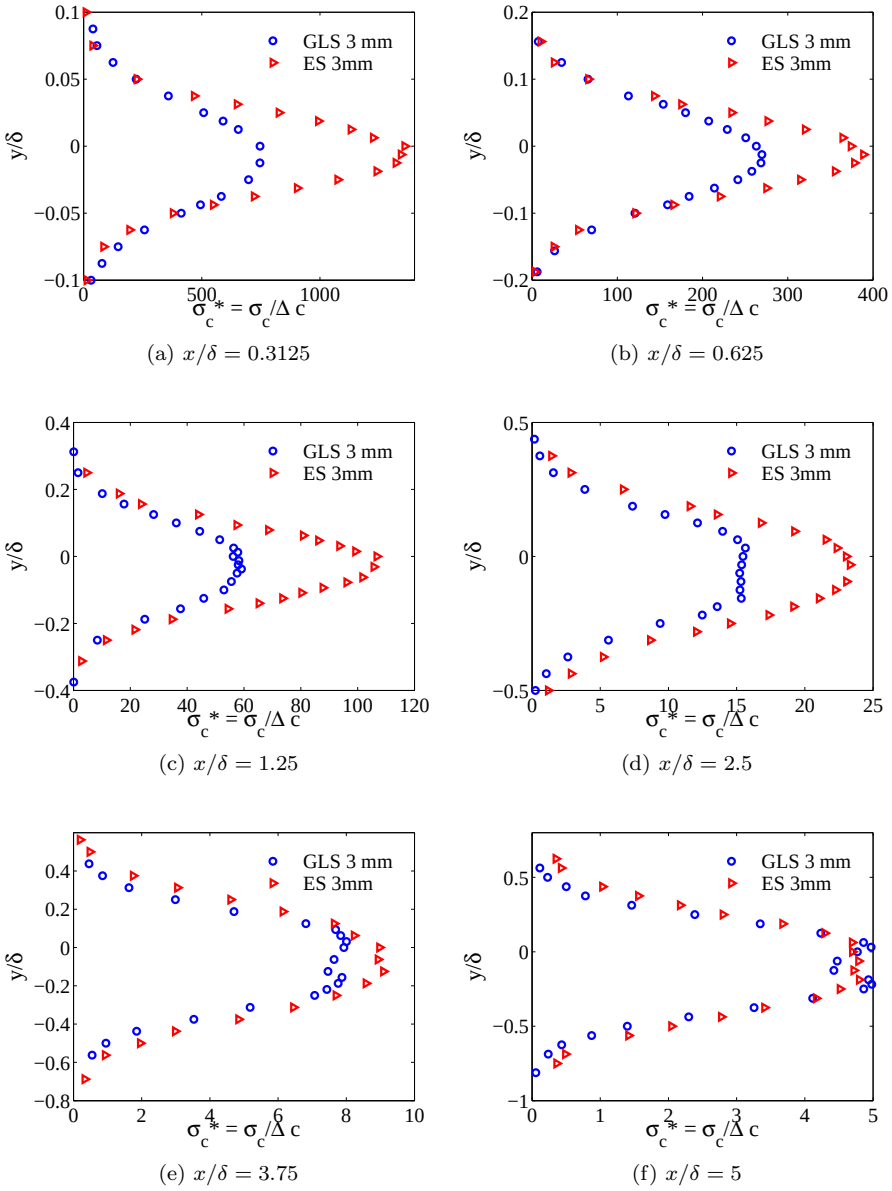

(a) $x/\delta = 0.3125$ (b) $x/\delta = 0.625$

(c) $x/\delta = 1.25$ (d) $x/\delta = 2.5$

(e) $x/\delta = 3.75$ (f) $x/\delta = 5$

Figure 3.20: Transversal profiles of non-dimensional concentration standard deviation for the ground level source with diameter 3 mm, at various distances downwind. Profiles were measured at the source heigth, $z_s/\delta = 0.0625$. A comparison is made with the elevated source having the same diameter.

source they are shown in Figure 3.20. Vertical profiles are reported in the Annexe 7.1. A strong dependence on the source size is visible near the source, confirming that the small source generates the highest fluctuations. The gap mitigates moving downwind, up to the last two stations where the profiles collapse.

Source elevation also has a strong influence, as shown in Figure 3.20 where ES and GLS are compared. The ES emission results in higher concentration standard deviation, only at the latest station the profiles collapse. A difference is observed also in the profiles shape. While the σ_c^* from ES emission always have a Gaussian like form, the profiles for GLS depart from this is the far field and exhibit off-centreline maxima. These off-centreline peaks are due to a reduced meandering motion in the plume centre-line in the far field. This phenomenon was also noticed by Yee and Wilson (2000), who argue that still the exact quantitative conditions required for the emergence of off-centreline peaks have not been elucidated.

3.5.5 Higher concentration moments

The non-dimensional third and fourth concentration moments are calculated as:

$$m_{3c}^* = \left[\frac{1}{N} \sum_{j=1}^{N} (c_j^* - C^*)^3 \right]^{1/3} \tag{3.40}$$

$$m_{4c}^* = \left[\frac{1}{N} \sum_{j=1}^{N} (c_j^* - C^*)^4 \right]^{1/4} \tag{3.41}$$

where c^* is non-dimensional instantaneous concentration, C^* is the non-dimensional mean of the time-series and N is the number of samples in the time-series.

Transversal profiles of the third and fourth moments of concentration downwind of the source are presented in Figure 3.21 for the elevated sources, while for the ground level source they are shown in Figure 3.22. Vertical profiles are reported in the Annexe 7.1. Third and fourth moments have a similar behaviour for what concerns the influence of source size and source elevation. The first is investigated by means of measurements on the ES, where a strong source-size dependence is observed in the near field. As expected, the small source generates higher moments. It is remarkable how a tiny difference in the source size, whose diameter was varied by a factor of 2 (from 3 to 6 mm), is reflected in significant variations of higher order moments of the concentration fluctuations. These appear to be more and more pronounced as the moment are increased and persist up to a distance of about $3m$, that is about 1000 times the source diameter. Moving downwind the difference in concentration fluctuations diminishes (see Figure 3.18, where is shown the downwind evolution of the intensity of concentration fluctuations) and consequently the profiles gradually approach one to the other and finally collapse at the latest two stations.

The source elevation is even more determinant in the shape of the moments profiles. While profiles from the ES emission have a Gaussian like shape, in the GLS case the shape changes soon downwind. At $x/\delta = 1.25$ a constant zone is observed at the centre of the profile and afterwards the phenomenon of

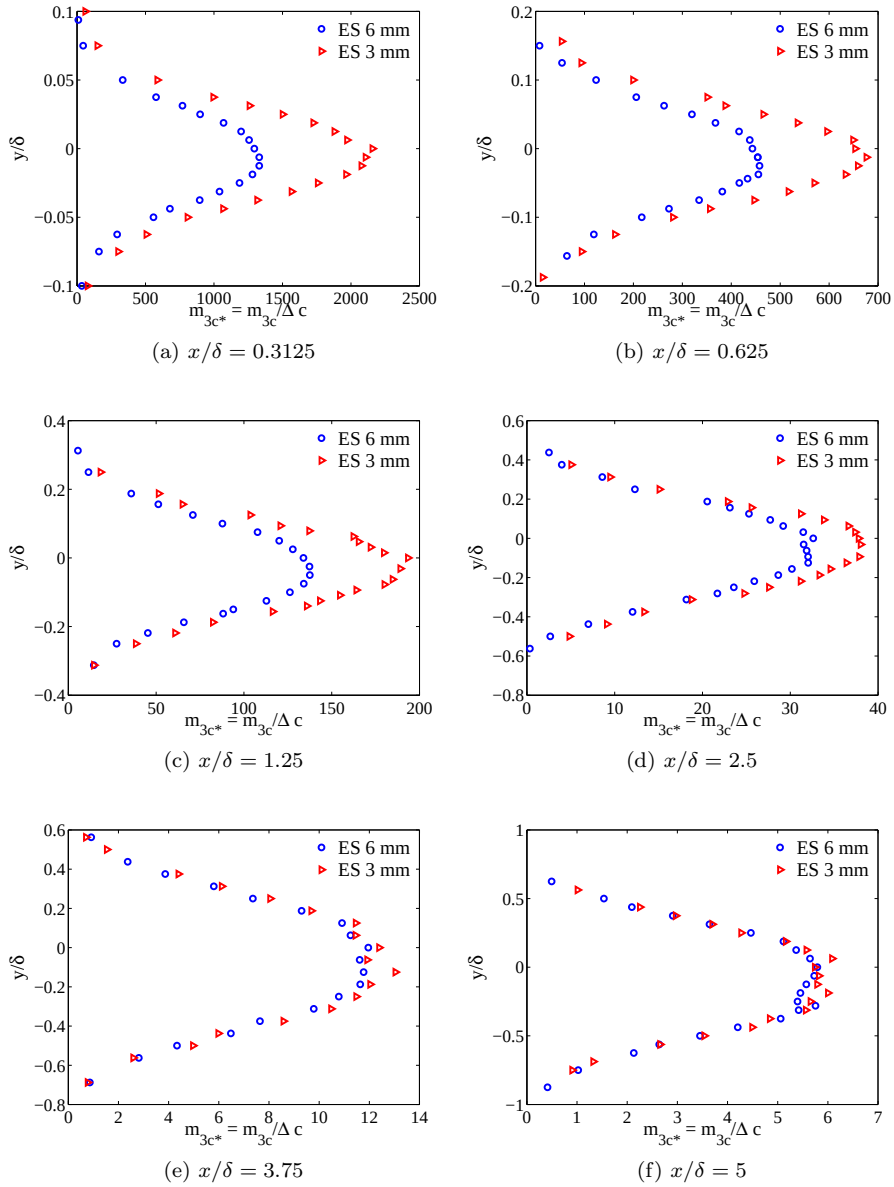

(a) $x/\delta = 0.3125$ (b) $x/\delta = 0.625$

(c) $x/\delta = 1.25$ (d) $x/\delta = 2.5$

(e) $x/\delta = 3.75$ (f) $x/\delta = 5$

Figure 3.21: Transversal profiles of non-dimensional third moment of concentration. Elevated sources at various distances downwind. Profiles were measured at the source heigth, $z_s/\delta = 0.19$. Blue circles: source diameter 6 mm; red triangles: source diameter 3 mm.

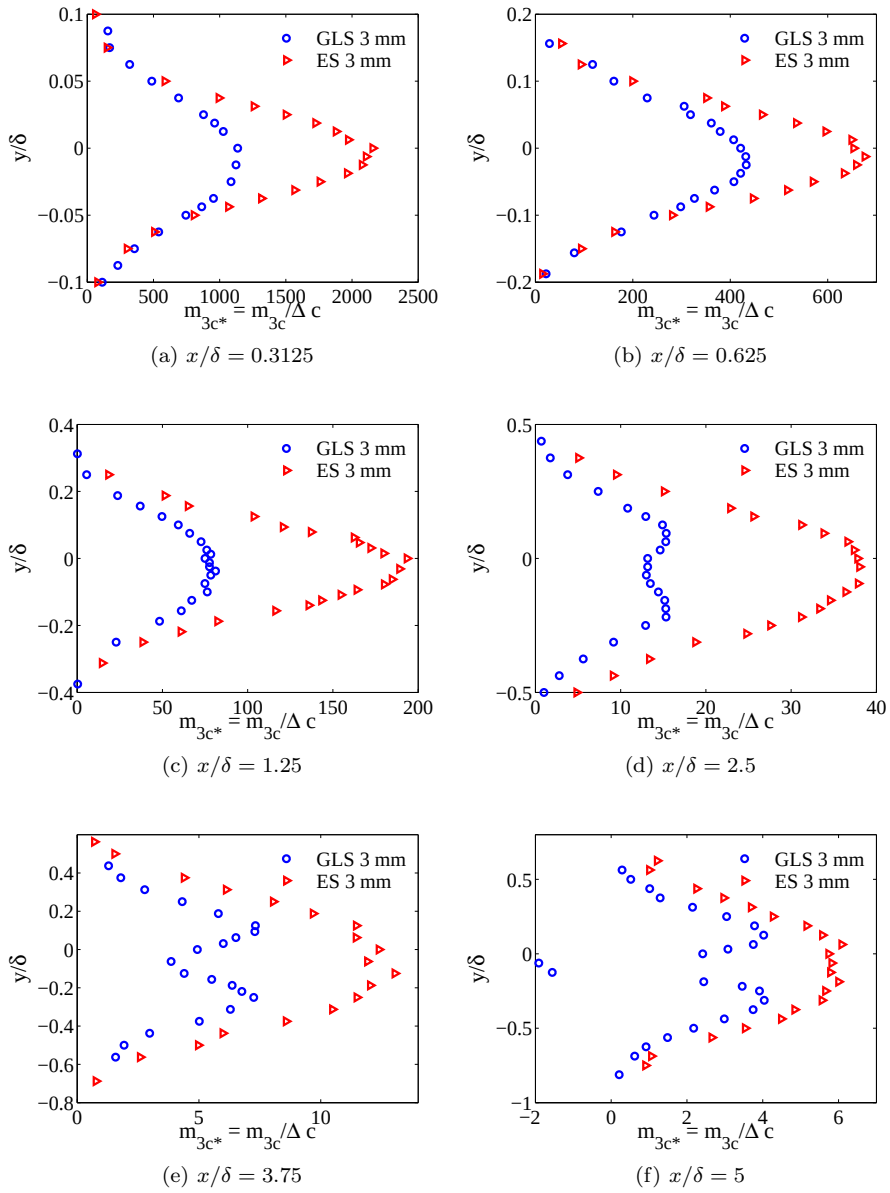

(a) $x/\delta = 0.3125$ (b) $x/\delta = 0.625$

(c) $x/\delta = 1.25$ (d) $x/\delta = 2.5$

(e) $x/\delta = 3.75$ (f) $x/\delta = 5$

Figure 3.22: Transversal profiles of non-dimensional third moment of concentration for the ground level source with diameter 3 mm, at various distances downwind. Profiles were measured at the source heigth, $z_s/\delta = 0.0625$. A comparison is made with the elevated source having the same diameter.

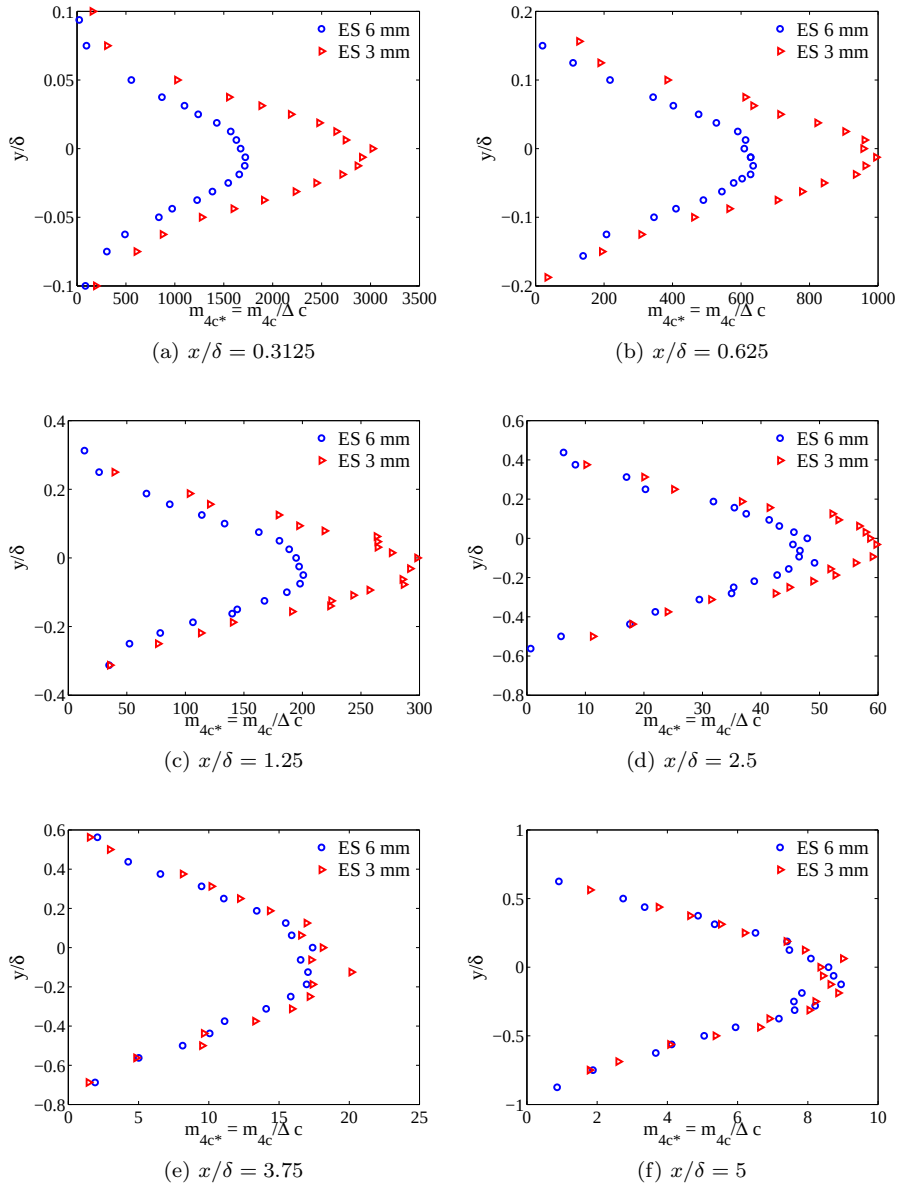

(a) $x/\delta = 0.3125$ (b) $x/\delta = 0.625$

(c) $x/\delta = 1.25$ (d) $x/\delta = 2.5$

(e) $x/\delta = 3.75$ (f) $x/\delta = 5$

Figure 3.23: Transversal profiles of non-dimensional fourt moment of concentration. Elevated sources at various distances downwind. Profiles were measured at the source heigth, $z_s/\delta = 0.19$. Blue circles: source diameter 6 mm; red triangles: source diameter 3 mm.

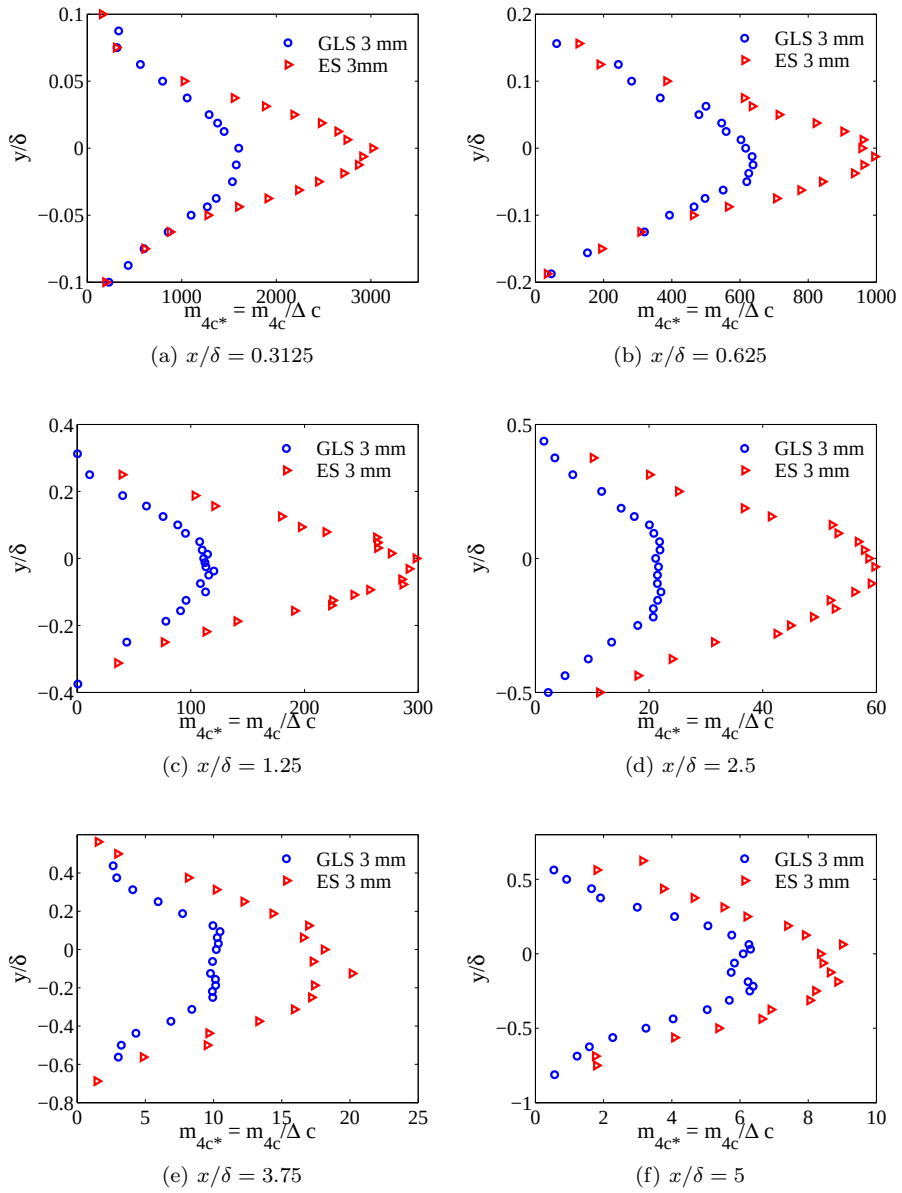

(a) $x/\delta = 0.3125$ (b) $x/\delta = 0.625$

(c) $x/\delta = 1.25$ (d) $x/\delta = 2.5$

(e) $x/\delta = 3.75$ (f) $x/\delta = 5$

Figure 3.24: Transversal profiles of non-dimensional fourt moment of concentration for the ground level source with diameter 3 mm, at various distances downwind. Profiles were measured at the source heigth, $z_s/\delta = 0.0625$. A comparison is made with the elevated source having the same diameter.

off-centreline peaks appears, starting from $x/\delta = 2.5$. At the latest station, m^*_{3c} is negative on the plume centre-line. The third moment is the most affected by off-centreline peaks. However, their apparition is evidents also on m^*_{4c}. Finally we can note how the graphs for m^*_{4c} show generally more scatter in the profiles compared to those of lower order moments. This is due to the increased experimental error affecting our data as the order of the moments of the concentration PDF increases, mostly due to the undesired spikes registered in the signals caused by aerosol sampling.

It was shown in Paragraph 3.5.1 that a one-parameter gamma distribution well predicts the probability density function downwind elevated and ground level sources. We now verify whether the third and fourth moments of the gamma distribution are in agreement with our measurements. Provided the parameter k, that specifies the gamma distribution and is defined as $k = C^2/\sigma_c^2$, the moments $m^*_{3c\Gamma}$ and $m^*_{4c\Gamma}$ are calculated as:

$$m^*_{3c\Gamma} = \left(\frac{2}{\sqrt{k}}\right)^{1/3} \sigma_c^{2*} \tag{3.42}$$

$$m^*_{4c\Gamma} = \left(\frac{6}{k} + 3\right)^{1/4} \sigma_c^{2*}. \tag{3.43}$$

In the near field ($x/\delta = 0.3125$), the moments of the gamma distribution reproduce experimental data with a good precision. The differences between source dimensions and elevation are respected and curves superpose for the three source types. In the far field ($x/\delta = 5$), a little scatter is observed between the gamma distribution and experiments. At the plume centreline, for the ES case, $m^*_{3c\Gamma}$ and $m^*_{4c\Gamma}$ under-estimate the experiments, especially fourth moments. As well as measured third and fourth moments, $m^*_{3c\Gamma}$ and $m^*_{4c\Gamma}$ are not affected by the source size, but are sensible to the source elevation. It is therefore possible to distinguish between moments due to ground level and elevated emissions. For the GLS case, there is a general overestimation of experimental data in the far field, that is particularly visible in the third moment. The shape of $m^*_{3c\Gamma}$ is close to the experimental one, and we observe the existence of off-centreline peaks. These peaks are also present in the GLS fourth moment, were the $m^*_{4c\Gamma}$ overestimate experimental data. Also for the elevated sources, $m^*_{3c\Gamma}$ and $m^*_{4c\Gamma}$ present small off-centreline peaks. These peaks however are not clearly distinguishable in experimental data.

3.5.6 Relationships between higher moments of concentration

It was demonstrated by Chatwin and Sullivan (1990) that the same simple relationship between the mean concentration C and the mean-square fluctuation σ_c of a dispersing scalar exists for a wide range of turbulent shear flows, in statistically self-similar and steady conditions. This relationship was at first postulated for the dispersion of a scalar with concentration c in a turbulent shear flow, in the hypothetical situation when there is no molecular diffusion. So that in the convective diffusion equation (3.4), the coefficient of molecular diffusivity D is equal to zero. This is a strictly theoretical flow, where concentration can assume only two values: the release concentration c_s and 0. Any dispersion

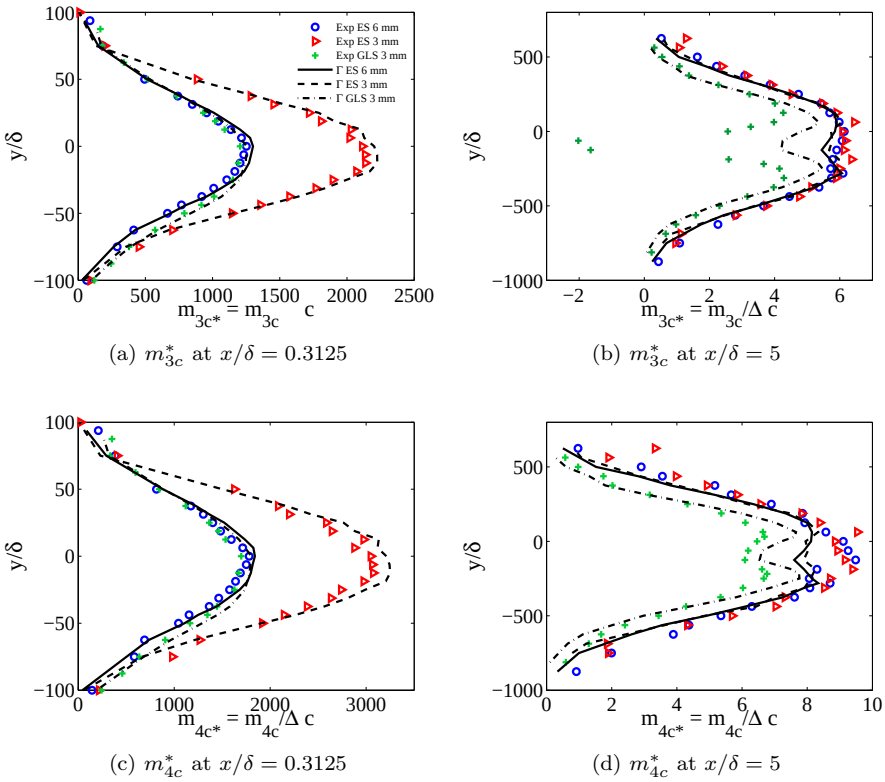

(a) m^*_{3c} at $x/\delta = 0.3125$

(b) m^*_{3c} at $x/\delta = 5$

(c) m^*_{4c} at $x/\delta = 0.3125$

(d) m^*_{4c} at $x/\delta = 5$

Figure 3.25: Experimental profiles of non-dimensional third and fourth moments in the transversal direction for the three sources (ES 6 mm, ES 3 mm, GLS), compared to the moments of the gamma distribution from Equations 3.43.

process would be characterized by a PDF of the form

$$p(c; x_j, t) = \pi(x_j, t)\delta(c - c_s) + (1 - \pi(x_j, t))\delta(c) \tag{3.44}$$

where π is the probability of finding a marked fluid and $\delta_D(.)$ is the Dirac delta function. Such a system can be described completely by its first two moments

$$C = \pi c_s \tag{3.45}$$

$$\sigma_c^2 = \pi c_s^2(1 - \pi). \tag{3.46}$$

With physical arguments, Chatwin and Sullivan (1990) extended Equation 3.46 to the real case, for a molecular diffusivity $D > 0$. Molecular diffusion acts in two fundamental ways. The maximum concentration at a certain distance downwind is less than the release concentration, and it diminishes by a factor that increases with the distance. The concentration standard deviation is dissipated according to the reduction of the maximum concentration and according to the statistical properties of the velocity field. Two empirical parameters were introduced in 3.46 to account for the effects of molecular diffusion, and the second moment was written as:

$$\sigma_c = B\ C(A\ C_{max} - C) \tag{3.47}$$

where $C_{max}(x)$ denotes the maximum value of the mean concentration C at each cross-section, and corresponds to the centerline mean concentration. A and B are positive parameters, having a constant value. A considers that the evolution of the contaminant distribution is controlled by the large eddies of the velocity field, while B is essentially a measure of the amount of dissipation accomplished by molecular diffusion.

Chatwin and Sullivan (1990) theory was extended for third and fourth moment of a diffusing scalar by Mole and Clarke (1995). They demonstrate that there exists a quadratic relationship between the skewness (Sk) and the kurtosis (Ku) obtained from continuous, elevated sources of scalar contaminant released into both convective and stable atmospheric boundary layers.

$$Ku = aSk^2 + b \tag{3.48}$$

where skewness and kurtosis are defined as follows

$$Sk = \frac{m_{3c}^*}{\sigma_c^{*3}}\ ;\ Ku = \frac{m_{4c}^*}{\sigma_c^{*4}} \tag{3.49}$$

and a and b are empirically fitted constants that depend on the flow.

They noted that the relationship $Ku = Sk^2 + 1$ can be used as a check of whether the model is consistent with the data, as it represents the lower bound of the general relationship. In fact, it is true for all probability distributions that $Ku \geq Sk^2 + 1$. It is likely that all graphs of skewness against kurtosis will lie on a parabola above this lower bound.

The existence of a relation between skewness and kurtosis is a potentially useful information in regard to modelling the probability density function of a diffusing scalar. With a knowledge of all moments, the PDF can be fully reconstructed. The first three or four moments are enough to capture the bulk characteristics of the PDF (Chatwin and Sullivan, 1990), however higher order

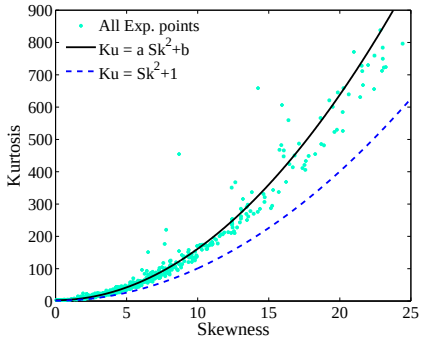

(a) All experimental points: $a = 1.589$, $b = 2.509$

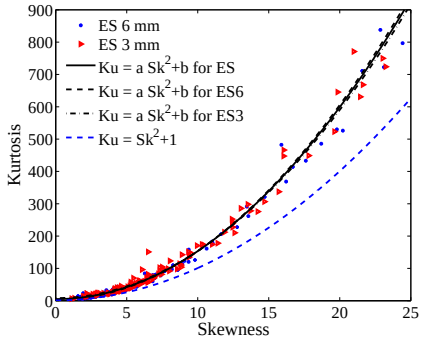

(b) ES 6mm: $a = 1.507$, $b = 2.791$, ES 3mm: $a = 1.456$, $b = 8.074$, All ES: $a = 1.485$, $b = 4.975$

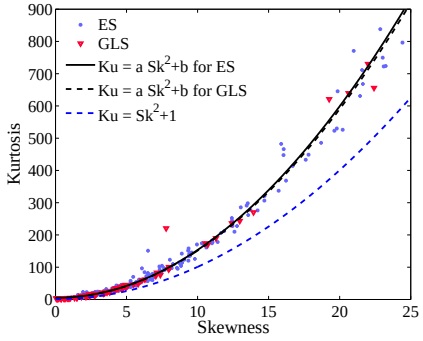

(c) GLS: $a = 1.463$, $b = 5.132$, All ES: $a = 1.485$, $b = 4.975$

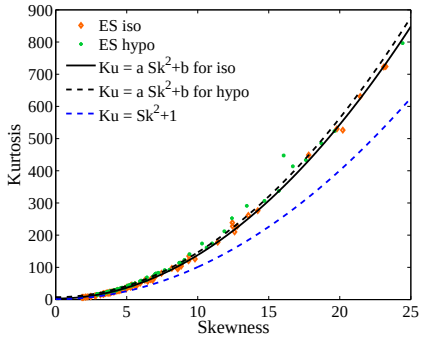

(d) ES iso: $a = 1.352$, $b = 2.989$, ES hypo: $a = 1.391$, $b = 7.375$

Figure 3.26: Kurtosis Ku against Skewness Sk. Equation $Ku = aSk^2 + b$ is fitted to experimental measurements using a least squares best fit. Dashed blue line is the theoretical lower bound, $Ku = Sk^2 + 1$.

moments are required to retrieve more subtle features. If one intends to model the PDF by inverting a limited number of moments, the task is reduced when there is a functional relationship between the standardized third and fourth moments.

From one flow to another, there appears to be a non-negligible variability in the a and b coefficients. Using field data from a continuous elevated source in both convective and stratified conditions in the atmospheric boundary layer, Mole and Clarke (1995) determined the fitted constants to be $a = 1.31$ and $b = 0.77$. Lewis et al. (1997) used field measurements in stability conditions and continuous releases to determine the fitted constants to be $a = 4/3$ and $b = 3$. Schopflocher and Sullivan (2005) attempted to predict how a and b vary in space and time, using wind tunnel experiments where the source of contaminant consisted in a heated wire producing a line source of heat. They found that the fitting parameters generally increase while proceeding downstream. Parameter a is about 1.14 near the source and than levels off at 1.43. Parameter b have less variation and ranges from 1.82 to 2.22.

We attempted to predict whether the source dimension, elevation and emission velocity have some influence on the relation between skewness and kurtosis. To estimate a and b, we fitted Equation 3.48 on our experimental measurements with least squares best fit. All experimental points where the signal-to-noise ratio was not satisfactory, especially those at the plume borders, were excluded from the analysis. From our data, we are not able to clearly identify the influence of the source size on the parameters a and b (Figure 3.26b), as the fits superpose for the cases ES 3 mm, ES 6 mm and ES (obtained with a fit on all elevated source measurements, without size diversification). The regression of Equation 3.48 on GLS and ES measurements returns close values of the couple a and b, as shown in Figure 3.26c. A small difference is observed between the fitting on isokinetic and hypokinetic ES measurements in the near field (Figure 3.26d), however no significant pattern can be deduced from the data. In conclusion, a ranges from 1.35 to 1.59 and b, which has more variability, ranges from 2.5 to 8. If all experimental points are best-fitted at once, without any diversification, a is equal to 1.58 and b is 2.51 (Figure 3.26a).

3.5.7 Influence of the source conditions

In most of the studies on passive scalar dispersion in a TBL, it is implicitly assumed that the particles emitted at the source instantaneously take the statistics of the external velocity field, so that there is no difference between Lagrangian statistics of the fluid particles injected at the source and those in the ambient fluid passing close to it. In order to reproduce experimentally this condition, two precautions are taken to minimise the effects of the source in the dispersion process. First of all, the source has to be chosen so that its interaction with the velocity field, i.e. its wake, is minimised. Secondly, the tracer should be emitted horizontally and in isokinetic conditions, so that the outlet velocity should equal the average velocity of the flow over its height.

It is generally assumed that with isokinetic conditions, the mean concentration field is not influenced by the source dimensions and that profiles from different source sizes collapse, for both ground level and elevated sources. This was not the case for our elevated source measurements. As shown in Figure 3.8, at the first station downwind ($x/\delta = 0.3125$), the mean concentration from the

6mm source was 30% greater than the 3mm one. This disparity reduces moving downwind and disappears for $x/\delta = 2.5$.

The ideal source conditions implies zero momentum deficit, zero density deficit and uniform velocity distribution. Departures from ideal conditions were studied by Fackrell and Robins (1982a), and were analysed in terms of difference between the real source diameter and a source flux diameter. They estimated a 10% difference between real and source flux diameter for profiles measured at distances starting from $x/\delta = 0.83$.

In our case, we estimated that the emission has no density deficit because the emitted gas is considerably diluted (from 0.01 % to 3.75% of ethane in air) and has the same temperature of ambient air. To diminish the walls friction, our sources were made by a metallic tube smoothed on the inside. Nevertheless, the condition of uniform velocity at the source is difficult to attain.

Since most of the concentration fluctuations are produced very close to the source (Paragraph 3.5.4), the investigation of the effect of the emission condition on the concentration field is a problem that deserves to be deeply analysed. In order to clarify this feature we focus here on the modification induced by the presence of the source on the velocity field and on the influence of the emission conditions on the concentration statistics by comparing isokinetic and hypokinetic emissions (in hypokinetic conditions the outlet velocity is slower than the velocity field at the same height: $u_s = 0.03\overline{u}_s$, being u_s the source outlet velocity and $\overline{u}_s$ the field mean velocity at the stack height).

We begin by analysing the perturbation of the velocity field induced by the physical presence of the source. To this purpose we measured the extension of the source wake depending on the gas emission conditions. A different analysis was carried out for each of the two elevated sources. For the small 3 mm source, our purpose was to understand how far the velocity field was altered by the presence of the source. Therefore, we measured, with hot wire anemometry, streamwise and vertical velocity profiles at the source elevation in two cases: with and without the source. No flow was emitted from the source. Profiles of the mean streamwise velocity $\overline{u}/U_\infty$ are shown in Figure 3.27. The source generates a region of velocity deficit that is likely to have non negligible consequences on the tracer dispersion. The logarithmic profile in the proximity of the source (at $x/\delta = 0.025$, corresponding to 6 times the source diameter) is highly perturbed. A velocity deficit region is clearly distinguishable, where $\overline{u}$ reaches a value of - 20% compared to the undisturbed velocity at the same height. At a distance $x/\delta = 0.4$ - corresponding to more than 100 times the source diameter - the flow is still slower than in undisturbed conditions.

A second analysis was carried out to highlight the influence of the gas emission velocity. We chose to use the big 6 mm source because, as already pointed out, this is the one that mostly affects the outlet conditions. We measured streamwise and vertical profiles of mean velocity in two cases: at first without any emission so that $u_s = 0$, and on a second time with an outlet velocity corresponding to hypokinetic conditions (that is to say that the ratio $u_s/\overline{u}_s = 1$). Measurements were carried out by means of a hot wire anemometer with a simple one-wire probe. The streamwise profile of $\overline{u}/U_\infty$ is shown in Figure 3.28 and vertical profiles are reported in Figure 3.29, for four distances from the source.

The 6 mm source generates a velocity defect region that extends for a long fetch downwind. Close to the source, at $x/\delta = 0.045$ (corresponding to 6 times the source diameter d) the mean velocity $\overline{u}$ is diminished of about 60% with

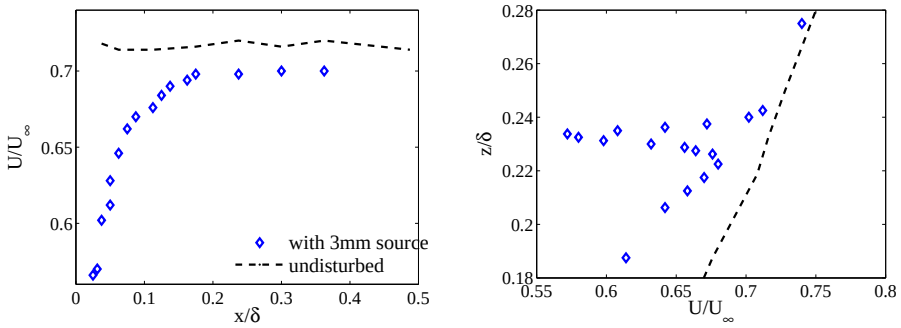

(a) Streamwise profile on the source centreline (b) Vertical profile at $x/\delta = 0.025$

Figure 3.27: Study of the influence of the source on the mean velocity field, source 3 mm. Comparison of streamwise and vertical profiles of mean velocity measured at the elevation of the emission point, in the presence of the source (not emitting) and in the undisturbed field without the source. The source is placed at $x/\delta = 0$.

respect to the undisturbed field. Moving from the source, the influence of the source slowly fades until the logarithmic profiles recovers its original shape, at $x/\delta = 3.75$, corresponding to 500 times the source diameter. The 6 mm source modifies substantially the velocity field and its influence on $\overline{u}$ is stronger and more persistent in time, compared to the 3 mm.

When the source is emitting, a clearly detectable jet effect appears. This effect can be observed on the profiles measured at $x/\delta = 0.045$ and $x/\delta = 0.225$, where the mean velocity $\overline{u}_s$ on the source centreline is higher than the flow due to the jet effect, while is lower on the source borders due to the velocity defect generated by the wake. At $x/\delta = 0.45$ (60 times d), the jet effect is almost disappears but the source wake is still clearly visible. As shown by the streamwise profile, the effect of the emission velocity persists up to about 130 times d ($x/\delta = 1$).

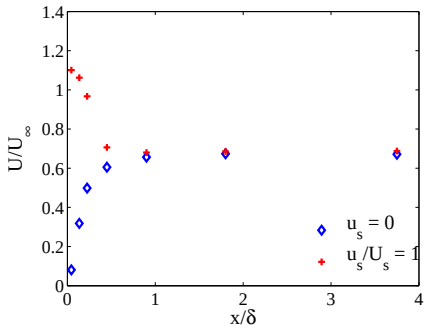

Figure 3.28: Streamwise profile of mean velocity at the source elevation, source 6 mm. Comparison between the case with no emission ($u_s = 0$) and the case of isokinetic emission ($u_s/\overline{u}_s = 1$). The source is placed at $x/\delta = 0$.

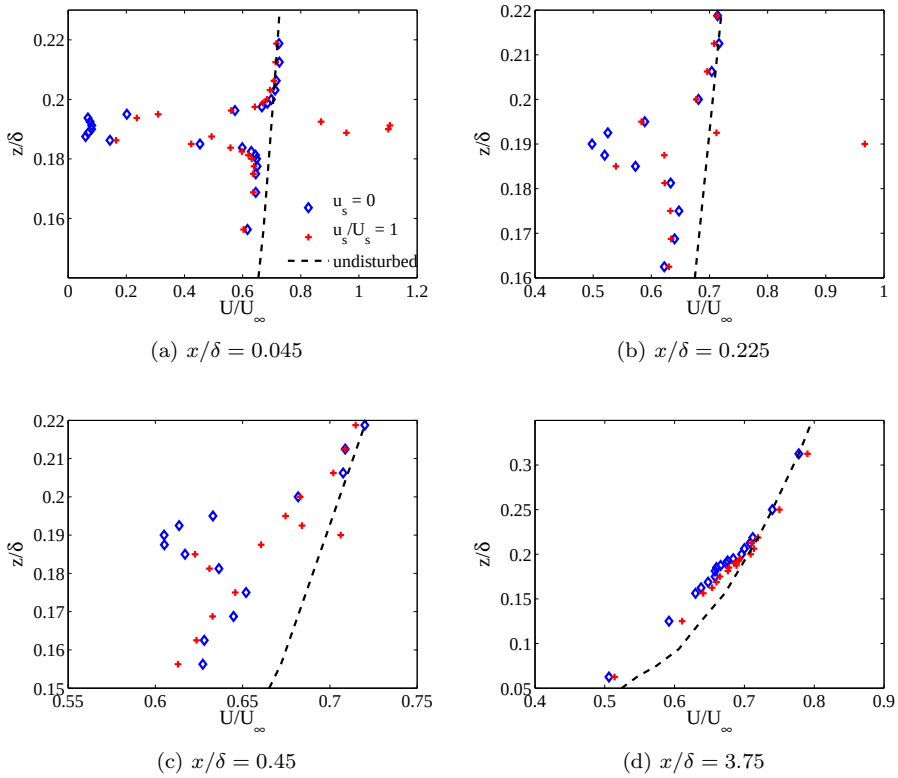

(a) $x/\delta = 0.045$ (b) $x/\delta = 0.225$

(c) $x/\delta = 0.45$ (d) $x/\delta = 3.75$

Figure 3.29: Study of the influence of the emission velocity on the mean velocity field, source 6 mm. Comparison between the case with no emission ($u_s = 0$) and the case of isokinetic emission ($u_s/\overline{u}_s = 1$). The source is placed at $x/\delta = 0$.

We now focus on the concentration field, by comparing the isokinetic conditions $u_s/\overline{u}_s = 1$ and the hypokinetic conditions $u_s/\overline{u}_s = 0.03$, that approximate the condition $u_s/\overline{u}_s \to 0$. Concentration profiles were measured close to the source, at the stations $x/\delta = 0.3125$ and $x/\delta = 0.625$. In Figure 3.30 the measured hypokinetic transversal profiles of mean concentration are compared to the respective isokinetics.

For both sources, the hypokinetic profiles have smaller concentration than the isokinetics. The difference between mean concentration profiles with different source diameter is considerably reduced at the first station in the hypokinetic case, while at the second station downwind hypokinetic profiles collapse. While profiles from the small 3mm source only showed a small reduction passing from iso to hypo conditions, major changes occurred in profiles from the 6mm source, showing that the influence of the emission velocity increases with the source dimensions.

The influence of the emission velocity on the moments of concentrations is showed in Figure 3.31, where r.m.s, third and fourth moments are compared. The standard deviation confirms what was observed for the mean. Firstly, the impact of the momentum deficit is more important close to the source. Secondly, the bigger is the source size, the higher is the influence of the emission velocity.

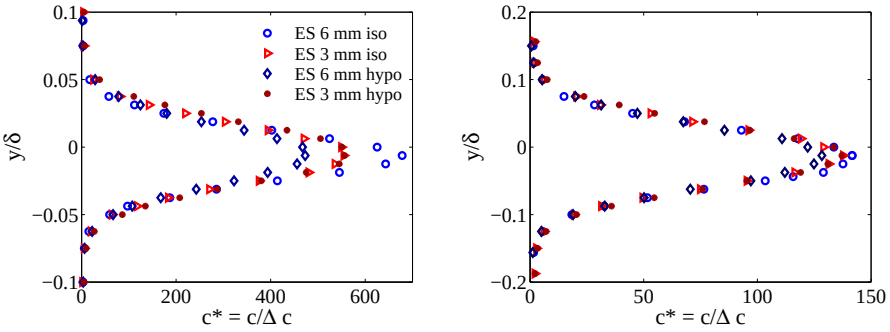

(a) $x/\delta = 0.3125$ (b) $x/\delta = 0.625$

Figure 3.30: Transversal profiles of non-dimensional mean concentration for the elevated sources, comparison between isokinetic and hypokinetic conditions.

While the r.m.s. of the 3 mm source diminishes slightly in the hypokinetic case, the 6 mm one shows a strong reduction. The influence of the outlet velocity is weaker on higher moments (m^*_{3c} and m^*_{4c}), whose profiles are still different in the iso- and hypokinetic emissions but the discrepancies are mitigated.

It worth noting that it is not possible to distinguish which of the two conditions (isokinetic or hypokinetic) induce a concentration field that is closer to the one generated by an ideal source without any wake effect and with particle statistics identical to that of the surrounding flow. To clarify this point it should be necessary to simulate both conditions with a CFD code or with a Lagrangian stochastic model.

3.5.8 Intermittency factor

To further inquire the influence of the source condition, we have focused on the intermittency of the concentration signals. The intermittency factor γ_c is defined as the percentage of time for which the plume is experienced at a given point. It can be calculated from measured concentration probability distributions, P(c), since:

$$\gamma_c = \int_0^1 P(c)\, dc. \tag{3.50}$$

If $\Gamma_c(\mathbf{x}, t)$ is a random variable describing the concentration at position $\mathbf{x}$ and time t, the intermittency factor can also be calculated as:

$$\gamma_c(\mathbf{x}, t) = prob(\Gamma_c(\mathbf{x}, t) > 0). \tag{3.51}$$

A reliable determination of the intermittency depends on the fine scale structure of turbulence, whose temporal and spatial resolution is invariably accompanied by random noise. Due to the noise, zero concentrations can not be measured and a small threshold value of concentration (Γ_t) is fixed, under which we suppose that the plume is not experienced by the probe. γ_c is obtained with the following equation:

$$\gamma_c(\mathbf{x}, t) = prob(\Gamma_c(\mathbf{x}, t) > \Gamma_t). \tag{3.52}$$

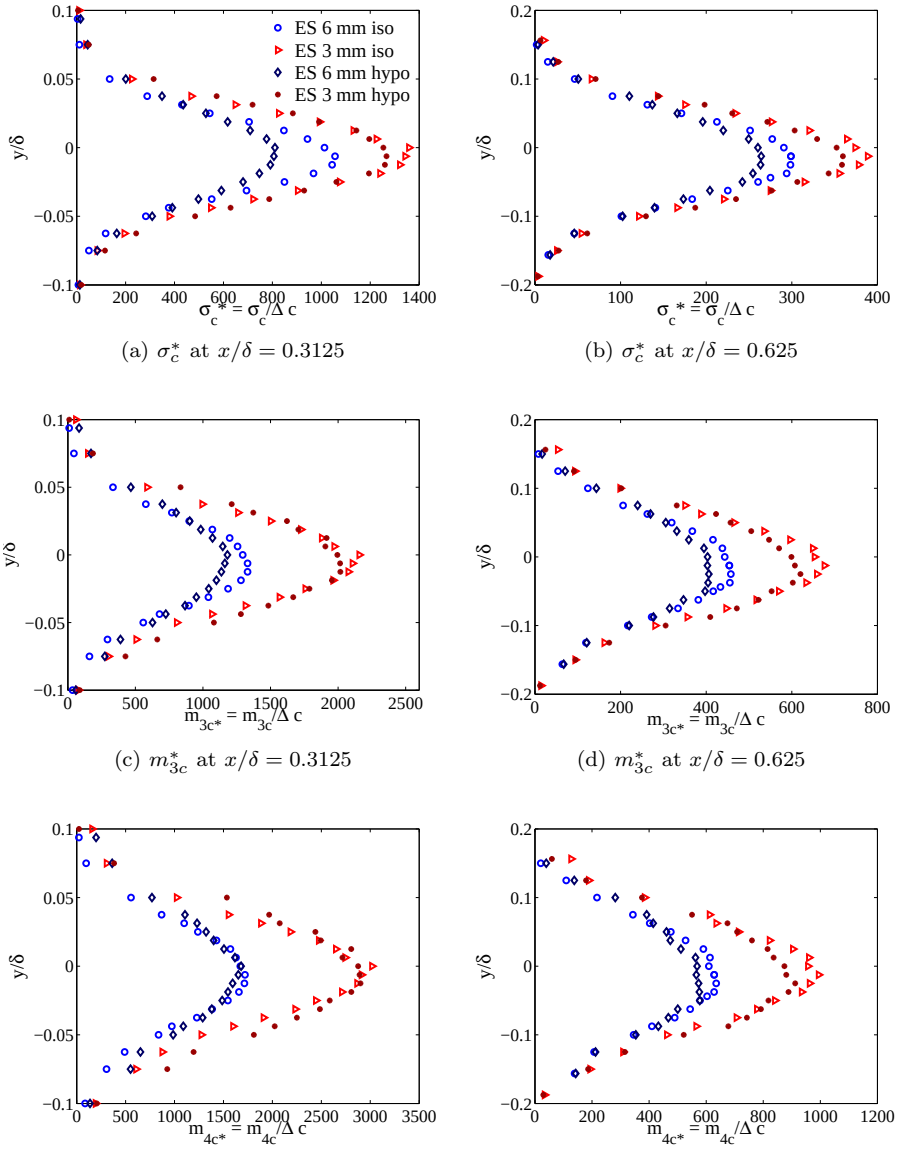

(a) σ_c^* at $x/\delta = 0.3125$

(b) σ_c^* at $x/\delta = 0.625$

(c) m_{3c}^* at $x/\delta = 0.3125$

(d) m_{3c}^* at $x/\delta = 0.625$

(e) m_{4c}^* at $x/\delta = 0.3125$

(f) m_{4c}^* at $x/\delta = 0.625$

Figure 3.31: Transversal profiles of non-dimensional r.m.s, third moment and fourth moment for the elevated sources. A comparison is made between isokinetic and hypokinetic conditions.

The choice of the threshold inevitably involves some arbitrariness, and the calculated values of γ_c are strongly dependent on it. This lead to the practical conclusion that a quantitative interpretation of the published data is not possible unless they are accompanied by the corresponding value of Γ_t (Chatwin and Sullivan, 1989). The variation of the intermittency factor with Γ_t was investigated at three distances downwind (Figure 3.32a). γ_c decreases with increasing the threshold. The trend is different in the three cases: the sharpest fall is experienced close to the source, while in the far field the decrease is more gradual. As the need of choosing a threshold is due to the measurement errors inevitably affecting the zero concentration values, we believe that Γ_t should be a small constant value, not depending on the downwind distance. For all stations, Γ_t was fixed equal to 1, in non-dimensional form. This threshold allows an efficient separation between the moments when the plume is experienced by the probe and the moments of zero concentration.

Profiles of intermittency factor are calculated for the elevated sources (diameters 3 mm and 6 mm) and for the ground level source (Figure 3.32b). Intermittency decreases with downwind distance for all source configurations. Elevated sources behave in a very similar way and no influence of the source size can be distinguished, apart for the first two stations where the smaller source is slightly more intermittent. At the furthest downstream position intermittency tends to unity, meaning that the plume is more mixed. The ground level emission is less intermittent than the elevated ones and reaches unity at $x/\delta = 1.25$.

The gas emission velocity at the source have an important influence on the intermittency. In Figure 3.32c is shown a comparison between γ_c calculated for the isokinetic and hypokinetic emissions, at the first two stations downwind. In the isokinetic case, γ_c is closer to unity, meaning that the plume is less intermittent. If the tracer is released hypokinetically, no jet effect is produced and the plume is immediately transported by the velocity field, resulting in a smaller intermittency factor. As it was already observed in Paragraph 3.5.7, the bigger is the source, the bigger is the influence of the emission velocity on the concentration field.

It can be noted that, independently on the source configuration, the intermittency approaches unity when the plumes reach the ground level and are efficiently mixed by the small scale surface generated turbulence, that acts by suppressing concentration fluctuations.

3.5.9 Spectra of concentration fluctuations

In order to analyse how source size and height affect the distribution of the variance of concentration over different length scales we turn to concentration spectra.

Spectra of concentration fluctuations measured on the center line at various distances from the source are given in Figure 3.33, where spectra from elevated sources and from the ground level source are compared. $E(k)$ is the one-dimensional wavenumber spectrum, with wavenumber $k = 2\pi f/\overline{u}$, $\overline{u}$ being the local flow speed. The $-5/3$ region corresponding to the inertial subrange is present, even if with a limited extension, especially in the near field.

The influence of the source size is clearly visible in the near field. Spectra from the small elevated source (diameter = 3 mm) result greater than the ones obtained for the big elevated source (diameter = 6 mm). This difference can

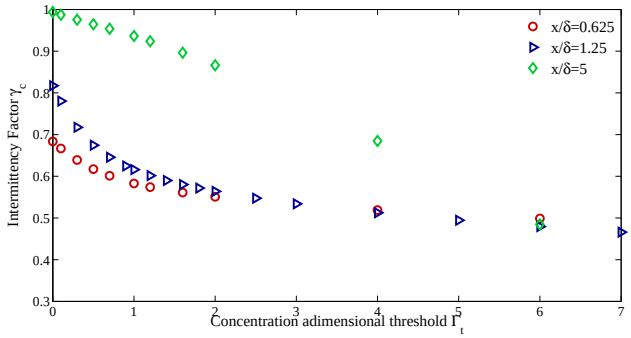

(a) Variation of the intermittency factor γ_c with the concentration threshold Γ_t used in the calculation, for three stations downwind. The threshold is non-dimensional, its value in kg/m^3 can be obtained as $\Gamma_t \Delta_c$.

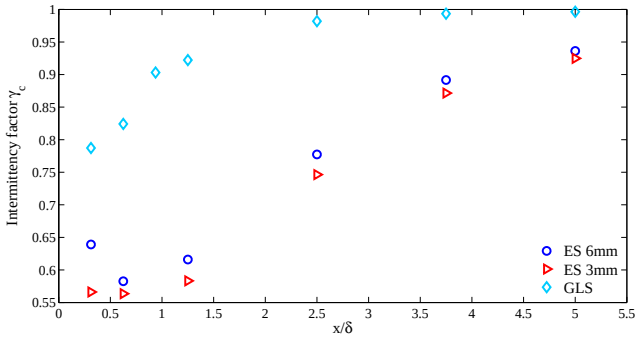

(b) Intermittency profile downwind the source for the three source configurations: elevated source 6mm, elevated source 3mm, ground level source.

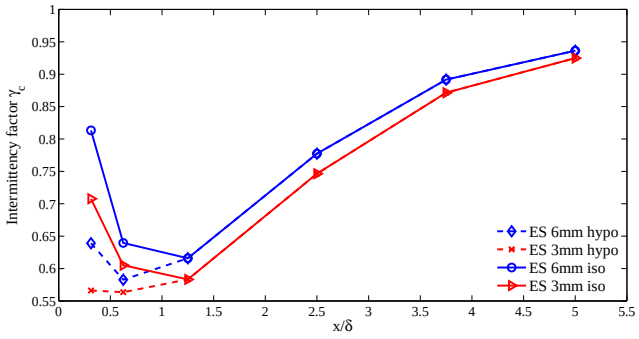

(c) Influence of the outlet velocity at the source.

Figure 3.32: Intermittency factor

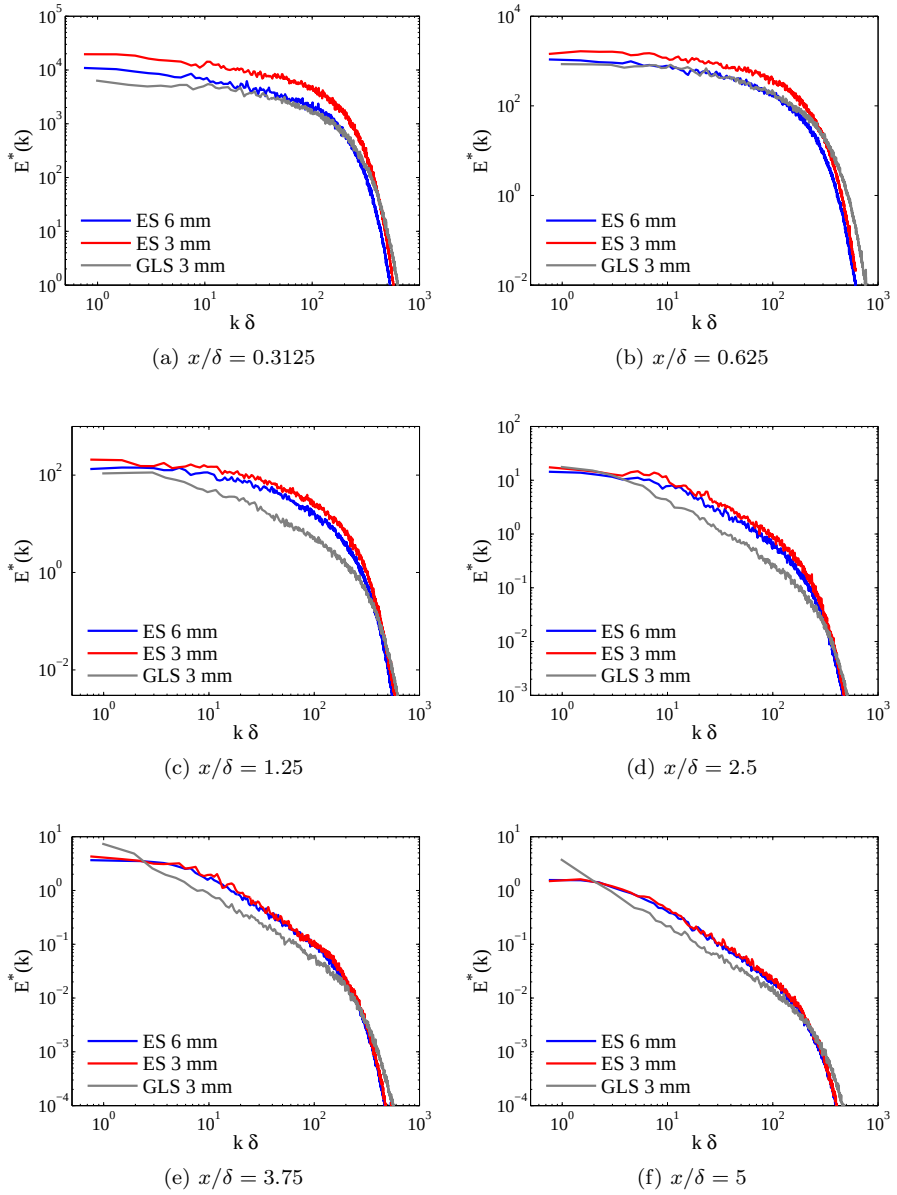

(a) $x/\delta = 0.3125$ (b) $x/\delta = 0.625$

(c) $x/\delta = 1.25$ (d) $x/\delta = 2.5$

(e) $x/\delta = 3.75$ (f) $x/\delta = 5$

Figure 3.33: Spectra of concentration fluctuations on the plume center line, at a growing distance from the source. Comparison between the spectra from the elevated sources with 3 mm and 6 mm diameter (measured at $z/\delta = 0.19$) and the ground level source (measured at $z/\delta = 0.0625$).

be interpreted in the light of the meandering scheme. Near the source, concentration fluctuations are mostly due to the plume meandering back and forth: a movement generating a highly intermittent signal when measured by a fixed probe. Eddies in the flow are bigger than the plume size and are able to shift the plume as a whole. This meandering motion occurs at small wavenumbers, corresponding to big length scales in the plume, and it is at this point that the difference between 3 and 6 mm spectra is more evident, with the small 3 mm source generating a plume with a marked meandering. At elevated wavenumbers, or fine length scales, relative diffusion is predominant and no significant difference is observed between the two source sizes. Figure 3.33 also clearly show the effect of varying height on plumes emitted by d = 3mm sources. The large scale fluctuations in the GLS are significantly reduced compared to the ES, since the plume is submitted to the dispersive action of smaller eddies than those experienced by the ES. Even in this case, the meandering scheme provide fulfilling explication for the differences observed in spectra. It is also worth noting how the smaller scale fluctuations appear to be more intense in the centre line of the GLS plume, which is much more sensitive to the small scale turbulence generated close to the wall.

In the far field, the plume has developed and its dimension is comparable to the bigger structures in the flow. In these conditions, the meandering motion is almost inexistent and relative diffusion is the phenomena governing plume dispersion. Concentration spectra far from the source superpose, irrespective of the source size and of the wavenumber. Concentration fluctuations however still show a significant dependence with the distance from the wall. The concentration spectra registered at the GLS plume centreline still shows a reduced contribution of large scale fluctuations and a most prominent role of the smaller eddies in the inertial range.

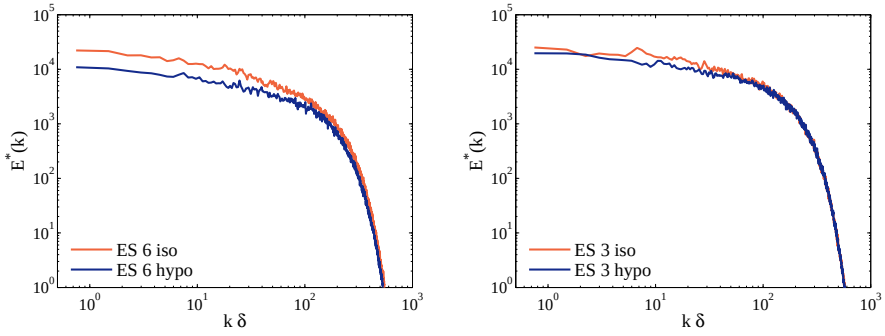

(a) $x/\delta = 0.3125$ ES 6 mm (b) $x/\delta = 0.3125$ ES 3 mm

Figure 3.34: Influence of the source emission velocity on spectra of concentration fluctuations. Comparison between isokinetic and hypokinetic conditions for spectra measured on the plume center line, at $x/\delta = 0.3125$.

Figure 3.34 shows spectra from different emission velocities at the source. The difference between isokinetic and hypokinetic conditions is evident and confirms that fluctuations are enhanced in the isokinetic case. This difference appears for both source sizes but is more evident for the bigger source.

3.5.10 Dissipation and production of concentration fluctuations

Considering diffusive transfer as negligible, due to the high Re number, and transversal and vertical mean flow component equal to zero, the balance equation of the concentration variance reduces to:

$$U\overline{\frac{\partial c^2}{\partial x_j}} + 2P + \overline{\frac{\partial u' c^2}{\partial x_j}} + 2\varepsilon_c = 0 \tag{3.53}$$

where the first term represents the mean advection and the third term represents turbulent diffusion, and where

$$P = \overline{u'_j c'}\frac{\partial C}{\partial x_j} \tag{3.54}$$

is the production term and ε_c is the rate of dissipation at which molecular diffusion dissipates scalar fluctuations by acting on local scalar gradients, defined as:

$$\varepsilon_c = D\left(\overline{\frac{\partial c'}{\partial x_j}\frac{\partial c'}{\partial x_j}}\right). \tag{3.55}$$

Our experimental data do not allow us to properly evaluate the different terms of Equation 3.53. The estimate of the mean advection term would require a finer spatial resolution to compute the variance gradients, we do not dispose of any simultaneous measurement of velocity and concentration to compute their correlations, and finally the frequency response of the FID ($\simeq 350Hz$) is too coarse to sample the fluctuations in the small dissipative scales.

However, in order to shed light on the mechanisms controlling the dispersion phenomenon, we can deduce estimates of the production and dissipation terms at varying distances from the source. Following Fackrell and Robins (1982b), we deduced ε_c from the measured spectra of concentration $E(k)$, to which is related by means of the following equation derived from a universal relationship for the inertial subrange:

$$E(k) = const. \times 2\varepsilon_c \varepsilon^{\frac{-1}{3}} k^{-\frac{5}{3}}, \tag{3.56}$$

where ε is the rate of dissipation of the velocity fluctuations and k is the wavenumber. Even though the $-5/3$ slope inertial region in the concentration spectra is narrow compared to velocity spectra, this estimate was proven to be quite accurate compared to estimates of ε_c obtained as residual of the Equation 3.53 (Fackrell and Robins, 1982a). Nevertheless, quite accurate here means affected by errors that can easily attain $\pm 25\%$.

Since we do not dispose of experimental values of the correlation term $\overline{u'_j c'}$, in order to estimate the production term we adopt a simple gradient closure model, so that:

$$P \simeq \overline{v'c'}\frac{\partial C}{\partial y} + \overline{w'c'}\frac{\partial C}{\partial z} \simeq \tag{3.57}$$

$$\simeq D_{ty}\left(\frac{\partial C}{\partial y}\right)^2 + D_{tz}\left(\frac{\partial C}{\partial z}\right)^2, \tag{3.58}$$

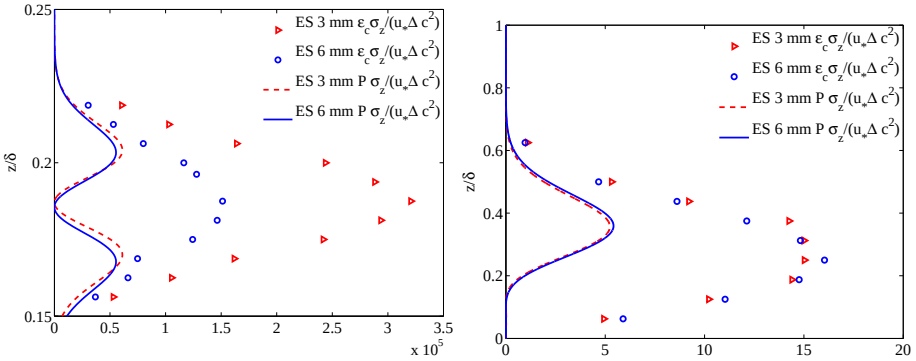

(a) $x/\delta = 0.3125$ (b) $x/\delta = 5$

Figure 3.35: Vertical profiles of the non dimensional dissipation of concentration fluctuations $\varepsilon_c\sigma_z/(u_*\Delta c^2)$ at a growing distance from the source. Comparison between the elevated sources with 3 mm and 6 mm diameter.

where the turbulent diffusivities, by definition, are expressed as a function of the plume spreads: $D_{ty}(x) = 2\sigma_y U/x$ and $D_{tz}(x) = 2\sigma_z U/x$.

Vertical profiles of the variance production and dissipation (in non-dimensional form) are shown in Figure 3.35, for two distances from the source: $x/\delta = 0.3125$ and $x/\delta = 5$. The dissipation is non-dimensionalised as $\varepsilon_c\sigma_z/(u_*\Delta_c^2)$. In the near field, the dissipation rate is higher for the small 3 mm source, while no significant differences are observed in the far field. At both locations, the production term for the two cases is almost the same, since the mean concentration field is almost not affected by the varying source size, and significantly lower than the dissipation term. This means that the higher σ_c^* registered for the $d = 3$ mm source (compared to the $d = 6$ mm one) has to be attributed to an enhanced production occurring over a distance lower than $x/\delta = 5$. As already enlightend by Fackrell and Robins (1982a), this shows the importance of focusing on the influence of varying emission conditions at the source, since most of the fluctuation production occurs very close to it.

It is usually assumed that the dissipation rate is intimately related to the phenomena of relative dispersion (Sawford and Hunt, 1986). We could then expect that higher ε_c are associated to more intense relative fluctuations, therefore concluding that relative dispersion in the near field is higher in the case of the smaller source (Figure 3.35). However, this conclusion contradicts what we could argue interpreting the results in the framework of Gifford's model (Equation 3.16). Since the plume spread σ_z is identical for the two sources (as shown in Figure 3.13a), and the meandering movement is predominant in the near field, we would expect that the small 3 mm source should have smaller relative dispersion. Our measurements therefore show that we can not identify a one-to-one relation between ε_c and relative dispersion, and that the intensity of ε_c is due to local concentration gradients produced not only by small scale fluctuations related to relative dispersion, but also on larger scale fluctuations induced by the plume meandering.

To further investigate the relation between the dissipation rate and the phenomena of relative dispersion we verified the reliability of a model proposed by

(Sawford and Hunt, 1986), which relates ε_c to the scales of motion in homogeneous turbulence, using similarity scaling arguments:

$$\varepsilon_c = \sigma_c^2 \sigma_w / L_{ww}(z), \tag{3.59}$$

where $L_{ww}(z)$ is the integral length scale of the w-component of velocity in the vertical direction, and which represents large-scale properties of the turbulence. However, another length scale is imposed on the concentration field by the plume extension σ_z, that is close to the source diameter in the near field and grows moving downwind. Then the scale ratio $\sigma_z / L_{ww}(z)$ influences the evolution of the scalar field. The scaling Equation 3.59 applies when $\sigma_z / L_{ww}(z) \sim 1$ or greater, so that relative dispersion is the only mechanism acting on the plume. In the far field ($x/\delta = 5$), $\sigma_z \sim 0.15$ m and $L_{ww}(z) \sim 0.056$ m (at the source elevation) and we are in the case of Equation 3.59, while in the near field ($x/\delta = 0.3125$), $\sigma_z \sim 0.01$ m and is smaller than the integral length scale. Experimental profiles are compared to the scaling Equation 3.59 in Figure 3.36. The scaling equation provides a value of ε_c that is of the same order of magnitude of the experiments. In the near field, experimental profiles are well reproduced by a factor of two. In the far field, instead, the difference between model and experiments is bigger and the model do not predict the exact shape of experimental profiles, due to the anisotropy of the velocity field.

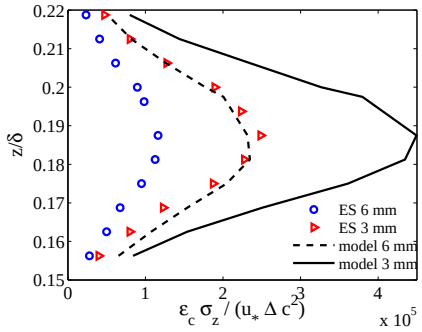

(a) $x/\delta = 0.3125$

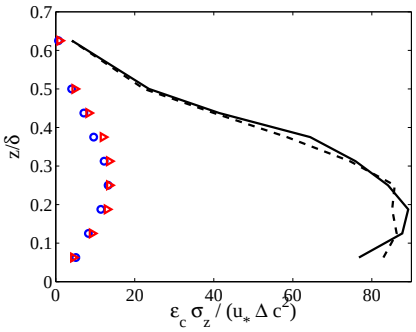

(b) $x/\delta = 5$

Figure 3.36: Dissipation ε_c at a growing distance from the source. Comparison with Equation 3.59

Part II

MODELLING

Chapter 4

MEANDERING PLUME MODELS

4.1 ABSTRACT

The reliability of meandering plume models was analysed by means of comparisons with our experimental measurements of a fluctuating plume dispersing in the turbulent boundary layer. Firstly, a simple two-dimensional plume model is implemented following the one proposed by Yee et al. (1994), to analyse the evolution of the model parameters M and λ. Than, to take into account the anisotropy and inhomogeneity of the concentration field in the TBL, the meandering model is extended to three dimensions. A focus is made on the modelisation of relative dispersion, by analysing the dependence of the model on the relative fluctuation intensity, i_{cr}, and on the plume spreads σ_y and σ_z.

4.2 INTRO

Fluctuating plume dispersion models are designed to predict the turbulent dispersion of continuous sources and to estimate the concentration statistics. The basic idea is to split the total plume dispersion into two independent components: meandering and relative dispersion. The first mechanism describes the fluctuation of the plume centre of mass, whereas the spreading concerns the relative dispersion of a plume element around its centre of mass. Meandering models were firstly formulated by Gifford (1959), who introduced the practice of partitioning concentration variability in a dispersing plume and who associated each mechanism with a characteristic length scale that is well-separated from the other. With this assumption, the absolute concentration PDF can be written as the convolution of the PDF of concentration p_{cr} in the meandering reference scheme (y_m, z_m) and the PDF of the location of the cloud instantaneous centroid p_m, characterizing the large scale random crosswind displacements of the mass centre:

$$p(c; x, y, z) = \int_{-\infty}^{\infty} \int_{-\infty}^{\infty} p_{cr}(c; x, y, z, y_m, z_m)\, p_m(x, y_m, z_m) dy_m dz_m, \qquad (4.1)$$

where c is the instantaneous concentration and p its PDF. Once that p is known, the moments of concentration can be computed as:

$$\overline{c^n}(x,y,z) = \int_0^\infty c^n p(c;x,y,z)dc. \tag{4.2}$$

The model derived by Gifford is isotropic and two-dimensional. It requires the homogeneity of the turbulence and internal concentration fluctuations are neglected, so that the PDF p_{cr} is parametrised by the Dirac delta function δ_D:

$$p_{cr}(c;x,y,z,y_m,z_m) = \delta_D\left(c - \overline{c}_r(x,y,z,y_m,z_m)\right). \tag{4.3}$$

This last hypothesis leads to the Gaussian distribution for the centroid positions and for the material distribution around the centre of mass. The hypothesis of neglecting internal concentration fluctuations is acceptable close to the source, where meandering is the main mechanism generating fluctuations, but it becomes unrealistic in the far field where the influence of meandering is significantly reduced.

Gifford's model was applied by Fackrell and Robins (1982a) to the study of concentration fluctuations downwind continuous point sources of different diameters. They measured the relative intensity of fluctuations at growing distances from the source and, by a suitable estimate of the dispersion coefficients, they evaluated the influence of the source size on the results.

Gifford's conceptual framework have been revised and generalised by many other authors. Sawford and Stapountzis (1986) extended the model to an anisotropic two-dimensional case. Yee et al. (Yee et al. (1994), Yee and Wilson (2000)) introduced the relative in-plume fluctuations in the model. They proposed a homogeneous model requiring two parameters, the fluctuation intensity and the meander ratio depending on the distribution of the plume centroid positions. To include the effects of relative diffusion due to small-scale fluctuations, a parametrisation for p_{cr} was proposed by several authors (Yee et al. (1994), Yee and Wilson (2000), Luhar et al. (2000)) that introduces a gamma distribution with the following form:

$$p_{cr}(c;x,y,z,y_m,z_m) = \frac{\lambda^\lambda}{\overline{c}_r\Gamma(\lambda)}\left(\frac{c}{\overline{c}_r}\right)^{\lambda-1}\exp\left(-\frac{\lambda c}{\overline{c}_r}\right), \tag{4.4}$$

where $\Gamma(\lambda)$ is the gamma function and $\lambda = 1/i_{cr}^2$, $i_{cr} = \sigma_{cr}/\overline{c}_r$ is the intensity of the relative concentration fluctuations (σ_{cr} is the standard deviation of relative concentration). The moments of the relative concentration assume the following shape:

$$\overline{c_r^n} = \frac{1}{\lambda^n}\frac{\Gamma(n+\lambda)}{\Gamma(\lambda)}\overline{c}_r^n, \tag{4.5}$$

with $\overline{c}_r$ is given by:

$$\overline{c}_r = \frac{M_q}{2\pi\sigma_r^2\overline{u}} exp\left[\left(\frac{(y-y_m)^2}{2\sigma_r^2}\right) + \left(\frac{(z-z_m)^2}{2\sigma_r^2}\right)\right], \tag{4.6}$$

where M_q is the source mass flow rate and $\overline{u}$ is the centroid mean velocity, assumed constant throughout the boundary layer height.

Another improvement in the model consists in taking into account the inhomogeneity of the turbulent velocity field in the vertical direction. Several

authors (Reynolds (2000), Luhar et al. (2000), Franzese (2003)) proposed to evaluate the plume centroid distribution by simulating the trajectories of puff centre of mass by means of a Lagrangian stochastic model. To separate the turbulent kinetic energy involved in the displacement of the plume centroid, they define a filter that is function of the relative plume spread.

In what follows, our aim is two folds. Firstly, we analyse the reliability of a two-dimensional model in order to predict concentrations at ground level and source height and to analyse the evolution of the model parameters. Secondly, we extend the model from Yee and Wilson (2000) to take into account the anisotropy and inhomogeneity of the concentration field.

4.3 MEANDERING PLUME MODEL 2D

The fluctuating plume model formulation presented here follows the one proposed by Yee et al. (1994) and Yee and Wilson (2000). The first is a two dimensional model and has been used for predictions in a boundary layer in neutral conditions, for a fixed distance from the ground. The second has a slightly different formulation and applies to isotropic dispersion. It was validated for dispersion in grid generated turbulence.

The functional form of the two PDFs, p_{cr} and p_m, have to be defined a priori. It is generally assumed that p_m is well approximated by a Gaussian distribution, considering that the plume meandering takes place only in the horizontal direction we have:

$$p_m(x, y_m) = \frac{1}{\sqrt{2\pi}\sigma_{ym}(x)} exp\left(-\frac{y^2}{2\sigma_{ym}^2(x)}\right), \tag{4.7}$$

where $\sigma_{ym}(x)$ is the standard deviation (spread) in the y-direction of the plume centroid position.

The functional form of p_{cr} differs according to the authors: log-normal distribution (Csanady, 1973), exponential distribution (Sawford and Stapountzis, 1986), a combination of exponential and generalized Pareto distribution (Lewis and Chatwin, 1995), clipped Gaussian distribution (Lewellen and Sykes (1986), Mylne and Mason (1991), Luhar et al. (2000)). Following Yee et al. (1994) and Yee and Wilson (2000), we assume here a Gamma distribution:

$$p_{cr}(c; x, y, z, y_m, z_m) = \frac{\lambda^\lambda}{\overline{c}_r \Gamma(\lambda)} \left(\frac{c}{\overline{c}_r}\right)^{\lambda-1} \exp\left(-\frac{\lambda c}{\overline{c}_r}\right), \tag{4.8}$$

where $\overline{c}_r$ denotes the mean concentration on a transverse plane of the dispersing plume, measured relative to the centroid location at a downwind distance x. $\overline{c}_r$ is assumed to be Gaussian with standard deviation $\sigma_{yr}(x)$:

$$\overline{c}_r = \overline{c}_{r0}(x) exp\left(-\frac{y^2}{2\sigma_{yr}^2(x)}\right), \tag{4.9}$$

being $\overline{c}_{r0}(x)$ the centreline value.

The parameter λ is equal to the inverse of the fluctuation intensity in relative coordinates: $\lambda = 1/i_{cr}^2$, with $i_{cr} = \sigma_{cr}/\overline{c}_r$. It is assumed that λ depends on x only. As a consequence λ is constant in the transverse planes, meaning that we are assuming isotropy along the y-direction.

Resolving Equation 4.1 assuming Eqs. 4.7, 4.8, 4.9 for the functional form of p_m and p_{cr} leads to an analytical expressions for the concentration PDF $p(c; x, y)$ and therefore to the concentration shape parameters, namely, the fluctuation intensity $i^2 \equiv \overline{c'^2}/\overline{c}$, the skewness $S \equiv \overline{c'^3}/\overline{c'^2}^{3/2}$ and the kurtosis $Ku \equiv \overline{c'^4}/\overline{c'^2}^2$, where c' is the fluctuating concentration. All these quantities are dependent on two parameters, which admit a physical interpretation. The first one is the meandering ratio $M = \sigma^2_{ym}/\sigma^2_{yr}$, defined as the ratio between the plume meander variance and the instantaneous plume width variance, which is related to the larger scale fluctuations. The second is the previously defined $\lambda = 1/i^2_{cr}$, which is related to the effects of the smaller scale fluctuations. In both models proposed by Yee et al. (1994) and Yee and Wilson (2000), these parameters are assumed to be dependent on the distance from the source only, which implies constant values along the y and z axes.

4.3.1 Results

The model parameters M and λ have been computed by means of the experimentally measured concentration statistics. The meandering ratio M is related to the spread σ_{ny} of the spatial distribution of the n-th moment of the concentration PDF (for n=2,3,4) and to the lateral spread σ_y of the mean concentration, by means of the relation (Yee and Wilson, 2000; Yee et al., 1994):

$$M = \frac{1 - nR_n}{n(R_n - 1)}, \text{ where } R_n = \frac{\sigma^2_{ny}}{\sigma^2_y}. \tag{4.10}$$

The values of σ_{ny} and σ_y are inferred by fitting a Gaussian law to the measured crosswind profiles of concentration moments about zero, for $n = 2, 3, 4$. The parameter λ is chosen so that the modelled value of the fluctuation intensity i^2 (Equation 4.11) matches the measured one at the mean-plume centreline (with $\overline{c}/\overline{c_0} = 1$, where $\overline{c}$ is the mean concentration and $\overline{c_0}$ is its centreline value):

$$i^2 = \frac{\lambda + 1}{\lambda} \frac{1 + M}{\sqrt{1 + 2M}} \frac{\overline{c}}{\overline{c_0}}^{-\frac{2M}{1+2M}} - 1. \tag{4.11}$$

We analyse the stream-wise evolution of the model parameters focusing on M_2 and λ_2, which are computed for $n = 2$, on the plume centreline and at a fixed distance z from the ground corresponding to the source elevation. The variability of λ with n is of the order of 2% at every downwind position, therefore we can retain that λ is independent of n. M is independent of n starting from $x/\delta = 2.5$, where its variability as about 2%. Close to the source the variability of M_n is much greather (about 50%), probably due to the increasing uncertainty affecting the measurement of third and fourth moments in the near field. Since M_2 and λ_2 are the most reliable parameters, we decided to use them in the model.

This simple 2D model allows us to enlighten the dynamical behaviour of the plumes. In the ES case, the meandering ratio M_2 increases rapidly moving away from the source, attains a peak and then decreases asymptotically to zero (Figure 4.1a). The intensity of this large scale motion, as expected, is higher for the 3 mm source than for the 6 mm source. Meandering motion is inhibited in the case of the GLS.

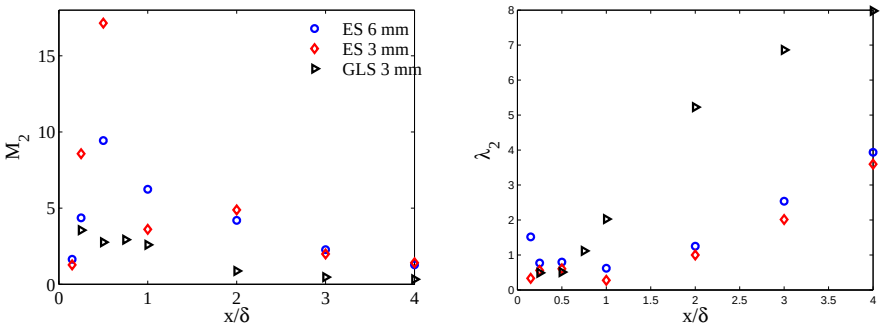

(a) $M_2(x/\delta)$ (b) $\lambda_2(x/\delta)$

Figure 4.1: Stream-wise evolution of the model parameters M_2 and λ_2, inferred from profiles of concentration variance (for $n = 2$).

The evolution of λ_2 for the three sources has a similar trend, increasing monotonically moving away from the source (Figure 4.1b). For the ES case, relative dispersion is only slightly affected by the source size. Conversely, the source elevation has a major effect in reducing drastically the intensity of relative fluctuation and therefore producing values of λ_2 in GLS that are significantly larger than those observed for the ES sources.

Vertical variation of model parameters and comparison with experimental results

Our aim is to verify the reliability of the model for predictions in boundary layer flows which may be useful for operational purposes. To do so, we check the hypothesis of constant M and λ in the vertical direction and we compare the model prediction with experimental results at the source height for varying distances downwind. The analysis focuses on the case of the ground level emission.

The results, which are shown in Figure 4.2, indicate that the trend in the z-direction, for both M and λ, is far from being constant. Furthermore, the variability in the z-direction for each parameter depends on the downwind position. M grows faster close to the source compared to the slower increase of its z-profile measured at a distance of $x/\delta = 2.5$. λ, instead, slightly decreases at $x/\delta = 0.625$ and shows a drop at $x/\delta = 2.5$. This first analysis shows that the model parameters vary significantly with the distance from the ground, and that this dependence changes with increasing stream-wise distances. This feature makes difficult the adoption of simple functions defined empirically to model this dependence.

The model from Yee et al. (1994) was adopted and the model predictions are compared with measured crosswind profiles of fluctuation intensity, skewness and kurtosis (Figures 4.3a,4.3b,4.3c) for the case of the ground level source. In these comparisons we consider only concentration profiles measured at the source height ($z/\delta = 0.0625$). In doing that, we will adopt the values of M and λ related to the plume centreline and estimated with the 2nd moment transversal profiles (data are shown in Figure 4.2). Profiles are normalised as

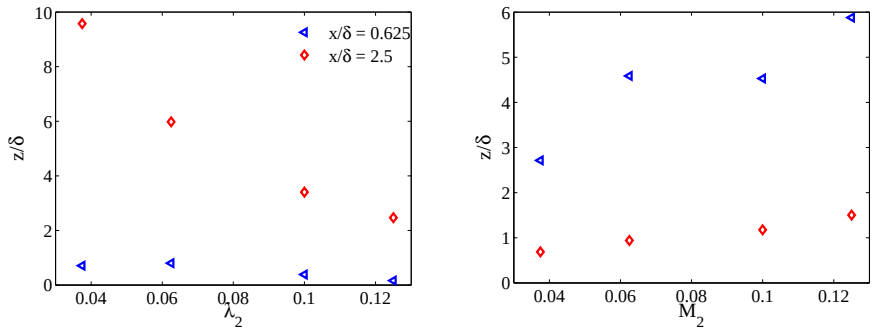

(a) $\lambda_2(z/\delta)$ (b) $M_2(z/\delta)$

Figure 4.2: Vertical evolution of the model parameters λ_2 and M_2 for the case of the GLS. Parameters are inferred from profiles of concentration variance ($n = 2$), for two distances from the source: $x/\delta = 0.625$ and $x/\delta = 2.5$.

C/C_{hs}, being C the mean concentration and C_{hs} the mean concentration on the plume centerline (at the source haight). The model equations used are reported in Yee et al. (1994).

The relative error on crosswind profiles, calculated as

$$ER = 100(\text{ExpValue} - \text{ModelledValue})/\text{ExpValue}, \tag{4.12}$$

is shown for each shape parameter in Figures 4.3d,4.3e, 4.3f. An overall agreement is observed between the model and the observations, yet the relative error grows increasing the moment order, reaching the 30% in the kurtosis profile. The mean and maximum ER along the streamwise direction is shown in Figures 4.3g, 4.3h, 4.3i. Speaking about fluctuation intensity and skewness, the mean ER in the near field (viz. from $x/\delta = 0.625$ to $x/\delta = 2.5$) is 5 and 10% respectively, but it rises starting from $x/\delta = 2.5$. In particular, the model shows significant differences with the experimental measurements in the far field. An opposite behaviour is observed for the kurtosis, for which the greater errors are located close to the source. This augmentation of the relative error can be explained with the emergence of off-centreline peaks in the moments transversal profiles, that appear starting from a distance of $x/\delta = 2.5$ from the source (see measured profile of the rms in Fig. 3.20 and of the third and fourth moments in Figures 3.22 and 3.24 respectively).

Concentration PDFs were calculated analytically according to Yee et al. (1994) and are reported in Figure 4.4, where they are compared to the measured PDFs. PDFs are situated on the plume centreline, at two distances from the source ($x/\delta = 1.25$ and $x/\delta = 5$). Concentration is non-dimensionalised as C/C_{hs}. Also in this case, the agreement with the model is satisfactory in the near field. In the far field, the modelled PDF has the same qualitative shape of the experimental one but is shifted to lower levels of concentration.

This analysis showed that, for a pollutant plume dispersion within a turbulent boundary layer, the model parameters M and λ are highly dependent on the vertical coordinate. However, considering concentration at a fixed distance from the ground only, comparisons between model predictions and experimen-

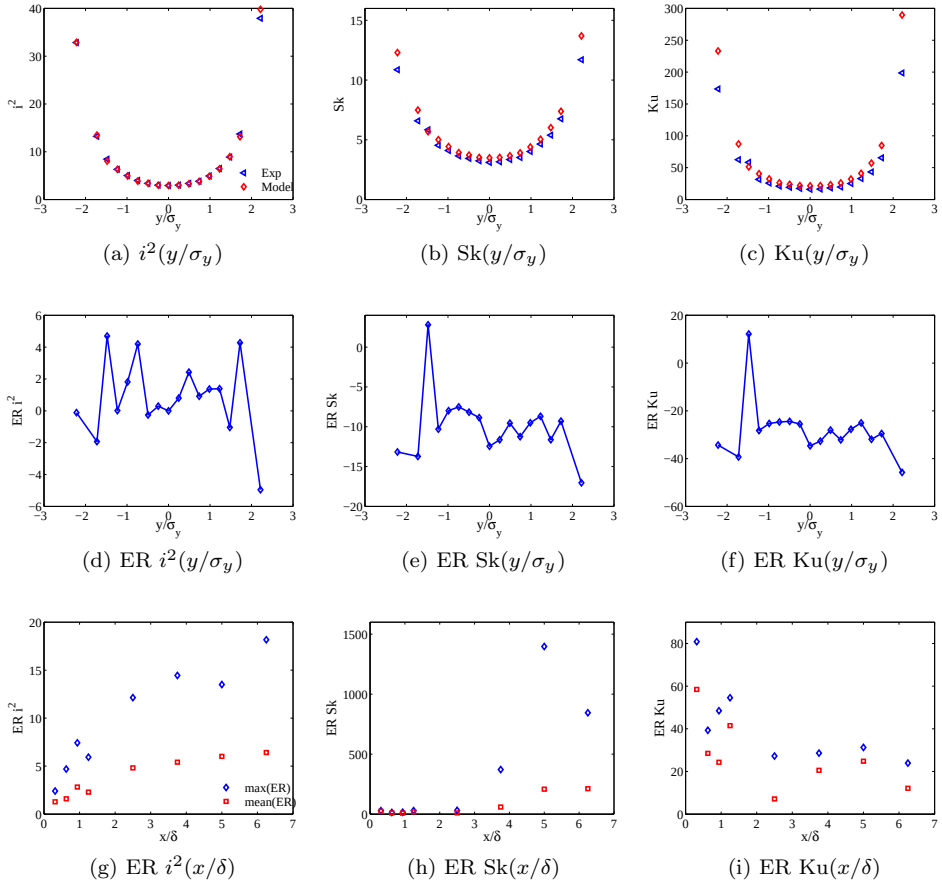

(a) $i^2(y/\sigma_y)$ (b) $\mathrm{Sk}(y/\sigma_y)$ (c) $\mathrm{Ku}(y/\sigma_y)$

(d) ER $i^2(y/\sigma_y)$ (e) ER $\mathrm{Sk}(y/\sigma_y)$ (f) ER $\mathrm{Ku}(y/\sigma_y)$

(g) ER $i^2(x/\delta)$ (h) ER $\mathrm{Sk}(x/\delta)$ (i) ER $\mathrm{Ku}(x/\delta)$

Figure 4.3: a), b), c) Comparison between measured and modelled crosswind profile of concentration statistics for the GLS case. Graphics refer to the position $x/\delta = 0.625$ and source elevation ($z/delta = 0.0625$). d), e), f) Relative Error (ER) in crosswind profiles. g), h), i) mean and max ER along the streamwise axis, at the plume centreline.

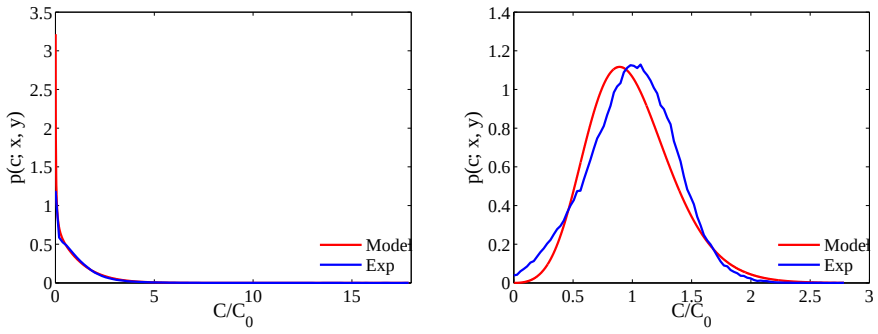

(a) $x/\delta = 1.25$ (b) $x/\delta = 5$

Figure 4.4: Comparison between modelled and measured concentration PDFs.

tal results show overall good agreement in the near field. This model can be applied for operational purposes to predict pollutant concentration moments at a fixed distance from the ground. This may be the case for example of ground level concentrations. On the other hand, if the purpose is to achieve a complete description of the concentration field, the model should be reformulated to consider the variability of the fundamental parameters in the vertical direction.

4.4 MEANDERING PLUME MODEL 3D

In developing a three-dimensional formulation of the fluctuating plume model, we aim in defining a parametrisation that allows a reliable representation of the inhomogeneity and anisotropy of the dispersion process within a turbulent boundary layer.

By assuming the statistical independence of the plume meander in the lateral and vertical directions, p_m is splitted in two components p_{ym} and p_{zm} :

$$p_m(x, y_m, z_m) = p_{ym}(x, y_m) p_{zm}(x, z_m). \tag{4.13}$$

We than need to define the concentration statistics $\overline{c_r^n}$ in the relative coordinate system (y_m, z_m) as

$$\overline{c_r^n}(x, y, z, y_m, z_m) = \int_0^\infty c^n p_{cr}(c; x, y, z, y_m, z_m) dc, \tag{4.14}$$

where p_{cr} is the Gamma probability density function defined in Equation 4.4. To take into account the anisotropy and inhomogeneity of the small scale fluctuations we parametrise the relative mean concentration $\overline{c}_r$ as :

$$\overline{c}_r = \frac{M_q}{\overline{u}} \, p_{yr}(x, y, y_m) \, p_{zr}(x, z, z_m), \tag{4.15}$$

where p_{yr} and p_{zr} are the lateral and vertical components of the concentration distribution around the plume centre of mass. The PDFs p_{yr} and p_{zr} are defined

as follows:

$$p_{yr} = \frac{1}{\sqrt{2\pi}\sigma_{yr}} \exp\left(-\frac{(y-y_m)^2}{2\sigma_{yr}^2}\right), \tag{4.16}$$

$$p_{zr} = \frac{1}{\sqrt{2\pi}\sigma_{zr}} \left\{\exp\left(-\frac{(z-z_m)^2}{2\sigma_{zr}^2}\right) + \exp\left(-\frac{(z+z_m)^2}{2\sigma_{zr}^2}\right)\right\}, \tag{4.17}$$

where σ_{yr}^2 and σ_{zr}^2 are the horizontal and vertical variance of the plume relative dispersion around its centre of mass in the horizontal and vertical direction, respectively.

Since the turbulence is assumed to be homogeneous in the horizontal planes, the crosswind distribution of centroid locations is Gaussian:

$$p_{ym}(x, y_m) = \frac{1}{\sqrt{2\pi}\sigma_{ym}} \exp\left(-\frac{(y_m - y_s)^2}{2\sigma_{ym}^2}\right), \tag{4.18}$$

with σ_{ym} being the centroid horizontal spread.

Conversely, the turbulence in the vertical direction is not homogeneous. For this reason, previous authors have estimated p_{zm} by simulating the trajectories of the cloud centroid using a Lagrangian stochastic model (Reynolds (2000), Franzese (2003)). Here, to take into account this dishomogeneity and to keep the model as simple as possible, to a first approximation we parametrise p_{zm} through the bi-Gaussian distribution:

$$p_{zm}(x, z_m) = \frac{1}{\sqrt{2\pi}\sigma_{zm}} \left\{\exp\left[-\frac{(z_m - z_s)^2}{2\sigma_{zm}^2}\right] + \exp\left[-\frac{(z_m + z_s)^2}{2\sigma_{zm}^2}\right]\right\}, \tag{4.19}$$

where σ_{zm} is the centroid vertical spread and z_s is the vertical distance of the source from the ground level.

The choice of a bi-Gaussian shape of p_{zm} instead of a simple Gaussian deserves to be discussed. Since the effect of the ground makes ineffective the hypothesis of homogeneous turbulence along the z-coordinate, the model has to include the reflection of the plume in order to assure the mass conservation. Fig. 4.5 shows the mass-rate evaluated along the longitudinal coordinate

$$M_q(x) = \int_{-\infty}^{+\infty} \int_0^{+\infty} \overline{c^1}(x, y, z)\overline{u}(z) dy dz. \tag{4.20}$$

It is worth noting that the bi-Gaussian keeps the mass-consistence, whereas the simple Gaussian is not able to achieve this condition: far from the source, where the reflection effect is more important, we observe a loss of (adimensioned) mass.

The n-th concentration moment as function of the space position (x, y, z) is given by:

$$\overline{c^n}(x, y, z) = \left(\frac{M_q}{\sqrt{2\pi}\sigma_{yr}\overline{u}}\right)^n \frac{1}{\lambda^n} \frac{\Gamma(n+\lambda)}{\Gamma(\lambda)} \frac{\sigma_{yr}}{\left(n\sigma_{ym}^2 + \sigma_{yr}^2\right)^{0.5}}$$
$$\times \exp\left[-\frac{n(y-y_s)^2}{2\left(n\sigma_{ym}^2 + \sigma_{yr}^2\right)}\right] \int_0^{\infty} p_{zr}^n(x, z, z_m) p_{zm}(x, z_m) dz_m. \tag{4.21}$$

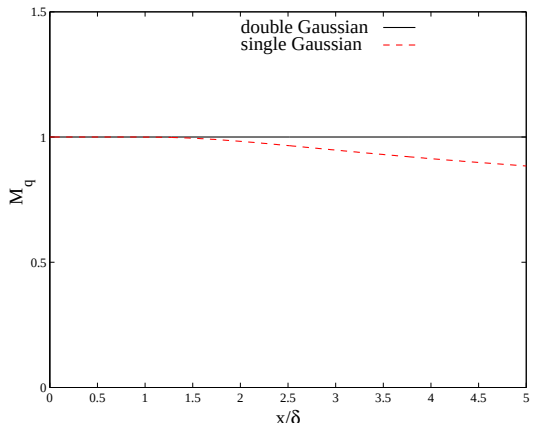

Figure 4.5: Adimensioned mass-rate in the streamwise direction x/δ.

Now we need to parametrise the dispersion coefficients σ_y, σ_{yr}, σ_{ym}, σ_z, σ_{zr}, σ_{zm} and the model parameter i_{cr}. The centroid and relative variances are related with the global dispersion coefficient in the following way:

$$\sigma_y^2 = \sigma_{ym}^2 + \sigma_{yr}^2, \tag{4.22}$$

$$\sigma_z^2 = \sigma_{zm}^2 + \sigma_{zr}^2. \tag{4.23}$$

The global variance can be parametrised by an equation derived from Taylor's statistical theory, taking into account the initial spread σ_0 (equal to the source diameter). The variances σ_y and σ_z are a function of the turbulent velocity fluctuations (σ_v and σ_w), the temporal coordinate t and the Lagrangian timescale:

$$\sigma_y^2 = \sigma_0^2 + 2\sigma_v^2 T_{Lv}\left\{t - T_{Lv}\left[1 - \exp\left(-\frac{t}{T_{Lv}}\right)\right]\right\}, \tag{4.24}$$

$$\sigma_z^2 = \sigma_0^2 + 2\sigma_w^2 T_{Lw}\left\{t - T_{Lw}\left[1 - \exp\left(-\frac{t}{T_{Lw}}\right)\right]\right\}. \tag{4.25}$$

As customary, the Lagrangian timescales are parametrised as:

$$T_{Lv} = \frac{2\sigma_v^2}{C_0\varepsilon} \tag{4.26}$$

$$T_{Lw} = \frac{2\sigma_w^2}{C_0\varepsilon}, \tag{4.27}$$

where C_0 is the Kolmogorov constant and ε is the dissipation rate of turbulent kinetic energy from experimental measurements (see Figure 2.5.1). The transverse relative variance, σ_{yr}^2, is parametrised as follows:

$$\sigma_{yr}^2 = \frac{(C_r/6)\varepsilon\left(t_s + t\right)^3}{\left\{1 + \left[(C_r/6)\varepsilon t^2/\left(2\sigma_v^2 T_{Lv}\right)\right]^{2/3}\right\}^{3/2}}, \tag{4.28}$$

where $t_s = \left[\sigma_0^2/(C_r\varepsilon)\right]^{1/3}$ depends on the source size σ_0 and C_r is the Richardson-Obukhov constant taken equal to 1.4. This parametrisation respects

the inertial range relative dispersion at small time ($\sigma_{yr}^2 \sim C_r\varepsilon(t_s+t)$), and it asymptotically tends to Taylor's limit at large time ($\sigma_{yr}^2 = 2\sigma_v^2 T_{Lv} t$).

The same parametrisation can not be adopted for the vertical relative dispersion coefficient σ_{zr}^2 since the reflection on the ground reduces the influence of the meandering process more quickly in the vertical direction (Franzese (2003), Mortarini et al. (2009)). To resolve the problem of the effect of the surface, the parametrisation adopted in the model introduces a timescale T_m representing the time when the meandering process becomes negligible with respect to the relative dispersion. T_m is assumed to be proportional to the Lagrangian macroscale, $T_m = \alpha_t T_{Lw}$, where α_t is taken equal to 3. This means that when the plume size is bigger or equal to the Lagrangian macroscale, the meandering motion in the vertical direction is switched off. The behaviour of σ_{zr}^2 corresponds to the inertial dispersion formulation at small times and is in agreement with the limit of Taylor's formula at large times:

$$\sigma_{zr}^2 = \frac{(C_r/6)\varepsilon\,(t_s+t)^3}{\left\{1+\left[(C_r/6)\varepsilon t^2/\left(2\sigma_w^2 T_{Lw}\right)\right]^{2/5}\right\}^{5/2}} \exp\left[-\left(\frac{t}{T_m}\right)^2\right] + \tag{4.29}$$

$$2\sigma_w^2 T_{Lw}\left\{t - T_{Lw}\left[1-\exp\left(-\frac{t}{T_{Lw}}\right)\right]\right\}\left\{1-\exp\left[-\left(\frac{t}{T_m}\right)^2\right]\right\}.$$

Eqs. (4.24) and (4.25) differs from the equations presented by other authors (Franzese (2003); Luhar et al. (2000)) since they introduce an initial spread σ_0^2 equal to the source size. If σ_0^2 is not taken into account, close to the source, where the particle flight time t is very small, the relative dispersion can be larger than the global dispersion and, consequently, the meandering coefficient becomes unrealistically negative. Figs. 4.6a and 4.6b show that in the vertical direction the relative coefficient approaches the global coefficient more quickly and far from the source the meandering influence becomes negligible.

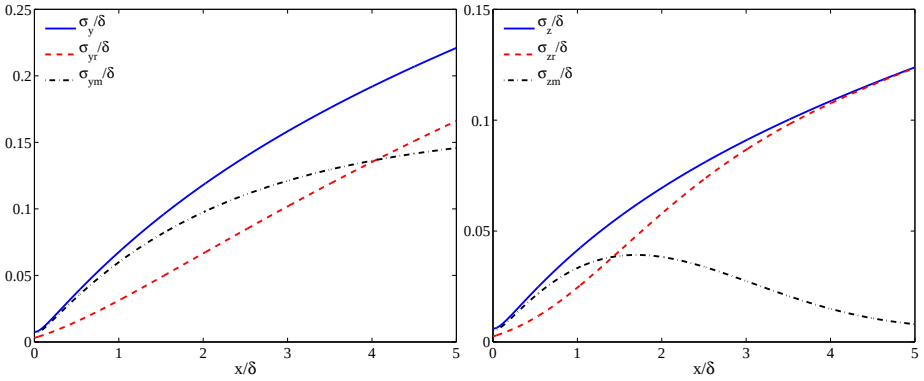

(a) σ_y/δ, σ_{yr}/δ, σ_{ym}/δ vs x/δ (b) σ_z/δ, σ_{zr}/δ, σ_{zm}/δ vs x/δ

Figure 4.6: Modeled transversal and vertical dispersion coefficients for the elevated source with diameter 3 mm and $C_0 = 4.5$.

4.4.1 Results

In order to reduce the influence of the shear we consider the plume development and we evaluate the velocity field at the plume centre of mass, $z_m(x)$, that is a function of the longitudinal coordinate x.

The reliability of the model defined by the Eq. (4.21) is tested against the experimental measurements of concentration we carried out in the wind tunnel.

Centred concentration moments up to the fourth order are related to the moments $\overline{c^n}$ about zero by means of the following relations:

$$
\begin{aligned}
m_1 &= C = \overline{c^1} \\
m_2 &= \sigma_c^2 = \overline{c^2} - C^2 \\
m_3 &= \overline{c^3} - 3\overline{c^2}C + 2C^3 \\
m_4 &= \overline{c^4} - 4\overline{c^3}C + 6\overline{c^2}C^2 - 3C^4
\end{aligned}
$$

and they are adimensionalised as:

$$
m_i^* = {m_i}^{1/i} \frac{u_\infty \delta^2}{M_q}. \tag{4.30}
$$

Estimate of Lagrangian Kolmogorov constant

The Lagrangian Kolmogorov constant C_0 determines the effective turbulence diffusion in velocity space. Although it should be a universal constant, the value differs according to the authors. Lien and D'Asaro (2002) carried out a series of direct numerical simulations with increasing large micro-scale Reynolds number and estimated C_0 as equal to 6 ± 0.5. Rizza et al. (2006) estimated $C_0 = 4.3 \pm 0.3$ by tracking an ensemble of Lagrangian particles in a planetary boundary layer simulated through large-eddy simulation. Du and Sawford (1995) found $C_0 = 3.0 \pm 0.5$ in decaying grid turbulence. In conclusion, the estimated values of Kolmogorov constant vary within the range $2.0 - 7.0$.

Following a common approach, we treat C_0 as a free parameter and we set its value in order to minimize the difference between the modelled and measured mean concentration, evaluated in Euclidean norm $||\overline{c}_{exp} - \overline{c}_{mod}||_2$. We find that $C_0 = 4.5$ is the value that better satisfies this criterion.

Dispersion coefficients σ_y/δ and σ_z/δ are reported in Figures 4.7a and 4.7b. It is shown that some discrepancies occur between measured and modelled dispersion coefficients, especially in the far field, causing a decrease in the accuracy of the model.

Estimate of the intensity of relative concentration fluctuations

While in homogeneous and isotropic turbulence the intensity of relative concentration fluctuations i_{cr} is generally assumed to be only dependent on the x-coordinate, in the TBL it is also function of the distance from the ground and of the source elevation.

To parametrise i_{cr} for the TBL, we adopted a procedure that consists in evaluating the vertical and transversal profiles of the modelled concentration standard deviation (σ_c^{mod}) and to compare them with the experimental ones (σ_c^{exp}). For each profile we choose the value of i_{cr} that minimize the Euclidean

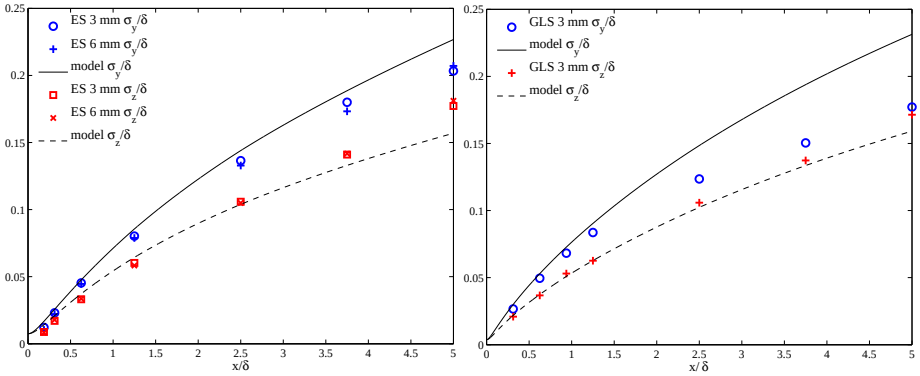

(a) σ_y/δ, σ_z/δ vs x/δ, ES cases

(b) σ_y/δ, σ_z/δ vs x/δ GLS case

Figure 4.7: Global dispersion coefficients σ_y/δ and σ_z/δ, comparison between the experimental measurements and the model with $C_0 = 4.5$.

norm $||\sigma_c^{exp} - \sigma_c^{mod}||_2$ and, as a consequence, we obtain the values of i_{cr} that globally fit the experimental results. For each distance downwind, a series of values of i_{cr} is calculated as function of x/δ and the following bonds are:

$$\begin{aligned} &\text{at } \frac{x}{\delta} \to 0 \quad i_{cr} \to 0, \\ &\text{at } \frac{x}{\delta} \to \infty \quad i_{cr} \to i_c = \frac{\sigma_c}{C} \neq 0. \end{aligned} \tag{4.31}$$

By applying a least-squares fitting, we derive the following empirical relationship:

$$i_{cr} = x_{ad} \frac{p_1 x_{ad}^2 + p_2 x_{ad} + p_3}{x_{ad}^3 + q_1 x_{ad}^2 + q_2 x_{ad} + q_3}, \tag{4.32}$$

where $x_{ad} = x/\delta$ is the adimensional longitudinal coordinate.

The consistence of the procedure for the evaluation of i_{cr} is verified by comparing the results to the experimental values. To calculate the experimental value of i_{cr} we used an equation based on the model distribution and including a term derived by experiments $((\sigma_c^2/C^2)_{exp})$:

$$i_{cr}^2 = \left[\left(\frac{\sigma_c^2}{C^2} \right)_{exp} + 1 \right] \sigma_{yr} \frac{(2\sigma_{ym}^2 + \sigma_{yr}^2)^{0.5}}{\sigma_y^2} \frac{\left[\int_0^\infty p_{zr}(x,z,z_m) p_{zm}(x,z_m) dz_m \right]^2}{\int_0^\infty p_{zr}^2(x,z,z_m) p_{zm}(x,z_m) dz_m} - 1 \tag{4.33}$$

where $(\sigma_c/C)_{exp}$ is the fluctuation intensity measured on the plume centreline $(y = y_s, z = z_s)$. The results are reported in Fig 4.8, where the curves of the intensity of relative concentration fluctuations are shown for the ES and GLS configurations. We report only the results evaluated by the minimization technique because they are related to the global behaviour of the model.

In both ES and GLS cases (Figs. 4.8a and 4.8b respectively), i_{cr} exhibits an initial growth and thereafter decreases monotonically to an asymptotic value,

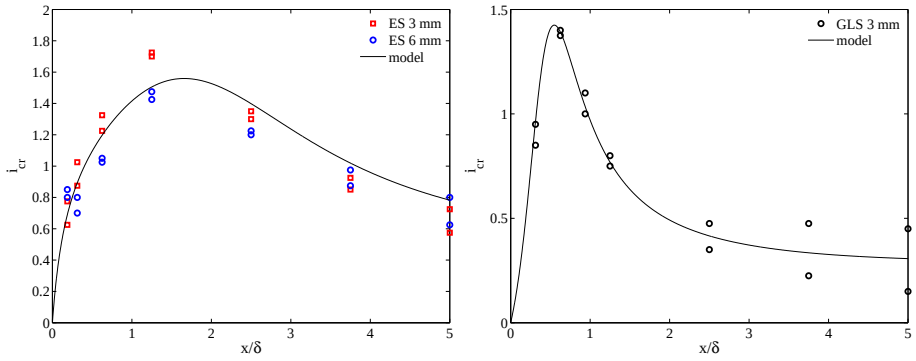

(a) ES (b) GLS

Figure 4.8: Intensity of relative concentration fluctuations i_{cr} vs x/δ. Experimental points are compared to the model of Eq.4.32 (solid line).

which is reached far from the source, consistently with the physics of the phenomenon. The values of the parameters in Eq.4.32 are summarised in Table 4.1, for ES and GLS sources. We observe that ES and GLS configurations reach the same asymptotic value of relative concentration fluctuation (at $x/\delta \to \infty$, $i_{cr} \to 0.4$).

	p_1	p_2	p_3	q_1	q_2	q_3
ES	0.4	-0.7	8.0	-2.5	5.8	1.14
GLS	0.4	1.2	5.0	10.0	-7.2	3.0

Table 4.1: Parameters used in Eq.4.32 to calculate the intensity of relative concentration fluctuations i_{cr}.

In Figs. 4.9 is shown a comparison between the intensity of concentration fluctuations from experiments i_c and the intensity of relative concentration fluctuations i_{cr}. Figure 4.9 shows that the bonds in Equation 4.31 are respected by the model. As expected, in the far field i_{cr} tends to i_c meaning that relative dispersion is the only mechanism responsible of the plume dispersion, while in the near field there is a gap between the experimental i_c and the modelled i_{cr} that is due to the meandering motion.

In the next section we verify the suitability of the coupling of Eq. 4.21 with Eq. 4.32 by comparing the 3^{rd} and 4^{th} numerical concentration moments with the experimental ones.

We recall that in the following discussion we do not use i_{cr} values that minimize the Euclidean norm, but we compute them through Eq. (4.32). In this way we privilege the use of a general rule, partly sacrificing the quality of the results.

Elevated source

The elevated source is located at $z/\delta = 0.19$ and is therefore less affected by the boundary layer shear, compared to the ground level source.

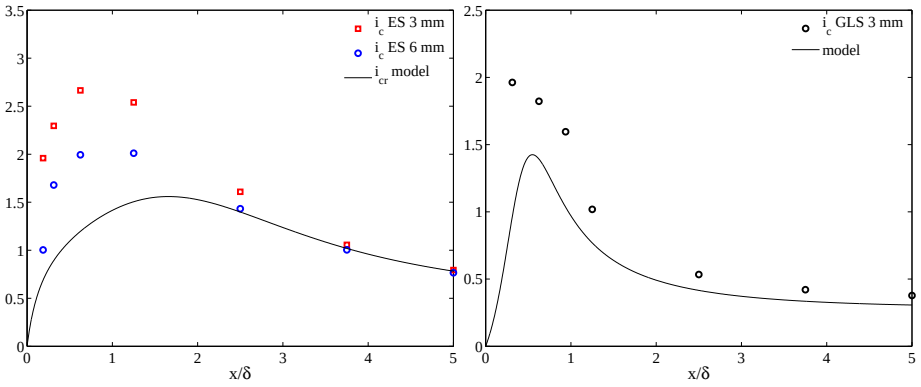

(a) ES (b) GLS

Figure 4.9: Experimental intensity of concentration fluctuations i_c and modelled intensity of relative concentration fluctuations i_{cr} vs x/δ.

Fig. 4.10 shows the ratio of the central concentration statistics (σ_c, $m_3^{1/3}$ and $m_4^{1/4}$) and mean concentration C, evaluated on the plume centreline, as function of x-coordinate. In spite of some simplifying assumptions, we observe that the model is able to simulate the influence of the source size and the agreement between the experimental and numerical results is qualitatively acceptable for all the moments.

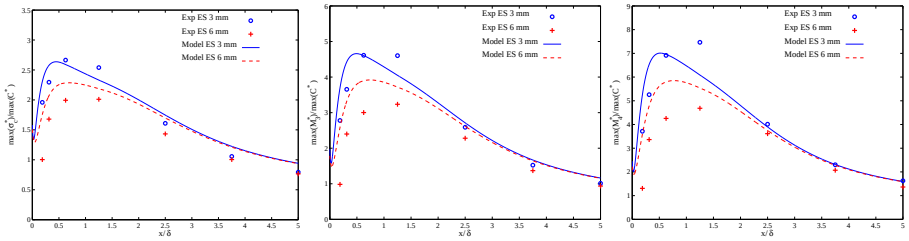

(a) σ_c^*/C^* (b) M_3^*/C^* (c) M_4^*/C^*

Figure 4.10: Concentration statistics vs x/δ evaluated at the source location $(y_s/\delta, z_s/\delta)$.

Close to the source, mean concentration profiles do not depend on the source size (Figs. 4.11a and 4.12a). On the contrary, in the near field the profiles of σ_c, m_3^* and m_4^* are influenced by the source size. The agreement between the experimental and modelled values of σ_c is satisfactory (Figs. 4.11b and 4.12b). The 3^{rd} and 4^{th} centred moments present a lower accordance, that however can be still considered fairly good (see Figs 4.11c, 4.11d, 4.12c, 4.12d). We recall that the second order moments are tuned by a suitable choice of the i_{cr} function, but no adjustment is performed on higher statistics.

Going far from the source, the influence of the source size becomes negligible and for different diameters the profiles appear quite overlapped. The agree-

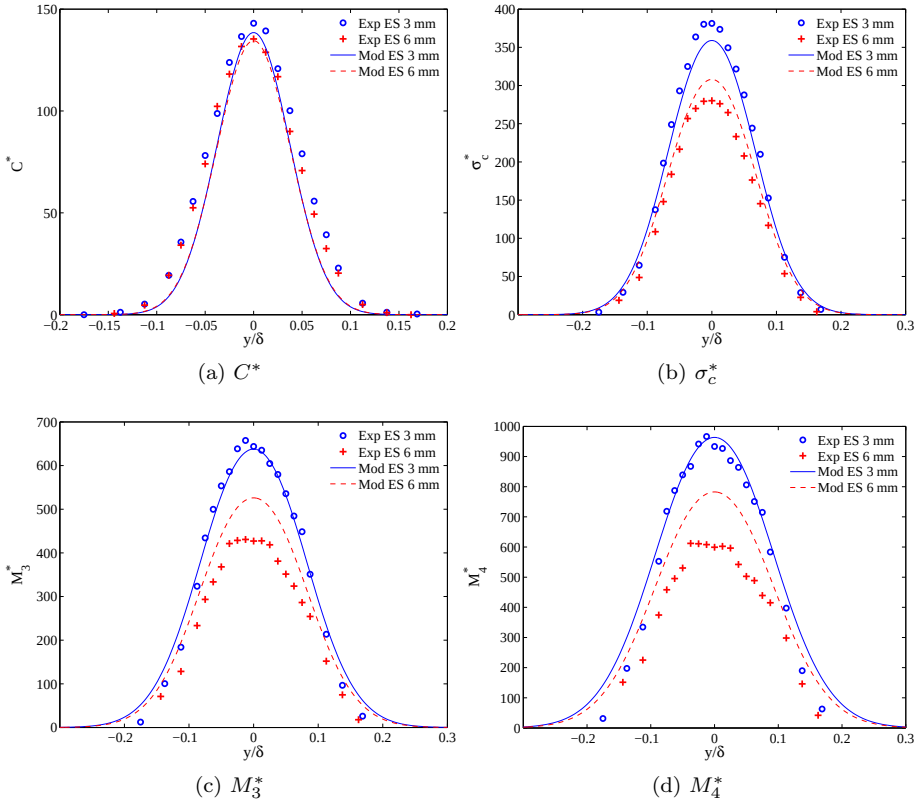

(a) C^* (b) σ_c^*

(c) M_3^* (d) M_4^*

Figure 4.11: Concentration statistics vs y/δ at $x/\delta = 0.625$, $z/\delta = z_s/\delta$.

ment between the transversal experimental and modelled results is good (see Figs 4.13a, 4.13b, 4.13c, 4.13d) as well as the vertical profile of C in Fig. 4.14a. On the contrary, the model is less efficient in predicting the vertical profiles of σ_c, m_3^* and m_4^* (Figs. 4.14b, 4.14c, 4.14d), since the modelled profiles are shifted with respect to the experimental ones. We believe that the reason of these discrepancies should be found in the model formulation: when the plume touches the ground, the hypothesis of indepencency of the horizontal and vertical pdfs (p_{yr} and p_{zr}) is not suited to describe the anisotropy and inhomogeneity of the concentration fluctuations.

Ground level source

The influence of the velocity shear on the source located at $z/\delta = 0.06$ (GLS) is larger compared to that at $z/\delta = 0.19$ (ES) and the inhomogeneity of the turbulent flow significantly affects the plume dispersion; an evident effect of the source height on the dynamics is the different shape of the intensity of relative concentration fluctuations in the two cases (Fig. 4.8).

The modelled profiles of the first fourth moments of the concentration along x-coordinate, evaluated at the source location (Fig. 4.15), presents a fairly good agreement with the experimental data both close to the source and in the far-

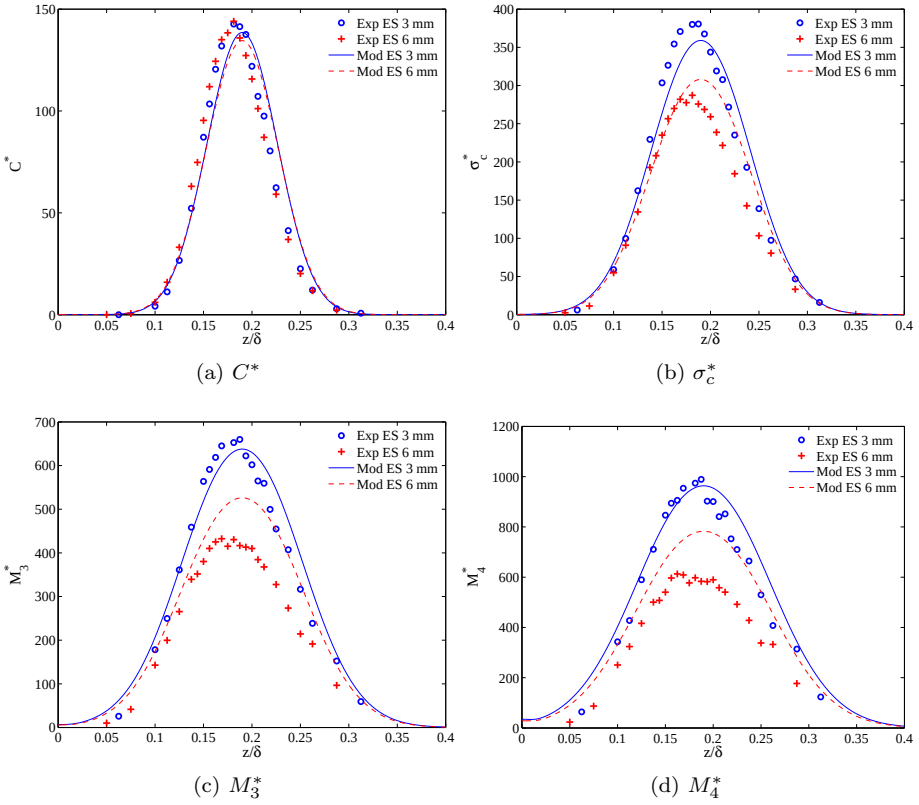

(a) C^* (b) σ_c^*

(c) M_3^* (d) M_4^*

Figure 4.12: Concentration statistics vs z/δ at $x/\delta = 0.625$, $y/\delta = y_s/\delta$.

field. The horizontal profiles of the concentration moments are in very good agreement within the whole field (Figs. 4.16 and 4.18). The ability of the model to reproduce the emergence of off-centreline peaks is quite remarkable . The vertical profiles show a good agreement with the experimental data, except close to the ground where the overestimation of the meandering process determines some discrepancies (Fig. 4.17). The significant difference shown by the vertical profile in the far-field (Fig. 4.20) constitutes a shortcoming of the model that will be discussed in the next subsection.

Asymptotic behaviour

In the far field ($x/\delta \to \infty$) the meandering process becomes negligible and the relative concentration fluctuation i_{cr} approaches i_c (Figure 4.9):

$$i_{cr} \to i_c \tag{4.34}$$

$$\sigma_{zm} \to 0 \tag{4.35}$$

$$\sigma_{zr} \to \sigma_z \tag{4.36}$$

In these conditions, the centroid PDF p_m approaches a Dirac delta function and the PDF of the global dispersion (p_c) is totally described by the relative

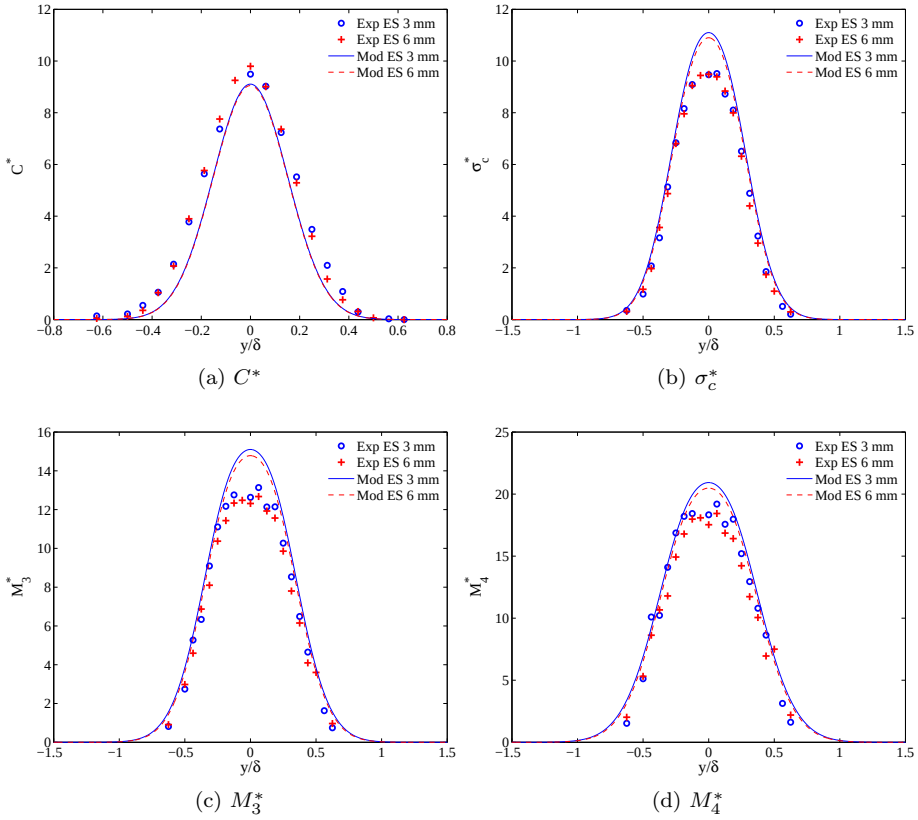

(a) C^* (b) σ_c^*

(c) M_3^* (d) M_4^*

Figure 4.13: Concentration statistics vs y/δ at $x/\delta = 3.75$, $z/\delta = z_s/\delta$.

concentration PDF, that assumes the following formulation:

$$p_m \rightarrow \delta_D \tag{4.37}$$

$$p_c = \frac{\lambda^\lambda}{\Gamma(C\lambda)} \left(\frac{c}{C}\right)^{\lambda-1} \exp\left(-\frac{\lambda c}{C}\right) \tag{4.38}$$

The use of a Γ distribution to describe the concentration PDF of a fluctuating plume is in agreement with the works of many authors (Villermaux and Duplat (2003); Yee and Skvortsov (2011)).

Now the n-th concentration moment assumes this form:

$$\overline{c^n}(x,y,z) = \left(\frac{M_q}{2\pi\sigma_y\sigma_z\overline{u}}\right)^n \frac{1}{\lambda^n}\frac{\Gamma(n+\lambda)}{\Gamma(\lambda)} \exp\left[-\frac{n(y-y_s)^2}{2\sigma_y^2}\right] \tag{4.39}$$
$$\exp\left(-\frac{n(z+z_s)^2}{2\sigma_z^2}\right)\left(\exp\left(\frac{2zz_s}{\sigma_z^2}\right)+1\right)^n.$$

After some algebra we obtain the following relation between the first two moments of concentration:

$$\overline{c^2}(x,y,z) = \frac{\lambda+1}{\lambda} C^2(x,y,z) \tag{4.40}$$

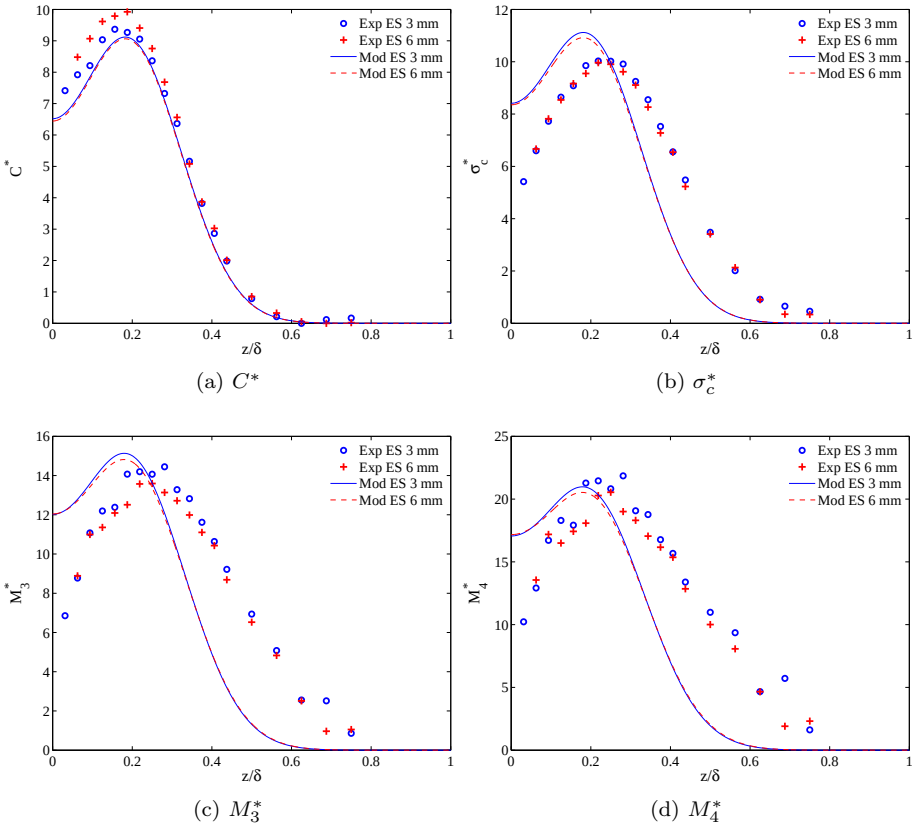

(a) C^* (b) σ_c^*

(c) M_3^* (d) M_4^*

Figure 4.14: Concentration statistics vs z/δ at $x/\delta = 3.75$, $y/\delta = y_s/\delta$.

The constant ratio between the variance and the mean concentration represents a heavy simplification of the model that provides unrealistic results in the far field. We can recognise this effect in the GLS vertical profiles, where the agreement between the model and experiments is quite unsatisfactory (see Fig. 4.20).

Taking advantage of the self-similarity of i_c in the far field (see Section 3.5.2) we can approximate its dependence on z by the following parametrisation:

$$i_{cr} = i_c = a \exp\left(b\frac{z}{\sigma_z}\right); \tag{4.41}$$

where $a = 0.2736$ and $b = 0.8653$. Figures 4.20 shows that the vertical profiles of the fourth moments of the concentration evaluated by taking into account the dependence of i_c on z present a better agreement with the experimental values.

Concentration probability density functions

The model provides a concentration PDF that is given by Equation 4.1. The modelled and experimental PDFs are compared in Figs. 4.21, at growing distances from the source. We also reported the PDF described by a Γ distribution Yee and Skvortsov (2011) depending on the experimental concentration

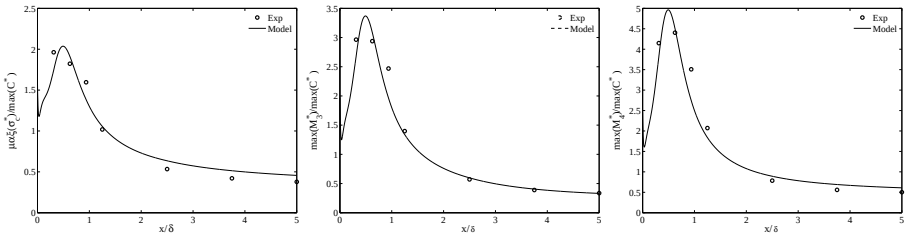

(a) σ_c^*/C^* (b) M_3^*/C^* (c) M_4^*/C^*

Figure 4.15: Concentration statistics vs x/δ evaluated at the source location $(y_s/\delta, z_s/\delta)$.

fluctuation intensity $(\sigma_c/C)_{exp}$. Close to the source the meandering mechanism prevails (see Fig. 4.6) and, as consequence, we have high probability that the concentration assumes values equal to zero (Figs. 4.21a). In the far-field, the PDF of the plume centroid approaches a Dirac delta distribution and the meandering becomes negligible with respect to the relative dispersion; these effects are well reproduced by the PDFs in Fig. 4.21b.

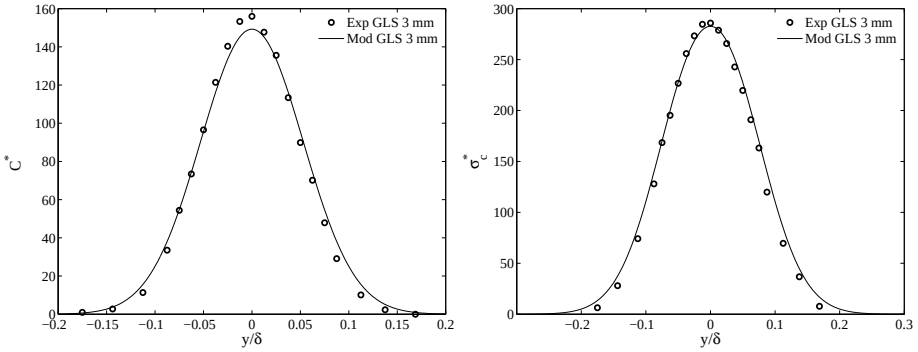

(a) C^* (b) σ_c^*

(c) M_3^* (d) M_4^*

Figure 4.16: Concentration statistics vs y/δ at $x/\delta = 0.625$, $z/\delta = z_s/\delta$.

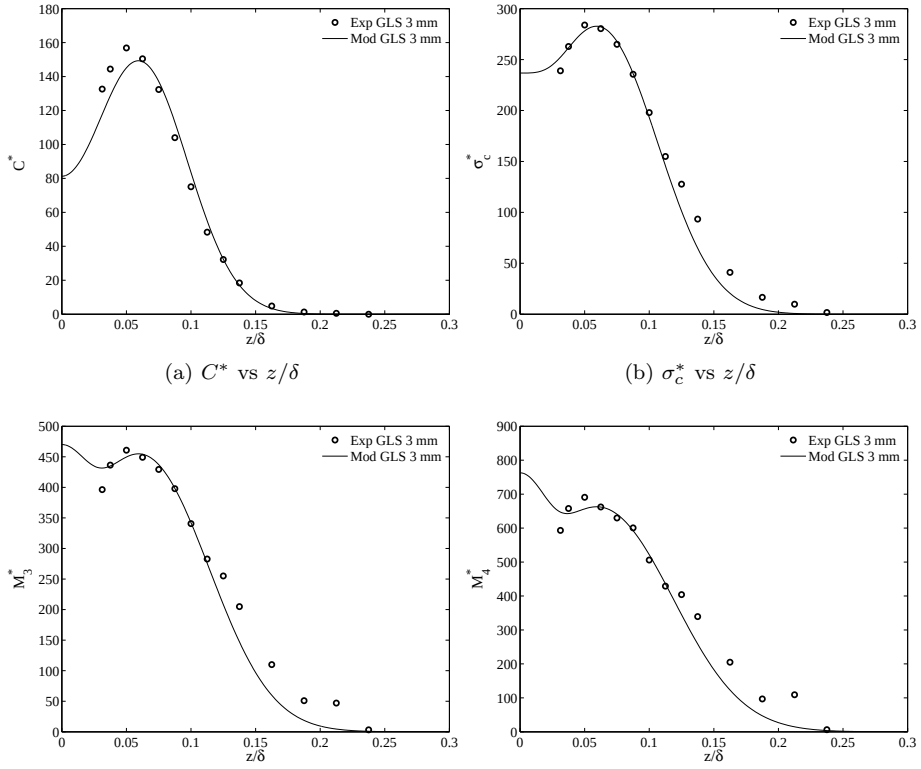

(a) C^* vs z/δ

(b) σ_c^* vs z/δ

(c) M_3^* vs z/δ

(d) M_4^* vs z/δ

Figure 4.17: Concentration statistics vs z/δ at $x/\delta = 0.625$, $y/\delta = y_s/\delta$.

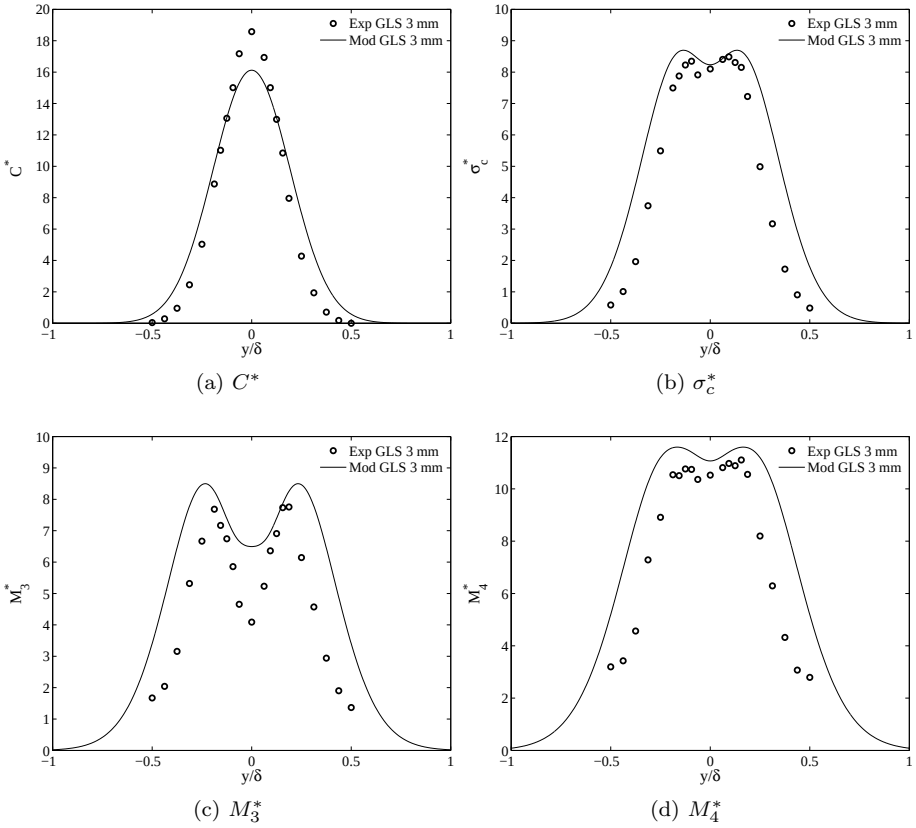

(a) C^* (b) σ_c^*

(c) M_3^* (d) M_4^*

Figure 4.18: Concentration statistics vs y/δ at $x/\delta = 3.75$, $z/\delta = z_s/\delta$.

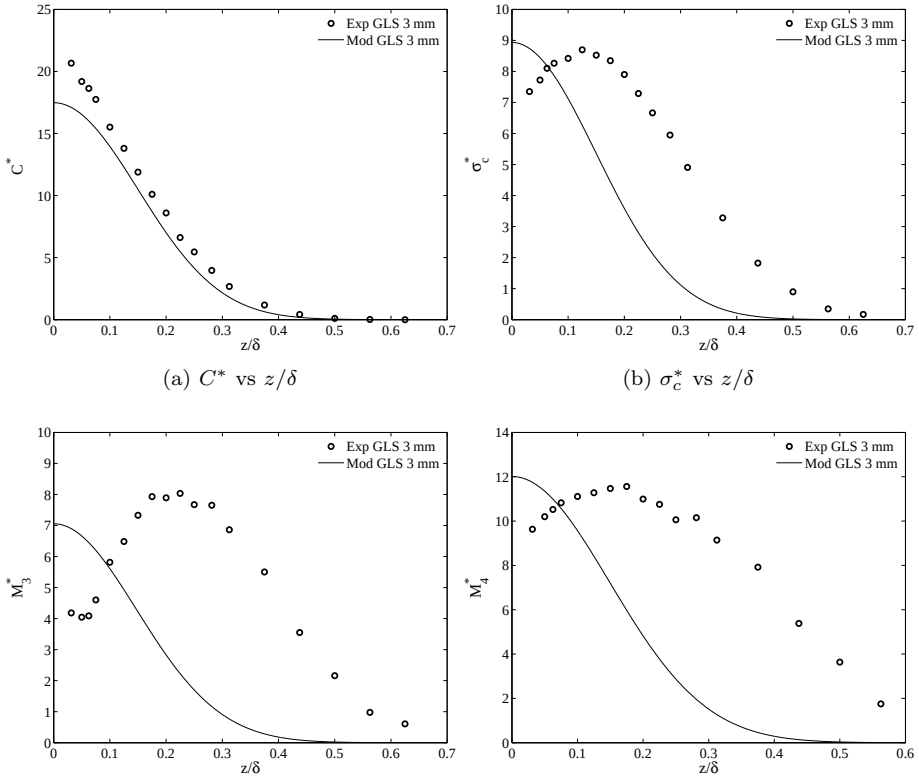

(a) C^* vs z/δ

(b) σ_c^* vs z/δ

(c) M_3^* vs z/δ

(d) M_4^* vs z/δ

Figure 4.19: Concentration statistics vs z/δ at $x/\delta = 3.75$, $y/\delta = y_s/\delta$.

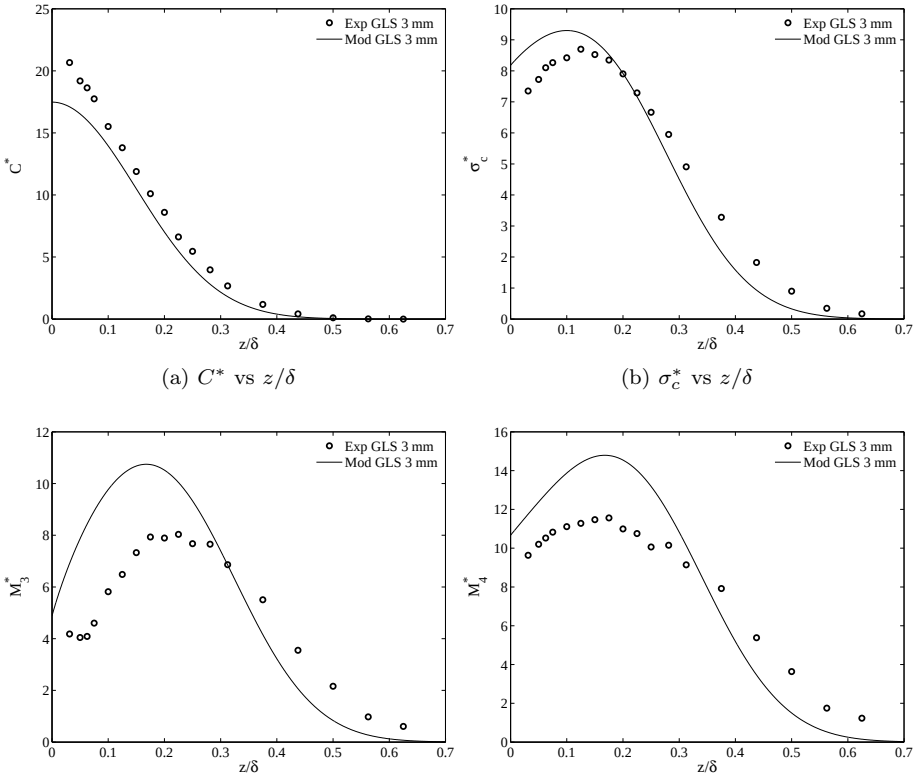

(a) C^* vs z/δ (b) σ_c^* vs z/δ

(c) M_3^* vs z/δ (d) M_4^* vs z/δ

Figure 4.20: Concentration statistics vs z/δ at $x/\delta = 3.75$, $y/\delta = y_s/\delta$ with $i_{cr} = f(z/\sigma_z)$.

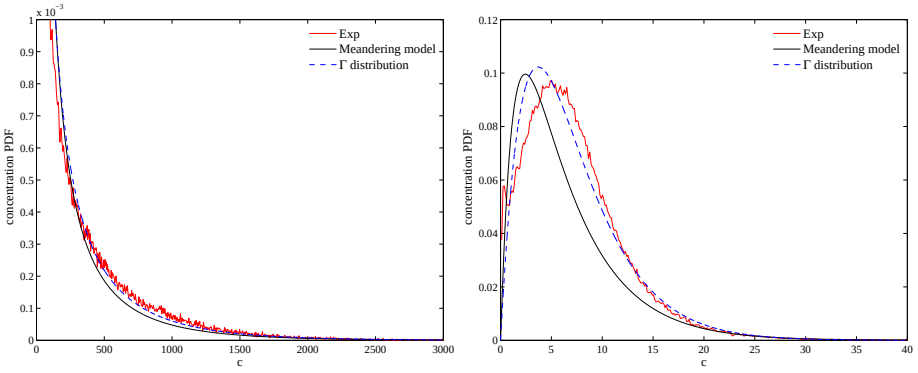

(a) $x/\delta = 0.625$ (b) $x/\delta = 5.0$

Figure 4.21: Experimental and modelled PDF on the mean plume centerline for the case of the elevated source with diameter 3 mm.

Chapter 5

MICROMIXING MODEL

5.1 ABSTRACT

A Lagrangian stochastic micromixing model is used to predict the concentration fluctuations of a continuous release in a neutral boundary layer. Such models are able to estimate the high order statistics of the concentration by simulating the combined effect of turbulent mixing and molecular diffusivity. We present the computational algorithm that implements the Interaction by Exchange with the Conditional Mean (IECM) model and we compare the numerical solutions with the experimental values in order to evaluate the reliability of the model. The influence of the source size on the concentration probability density function (PDF) in the near and far-field is discussed and some shortcomings of the model are pointed out.

5.2 INTRO

A Lagrangian stochastic micromixing model aims in simulating the effects of molecular diffusivity on the pollutant concentration fluctuations. Recent studies have shown that this model is particularly adapted to describe the concentration probability density function (PDF) and to estimate higher order moments. Cassiani et al. (2005a) and Postma et al. (2011a) simulated the dispersion of a point source in the neutral boundary layer and compared the concentration fluctuation intensity with the experimental profiles provided by Fackrell and Robins (1982a). The dispersion in the convective boundary layer (Cassiani et al., 2005b) and in the neutrally stratified canopy flow (Postma et al., 2011b) was also analysed. To our knowledge the first four concentration moments are numerically estimated only in homogeneous turbulence (Sawford, 2004), whereas other authors restrict the analysis to the mean and the standard deviation. Here we evaluate the accuracy of a Lagrangian stochastic micromixing model in estimating the first four concentration moments in a fluctuating plume in neutral boundary layer, taking advantage of the new experimental results presented.

5.3 MODEL EQUATIONS

The governing equations of a Lagrangian Stochastic (LS) method simulate the trajectories of N independent particles representing the real fluid in a statistical sense. We assume that the evolution of the position $\mathbf{X}$ and velocity $\mathbf{U}$ of a fluid element is a continuous Markov process and that the mild regularity condition is verified. Under these assumptions the following equations govern the motion of each particle:

$$dU_i' = a_i(\mathbf{X}, \mathbf{U}', t)dt + b_{ij}(\mathbf{X}, \mathbf{U}', t)d\xi_j, \tag{5.1}$$

$$dX_i = (\langle u_i \rangle + U_i')dt, \tag{5.2}$$

where X_i is the particle position, U_i' is the Lagrangian velocity fluctuation relative to the Eulerian mean velocity $\langle u_i \rangle$, t is the time coordinate, and $d\xi_j$ is an incremental Wiener process (Gardiner, 1983) with zero mean and variance dt. The deterministic acceleration term, a_i, is a function of the turbulent statistics and its simplest three-dimensional solution is given imposing the well-mixed condition (Thomson, 1987). For a fixed temporal instant and a space position, if the particle distribution in the domain is homogeneous, each statistic of the particle velocity has to be equal to the Eulerian velocity statistic. As a consequence, the particles have the same dynamical properties of the fluid. The term a_i is defined by the following equation:

$$a_i = -\frac{U_i'}{T_{Li}} + \frac{1}{2}\frac{\partial \sigma_{ui}^2}{\partial x} + \frac{U_i'}{2\sigma_{ui}^2}\left(\overline{U}_j \frac{\partial \sigma_{ui}^2}{\partial x_j}\right) \qquad \text{with} \qquad i = 1, 2, 3. \tag{5.3}$$

The stochastic diffusive term b_{ij} is defined from the Kolmogorov's hypothesis of self-similarity and local isotropy in the inertial subrange (Pope, 1987):

$$b_{ij} = \delta_{ij}\sqrt{C_0 \varepsilon}, \tag{5.4}$$

where δ_{ij} is the Kroneker delta. We recall that the Lagrangian integral scales T_{Li} represent the autocorrelation Lagrangian velocity coefficients and are expressed as function of the velocity variances σ_{ui}^2, of the turbulent kinetic energy dissipation rate ε and of the Lagrangian Kolmogorov constant C_0:

$$T_{Li} = \frac{2\sigma_{ui}^2}{C_0 \varepsilon}. \tag{5.5}$$

Equations 5.1 and 5.2 only provide information about first-order statistics, namely the mean concentration. The simulation of the higher-order statistics requires the introduction of another Markovian state variable, ϕ, representing the particle concentration. The evolution of the concentration field is simulated by a micromixing model, that takes into account the effects of molecular diffusivity and has to satisfy the following requirements:

1. at large Reynolds number the model do not have to change the mean scalar field
2. concentration fluctuations are dissipated by the model
3. the scalar field has to be bounded, i.e. the concentration keeps positive

4. the scalar PDF tends to a Gaussian for statistically homogeneous scalar fields in homogeneous isotropic turbulence.

Each particle is characterised by a concentration ϕ, whose evolution can be simulated according to the Interaction by Exchange with the Mean (IEM) model or, alternatively, with the Exchange with the Conditional Mean (IECM) model. In this study, we do not consider IEM model since many authors have already shown that it is unable to accurately reproduce the moment properties. In fact, the IEM introduces some spurious fluxes that cause an alteration of the mean concentration field (Cassiani et al., 2007; Sawford, 2004). The IECM model instead allows us to avoid this last effect. This approach reduces the particle interactions to those that have similar position and velocity:

$$\frac{d\phi}{dt} = -\frac{\phi - \langle\phi|\mathbf{X},\mathbf{U}\rangle}{\tau_m}, \tag{5.6}$$

where $\langle\phi|\mathbf{X},\mathbf{U}\rangle$ is the mean scalar concentration conditioned on the local position and velocity. The scalar micromixing time τ_m represents the temporal scale of molecular diffusion.

The analytical solution of Equation 5.6 is:

$$\phi(t+\Delta t) = \phi(t)\exp\left(-\frac{\Delta t}{\tau_m}\right) + \langle\phi|\mathbf{X},\mathbf{U}\rangle\left[1-\exp\left(-\frac{\Delta t}{\tau_m}\right)\right], \tag{5.7}$$

where Δt is the time-step-length.

5.3.1 Micromixing time scale

The parametrisation of the micromixing time scale τ_m follows the formulation proposed by Cassiani et al. (2005a) and is tested in the works of Cassiani et al. (2007) and Postma et al. (2011a).

The micromixing time is assumed to be proportional to the time scale of the relative dispersion process (τ_r) depending on velocity variance, mean turbulent kinetic energy dissipation rate, source size and particle flight time. τ_m can be written as:

$$\tau_m = \mu_t \tau_r, \tag{5.8}$$

where μ_t is an empirical constant depending on the turbulence and on the source configuration, treated as a free parameter. The parametrization of τ_r depends on the instantaneous plume spread σ_r and on the root mean square of the relative fluctuations σ_{ur}, that represents the energy responsible for the expansion of the plume about its instantaneous centre of mass:

$$\tau_r = \sigma_r/\sigma_{ur}. \tag{5.9}$$

Following Franzese's formulation (Franzese, 2003), σ_{ur} is modelled considering the variance of the turbulent velocity $\sigma_u^2 = \sum\sigma_{ui}^2/3 = 2q^2/3$ and the length scale of the most energetic eddies L:

$$\sigma_{ur}^2 = \sigma_u^2\left(\frac{\sigma_r}{L}\right)^{2/3}, \tag{5.10}$$

$$L = \frac{\left(3\sigma_u^2/2\right)^{3/2}}{\varepsilon}. \tag{5.11}$$

When the instantaneous plume spread σ_r becomes equal to the size of the largest eddies L, all the energy contributes to the plume expansion and for $\sigma_r > L$ the constraint $\sigma_{ur}^2 = \sigma_u^2$ is imposed.

The instantaneous plume spread is modelled as:

$$\sigma_r^2 = \frac{d_r^2}{1 + (d_r^2 - \sigma_0^2)/(\sigma_0^2 + 2\sigma_u^2 T_L t)}, \tag{5.12}$$

where $T_L = 2\sigma_u^2/(C_0\varepsilon)$ is the Lagrangian time scale averaged on the three space coordinates. The root-mean square two-particle separation in the instantaneous plume, d_r, is parametrised by Richardson's law:

$$d_r = C_r\varepsilon(t + t_s)^3, \tag{5.13}$$

where C_r is the Richardson-Obukhov constant, $t_s = \left[\sigma_0^2/(C_r\varepsilon)^{1/3}\right]$ is the inertial range formulation for dispersion from a finite source size (Franzese, 2003) and σ_0 represents the initial source distribution . The discretization of d_r is commonly obtained by linearization:

$$d_r^2(t + \Delta t) = d_r^2(t) + 3C_r\varepsilon(t + t_0)^2\Delta t, \tag{5.14}$$

with the initial condition $d_r^2(t = 0) = \sigma_0^2$. The upper bound of the micromixing time is the turbulence time scale $2q^2/(C_\phi\varepsilon)$ where q^2 is the turbulent kinetic energy and C_ϕ is an empirical constant set equal to 2.

5.3.2 Description of SLAM model

The coupling between the Lagrangian stochastic model (Equations 5.1 and 5.2) and the micromixing model (5.6) is performed by the numerical code SLAM, Safety Lagrangian Atmospheric Model (Vendel et al., 2011). SLAM is a model developped in the team AIR (Atmosphere Impact Risk) of the Laboratoire de Mécanique des Fluides et d'Acoustique de l'Ecole Centrale de Lyon, France.

The micromixing time and conditional mean concentrations are estimated during a pre-processing step. The trajectories of a small ensemble of particles released at the source location are computed and the cell-centered averages of τ_m and $\langle\phi|\mathbf{X}, \mathbf{U}\rangle$ are evaluated at all the space discretization elements of a suitable computational grid. Afterwards, the effects due to the molecular diffusivity on the concentration fluctuations are taken into account by simulating the influence of the background particles. This strategy allows us to obtain a multitude of concentration values and, therefore, suitably approximate the concentration PDFs.

The numerical experiments follow the approach of Cassiani et al. (2007): at the initial time-step a set of particles is uniformly distributed in the whole computational domain and each particle moves in accordance with the Equations 5.1 and 5.2. During this process, the concentration associated to each particle changes (Equation 5.6) assuming a large variety of values that allows us to compute the high order statistics. In order to increase the solution accuracy, the concentration is averaged on the simulation time. A suitable choice of the boundary conditions allows us to correctly reproduce the dispersion of the passive scalar and keep constant the number of particles during the simulations:

- top and lateral boundaries: the particle velocity and position are perfectly reflected and the concentration is absorbed;

- ground: particles are elastically reflected and conserve their concentration;

- inflow/outflow: periodic conditions are applied to the particle position and the absorption of the concentration is imposed;

- source: the influence of the source is taken into account by marking the near-source particles with a scalar concentration ϕ_{src}:

$$\phi_{src} = \frac{M_q}{2\pi\sigma_0^2 \overline{u_x}} \exp\left(-\frac{r^2}{2\sigma_0^2}\right), \tag{5.15}$$

  where M_q is the source mass-flow, $\overline{u_x}$ is the horizontal mean velocity at the source location (x_s, y_s, z_s) and $r^2 = (y-y_s)^2 + (z-z_s)^2$ is the distance from the particle position to the source in the yz-plane.

The computational algorithm is made of the following steps:

1. Pre-processing: simulation of the trajectories of an ensemble of particles released at the source location (Eqs. 5.1 and 5.2);

   - Simulation of the trajectories of an ensemble of particles released at the source location;
   - Estimate of the conditional mean concentration $\langle\phi|\mathbf{X}, \mathbf{U}\rangle$ and micromixing time τ_m;

2. Simulation of the concentration fluctuations (Eqs. 5.1, 5.2 and 5.6);

   - Instantaneous release of a uniform particle distribution in the whole domain
   - Initialization of particle properties ($\mathbf{X}$, $\mathbf{U}$, ϕ);
   - Main time loop:
     - Loop on all particles:
       * Update particle velocity and position
       * Apply boundary conditions
       * Update particle concentration ϕ
     - Update cell-centered statistics;
   - Update time averaged statistics.

Such micromixing model requires the tuning of some free parameters in order to get a suitable accuracy in the solutions (Postma et al., 2011b): the Kolmogorov constant C_0, that influences the Lagrangian integral scales, the Richardson constant C_r and the micro-mixing constant μ_t, that affects the micromixing time scale, and the initial source distribution σ_0, that linearly depends on the source diameter d_s. It is worth noting that this approach requires a large amount of computational resources due to the elevated number of particles.

5.4 NUMERICAL EXPERIMENTS

The ability of the Lagrangian stochastic micromixing model SLAM to estimate the concentration fluctuations was investigated. In the numerical experiments we simulated the dispersion of a fluctuating plume produced by a continuous release from a point source in the neutral boundary layer and we compared the numerical results with the experimental measurements that we performed in wind tunnel.

5.4.1 Computational set-up

The numerical experiments concerned a preliminary study of the influence of the discretization parameters. We carried out some simulations on a uniform grid, varying the cell dimensions and the time-step length, and we verified that the solutions are affected by neither the time-step length nor the space discretization (Figure 5.1a). The same analysis was carried out on the influence of the number of velocity classes used in the definition of the conditional mean concentration. Figure 5.1b shows that three classes for each velocity component are sufficient to assure a suitable accuracy. In order to have a satisfactory agreement with the experimental measures, the parameters adopted in the simulations are:

1. $C_0 = 4.5$
2. $\sigma_0 = \sqrt{2/3 d_s}$, d_s being the source diameter
3. $C_r = 0.3$ (Cassiani et al. (2005a))
4. $\mu_t = 0.6$
5. velocity classes: 3 x 3 x 3.

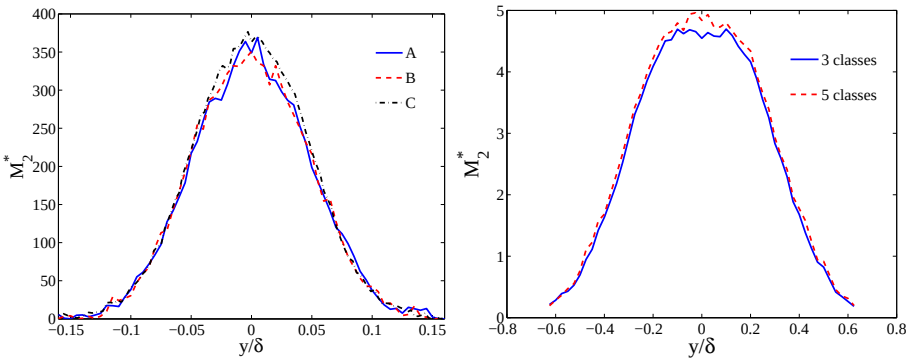

(a) space and time discretisation (b) velocity classes

Figure 5.1: Non-dimensional concentration standard deviation M_2^* vs. y/δ at the source height. (a): $x/\delta = 0.625$, (A) $\Delta t = 1.0e-3$, $\Delta x = 0.02$, $\Delta y = \Delta z = 5.0e-3$; (B) $\Delta t = 5.0e-4$, $\Delta x = 0.02$, $\Delta y = \Delta z = 5.0e-3$; (C) $\Delta t = 1.0e-3$, $\Delta x = 0.01$, $\Delta y = \Delta z = 3.0e-3$; (b) $x/\delta = 5.0$.

5.4.2 Results

Experimental measurements show that the source size does not affect the mean concentration, whereas it influences higher order moments. This influence is significant in the near-field (Figures 5.2 and 5.3) and it gradually becomes negligible for increasing distances from the source (Figures 5.4 and 5.5). In order to test the reliability of the model, we computed the first four centred moments of the concentration and we compared them with the corresponding experimental values after a suitable adimensionalisation:

$$m_i^* = \left[\frac{1}{N_c}\sum_{p=1}^{N_c}(C_p - C_c)^i\right]^{1/i}\frac{u_\infty \delta^2}{M_q}, \tag{5.16}$$

where u_∞ is the velocity at the boundary layer height, N_c and C_c are the number of particles and the mean concentration in the cell, respectively, and C_p is the particle concentration. In the near-field (Figures 5.2 and 5.3) the model is able to reproduce the influence of the source size on the concentration fluctuations showing a good agreement with the experimental values. In particular, Figures 5.2b and 5.2d show that the differences in the concentration PDFs due to the source diameter are correctly simulated. In the far-field ($x \sim 500 - 1000 d_s$) the model suitably simulates the negligibility of the source size on the computed standard deviation and the agreement with the experimental values is satisfactory both on vertical and transversal profile (Figures 5.4a and 5.4b and Figures 5.5a and 5.5b). On the contrary, some discrepancies occur on higher order moments: while experimental profiles show that the source size influence vanishes in the far-field, in the numerical solutions such effect is delayed. The numerical solutions overestimate the experimental results and some differences due to the source diameter persist (Figures 5.4c and 5.4d and Figures 5.5c and 5.5d). Indeed the loss of influence of the source size is delayed with respect to the experiments.

Let us define the relative difference between the computed moments for the two source sizes ES 3 mm ($d_s/\delta = 7e-3$) and ES 6 mm ($d_s/\delta = 3.75e-3$) as:

$$D_{rel} = \sqrt{\frac{\int_{-\infty}^{\infty}[(m_i^*)_{ES3mm} - (m_i^*)_{ES6mm}]^2 dy}{\int_{-\infty}^{\infty}[(m_i^*)_{ES3mm}]^2 dy}}. \tag{5.17}$$

We observe that D_{rel} reduces from $x/\delta = 3.75$ and $x/\delta = 5$ (Figure 5.6) as shown in Table 5.1.

x/δ	$D_{rel}\ m_3^*$	$D_{rel}\ m_4^*$
3.75	0.17	0.36
5	0.12	0.29

Table 5.1: Relative difference between the third and fourth moments at different distances x/δ.

The reasons for this delay have to be attributed to the shortcomings of the micromixing model that can be reasonably identified in the approximated formulation of the micromixing time scale and in an incomplete description of

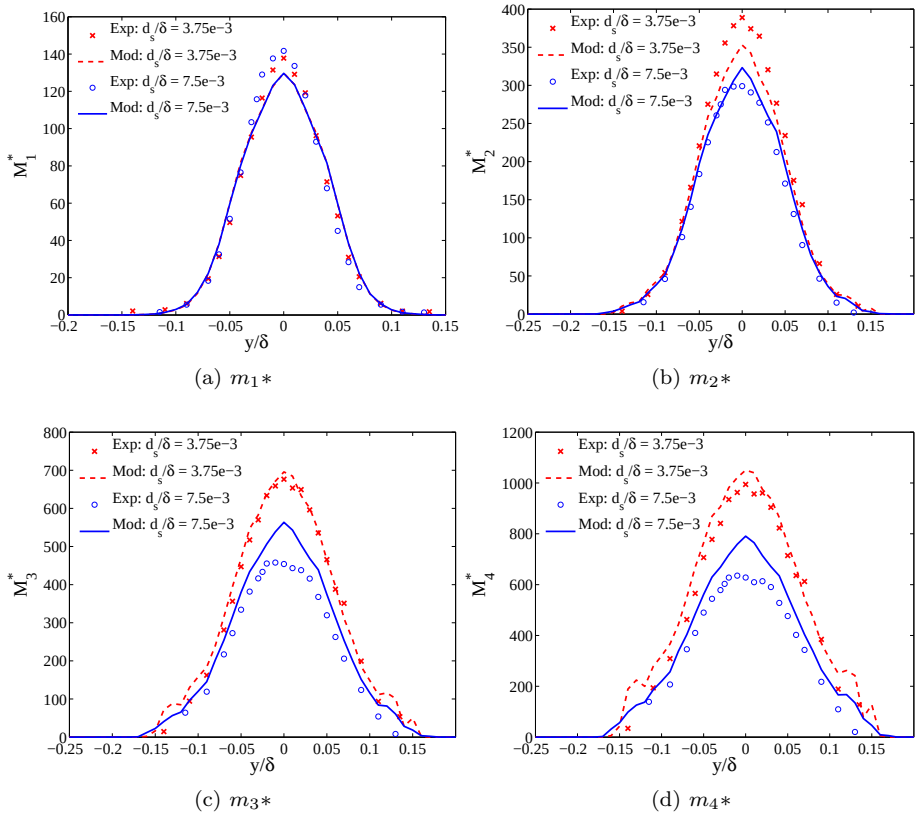

(a) m_1* (b) m_2*

(c) m_3* (d) m_4*

Figure 5.2: Non-dimensional concentration statistics vs. y/δ evaluated at the source height and $x/\delta = 0.625$.

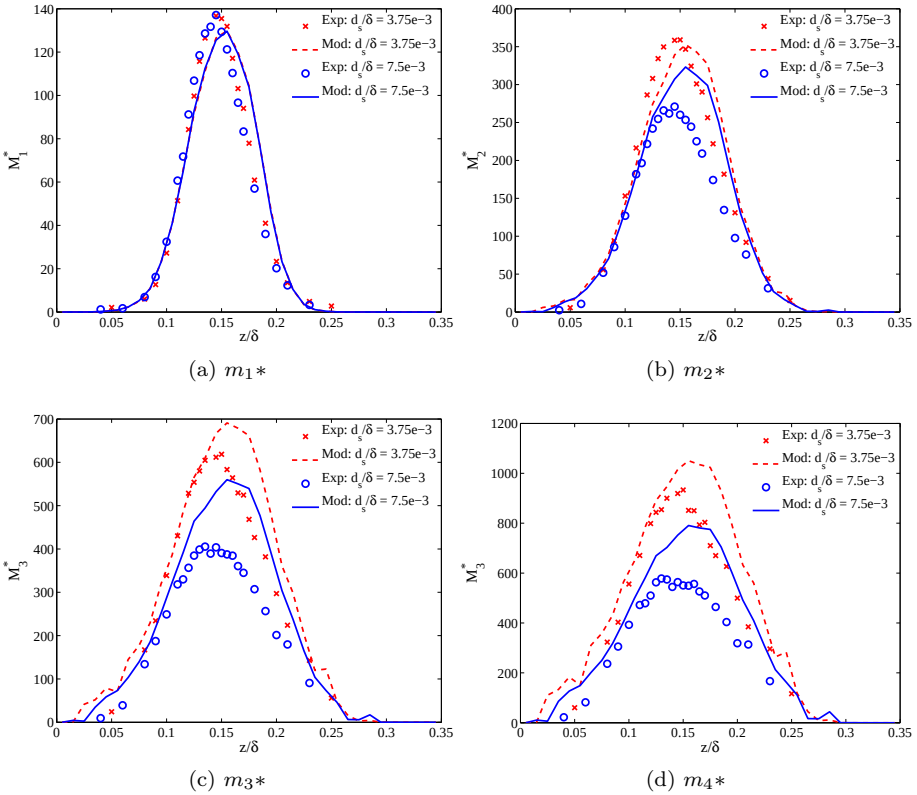

(a) m_1* (b) m_2*

(c) m_3* (d) m_4*

Figure 5.3: Non-dimensional concentration statistics vs. z/δ evaluated at the source height and $x/\delta = 0.625$.

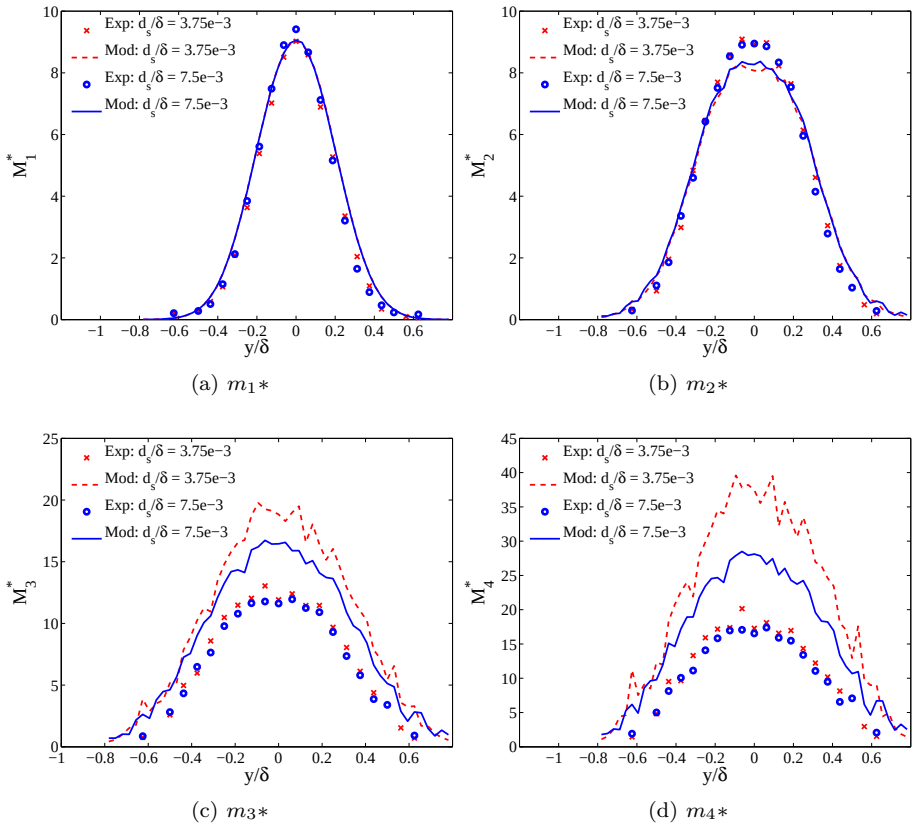

(a) m_1* (b) m_2*

(c) m_3* (d) m_4*

Figure 5.4: Non-dimensional concentration statistics vs. y/δ evaluated at the source height and $x/\delta = 3.75$.

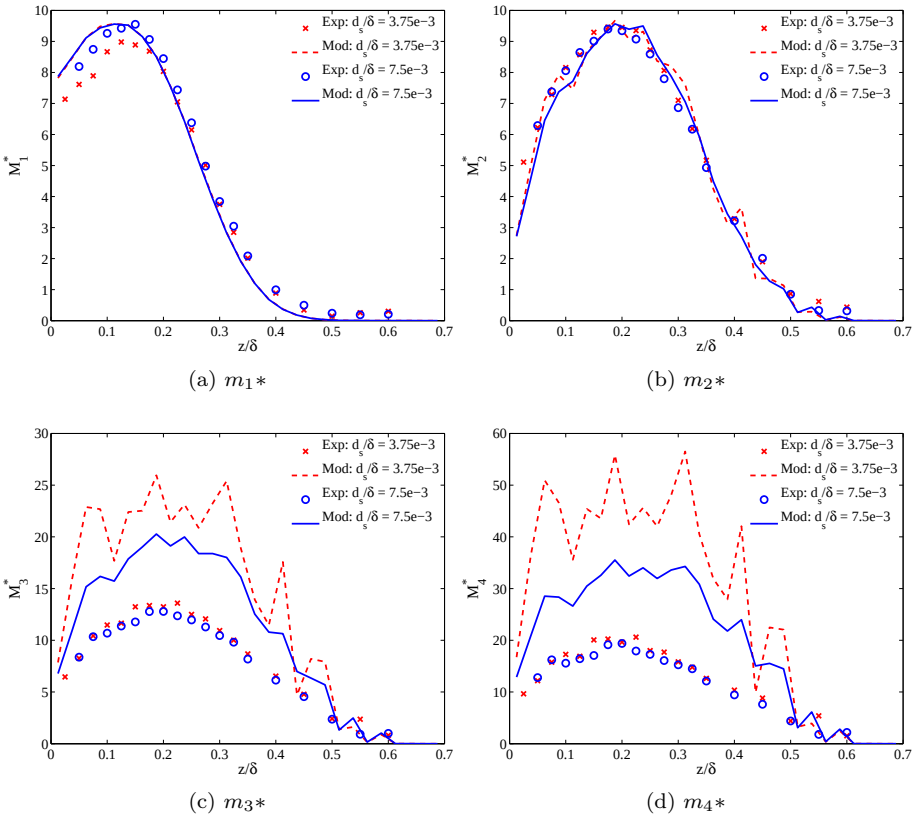

(a) m_1* (b) m_2*

(c) m_3* (d) m_4*

Figure 5.5: Non-dimensional concentration statistics vs. z/δ evaluated at the source height and $x/\delta = 3.75$.

the conditional mean concentration due to an insufficient number of the velocity classes. Further developments are needed in order to improve the accuracy of the solutions. In order to evaluate the accuracy of the model we compute the relative error between experimental and numerical values:

$$ER = \sqrt{\frac{\int_{-\infty}^{\infty} [(m_i^*)_{exp} - (m_i^*)_{mod}]^2 dy}{\int_{-\infty}^{\infty} [(m_i^*)_{exp}]^2 dy}}. \tag{5.18}$$

Figures 5.7 shows the relative error on the transverse profiles of the concentration moments at growing distance from the source location. The relative error of the mean concentration and the standard deviation are bounded in the whole field and for both source sizes. Conversely, the third and fourth concentration moments present a low relative error close to the source, but in the far field the discrepancy between the experiments and the numerical results becomes large.

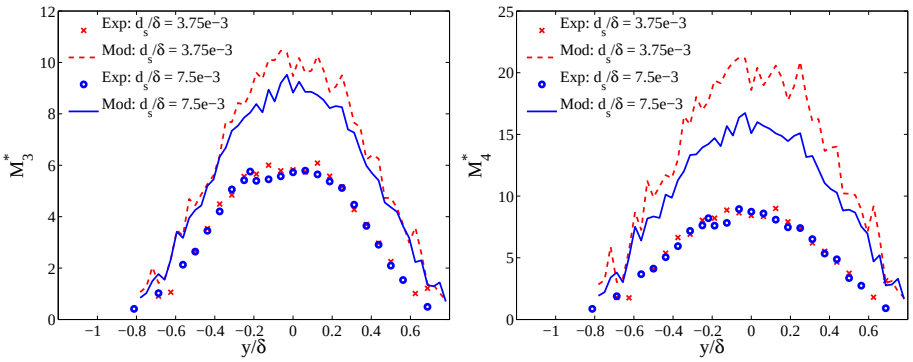

(a) m_3* (b) m_4*

Figure 5.6: Non-dimensional third and fourth moments (m_3^* and m_4^*) of the concentration vs. y/δ evaluated at the source height and $x/\delta = 5$.

The main disadvantage of the micromixing model is the high computational cost. A large number of particles is required to get a suitable accuracy in the numerical solutions, therefore calculations require a large amount of RAM and an elevated CPU time. This limits the applicability of the model to real scale problems in complex geometries.

5.4.3 Conclusions and perspectives

The ability of the Lagrangian stochastic micromixing model SLAM to estimate the concentration fluctuations was investigated. We simulated the dispersion of a fluctuating plume produced by a continuous release from a point source in the neutral boundary layer and we compared the numerical results with a new experimental data set. The numerical solutions show that the model is able to correctly simulate the concentration statistics in the near-field, reproducing the source size effects on the high order moments. In the far-field the numerical and experimental values of the mean and standard deviation of the concentration are in good agreement. Differently the model overestimates the

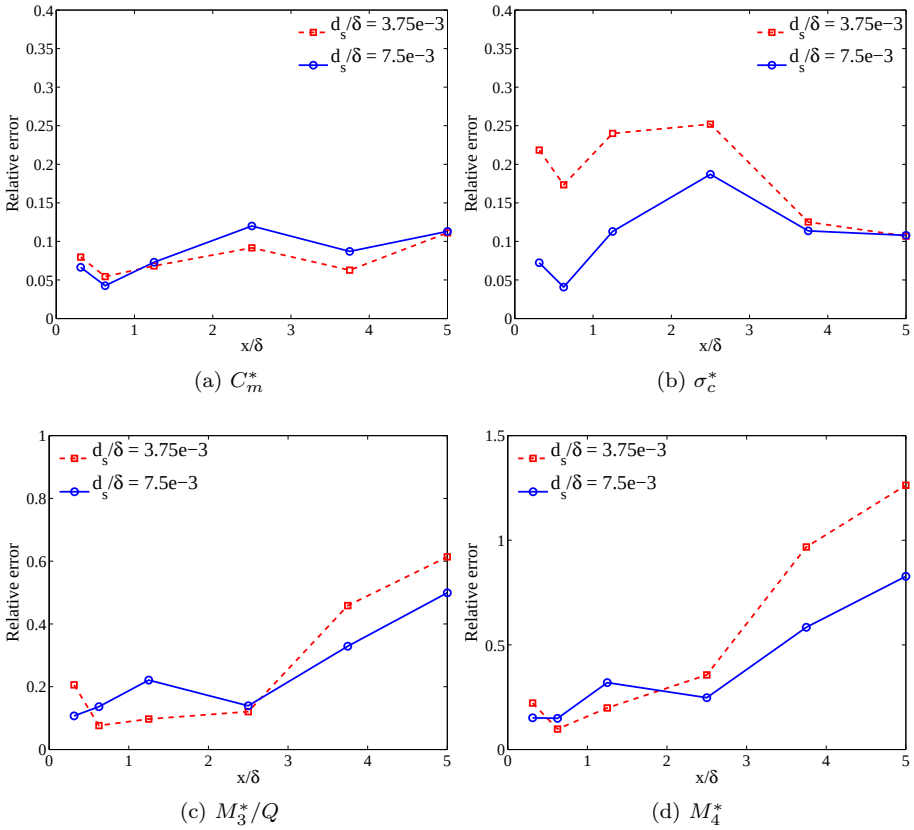

(a) C_m^* (b) σ_c^*

(c) M_3^*/Q (d) M_4^*

Figure 5.7: Transverse profile relative error vs x/δ.

third and fourth moments with respect to the experiments. Moreover, the experimental profiles show that the source size influence vanishes in the far-field after $x \simeq 500 - 1000 d_s$, whereas in the numerical simulations such effect is delayed and it occurs at longer distances. This behaviour shows the shortcomings of the model and the need of further developments in order to improve the accuracy of the solutions. The main shortcoming of such model is the high computational cost. The large number of particles, required to get a suitable accuracy in the numerical solutions, produces a large request of RAM and elevated CPU time that limits the applicability of the model to real scale problems in complex geometries.

Nevertheless further developments are required in order to increase the accuracy for higher concentration moments, namely the third and fourth moment. In particular, a more precise parametrisation of the micromixing time scale should be considered. We can identify three points that are critical in the present formulation of the model and that deserve a deeper analysis:

- the evaluation of the Eulerian length scale (Eq. 5.11) provides a significant overestimation of the real value
- the parametrisation of the instantaneous plume spread (Eq. 5.12) overes-

timates the meandering mechanism in the far-field

- the choice of turbulence time scale $2q^2/(C_\phi\varepsilon)$ as upper boundary of the micromixing time can introduce spurious fluctuations on the plume borders.

Chapter 6

CONCLUSIONS

Several modelling approaches have been developed to satisfy the need of predicting the Probability Density Function (PDF) of the concentration of a passive scalar downwind a source of pollutant within the turbulent boundary layer. This research provided a complete experimental data-set for the validation of dispersion models, where the concentration and the velocity fields are accurately described both spatially and temporally. The data-set was used to test a meandering plume model and a Lagrangian stochastic model.

The velocity field in the TBL over a rough wall was investigated by means of Hot-Wire Anemometry (HWA) and Particle Image Velocimetry (PIV) to provide a detailed analysis of its temporal and spatial structure. We measured velocity statistics, including Reynolds stresses and velocity skewness, two-points correlations, PDFs and spectra. All these statistics are essential in the understanding of the structure of the TBL. By means of comparisons with experiments carried out by other authors, we could verify that we were reproducing the main features of a TBL (i.e. the mean velocity logarithmic profile, the equality between production and dissipation, the Gaussian form of velocity PDFs, the $-5/3$ power law of velocity spectra in the inertial subrange). Thanks to these comparisons we could also point out some of the shortcomings of the similarity theory. In particular, we focused our attention on Eulerian Integral Length Scales (EILS), which provide much information about the structure of our TBL. We could measure vertical profiles of EILS, which were evaluated in x, y and z directions for the three velocity components. The scales were measured with HWA and PIV and the results provided by the two techniques were shown to be in good agreement. From the analysis of the integral lenght scales emerges the great complexity of the velocity field. There exist a great variety of length scales in our boundary layer and only one of them, i. e. $L_{ww}(z)$, scales with z according to the statement of the similarity theory. Lagrangian time scales are key parameters of the flow governing the dispersion mechanisms. We estimated their value by means of two different parametrisations usually adopted in the literature, and verified that the two parametrisations are consistent one to the other for a value of the Kolmogorov constant C_0 equal to 4.5.

A detailed description of the temporal and spatial evolution of a fluctuating plume emitted from a point source was provided. The source was placed within the turbulent boundary layer and the emission was neutrally buoyant and passive. Concentration measurements were carried out using a fast flame ionisa-

tion detector. The experimental protocol and the calibration procedure adopted were described to make clear how we faced some of the problems that appear when dealing with highly intermittent signals. We also discussed the influence of atmospheric aerosol sampling, the seasonal variation of atmospheric aerosol and how their sampling can enable the measurement of third and fourth concentration moments. From the concentration signals recorded, we could calculate concentration PDFs and moments up to the fourth order with a good precision. A data set was created that includes profiles of concentration statistics at growing distances from the source, in the vertical and transversal directions. We also measured spectra, intermittency factor, intensity of concentration fluctuations, concentration variance dissipation and peak values.

We discussed the influence of the source on the dispersion by considering three main aspects: the source elevation, the source size and the gas emission velocity. To carry out this analysis we adopted the framework developed by Gifford (1959), who considers the dispersion of a plume to be produced by two contributions, the meandering motion of the centre of mass and the relative dispersion, and we interpreted these phenomena in the light of the relation between the scales of the plume and those of the velocity field. Source elevation and size have a strong influence on concentration statistics, as already demonstrated by Fackrell and Robins (1982a). We extended their analysis to third and fourth concentration moments. We observed that an emission velocity that is isokinetic with the external flow do not minimise the effect of the source in the dispersion process, and that even sources that are normally considered as point source (having a ratio d/δ close to zero) generate a wake that interacts with the pollutant dispersion in the near field. At last, we showed that the moments of concentration and the PDFs can be effectively reproduced by a Gamma distribution, which also reproduces the differences due to the source size and elevation.

Two modelling approaches have been adopted to interpret the experimental results: a meandering plume model and a Lagrangian stochastic model with a micromixing scheme. A simple two-dimensional meandering plume model is used to study the evolution of the model parameters in transversal and streamwise directions, for the three source configurations. Subsequently, a three dimensional model is proposed to reproduce the inhomogeneity and anisotropy of the dispersion within a turbulent boundary layer, with a new parametrisation for the intensity of relative fluctuations. To account for the presence of the ground, the PDF of the vertical displacement of the centre of mass is assumed to be a Gaussian distribution with reflection on the wall. The comparison with the experiments is satisfactory, even if the model is less efficient in reproducing the vertical profiles of the concentration statistics. We believe that this is due to the hypothesis of indepencency of the horizontal and vertical PDFs, which becomes too hazardous when the plume strongly interacts with the ground.

Finally we used a micromixing Lagrangian stochastic model to evaluate high order statistics of the concentration field. The model reproduces the features of the concentration field and the differences in the statistics profiles due to the source size. In this study, for the first time, this modelling approach was adopted to predict the spatial distribution of third and fourth moments of concentration within an inhomogeneous and anisotropic turbulent flow. The present model formulation, however, shows some difficulties in correctly reproduce the decay of third and fourth moments in the far field.

Chapter 7

Annexes

7.1 Vertical profiles of concentration statistics

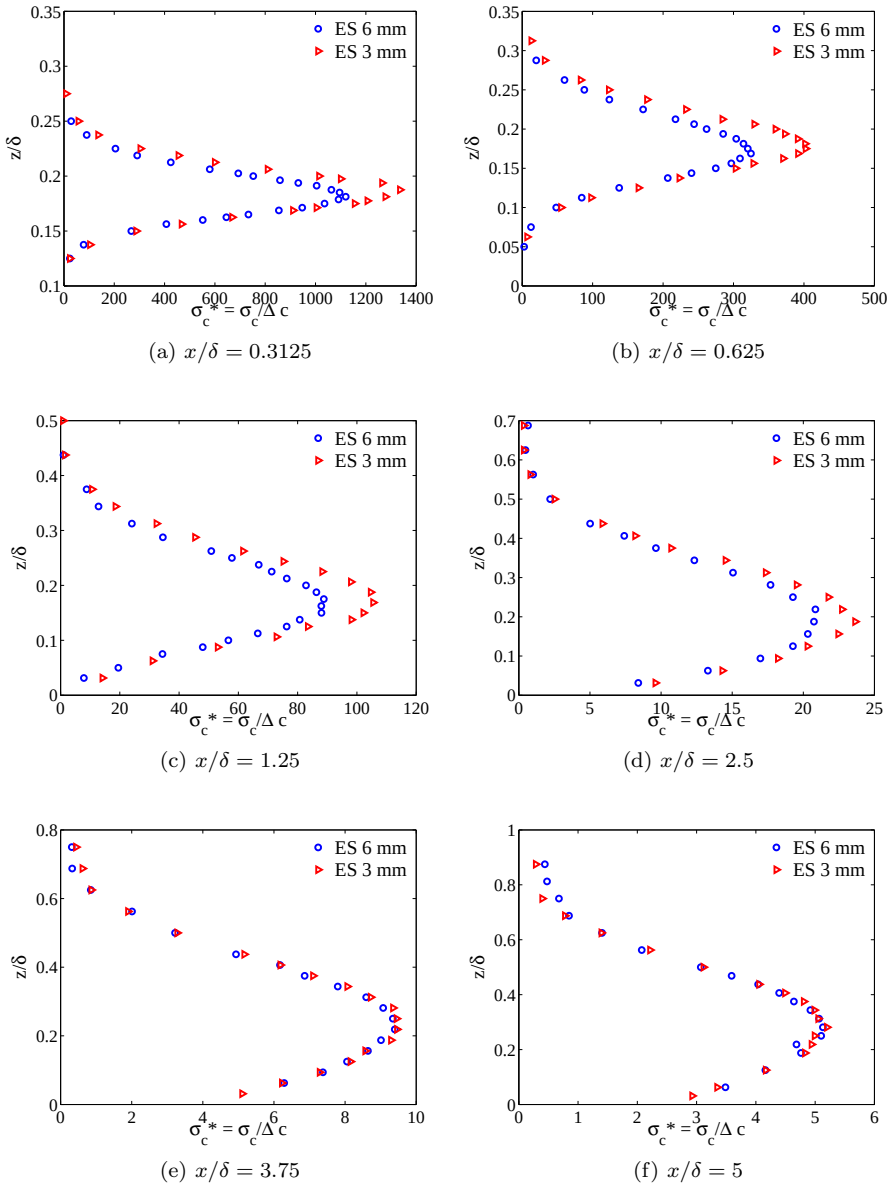

(a) $x/\delta = 0.3125$

(b) $x/\delta = 0.625$

(c) $x/\delta = 1.25$

(d) $x/\delta = 2.5$

(e) $x/\delta = 3.75$

(f) $x/\delta = 5$

Figure 7.1: Vertical profiles of non-dimensional concentration standard deviation for the elevate sources, at various distances downwind. Profiles were measured on the plume axis. Blue circles: source diameter 6 mm; red triangles: source diameter 3 mm.

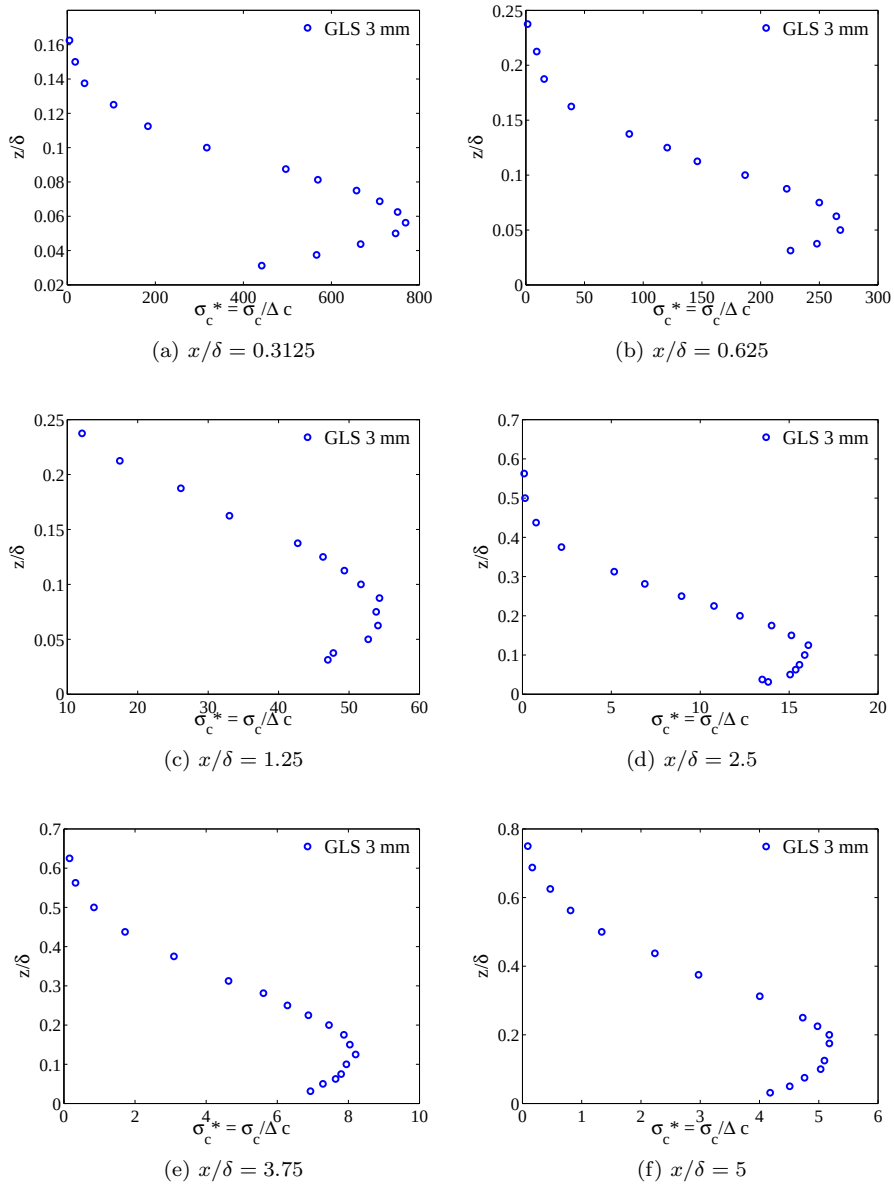

(a) $x/\delta = 0.3125$ (b) $x/\delta = 0.625$

(c) $x/\delta = 1.25$ (d) $x/\delta = 2.5$

(e) $x/\delta = 3.75$ (f) $x/\delta = 5$

Figure 7.2: Vertical profiles of non-dimensional concentration standard deviation for the ground level source, at various distances downwind. Profiles were measured on the plume axis. The source diameter is equal to 3 mm.

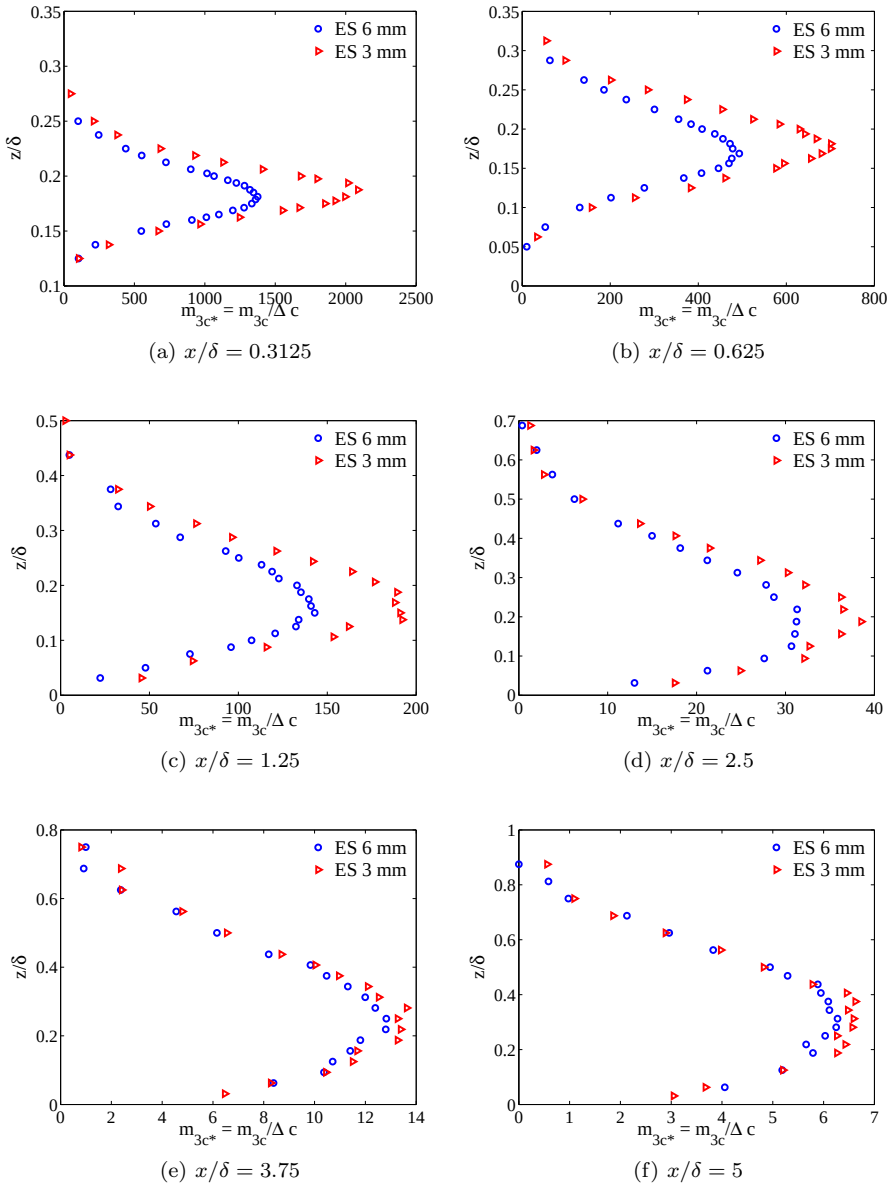

(a) $x/\delta = 0.3125$ (b) $x/\delta = 0.625$

(c) $x/\delta = 1.25$ (d) $x/\delta = 2.5$

(e) $x/\delta = 3.75$ (f) $x/\delta = 5$

Figure 7.3: Vertical profiles of non-dimensional third moment of concentration. Elevated sources at various distances downwind. Profiles were measured on the plume axis. Blue circles: source diameter 6 mm; red triangles: source diameter 3 mm.

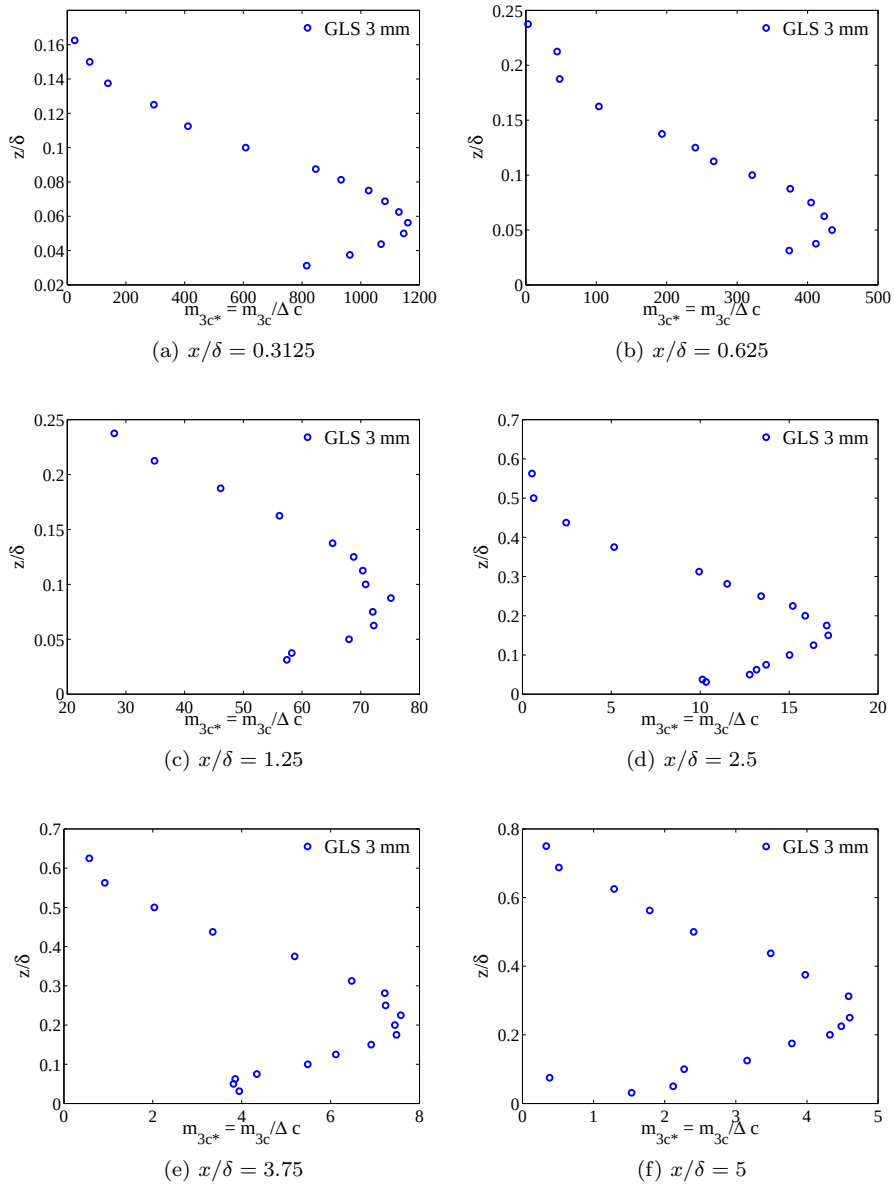

(a) $x/\delta = 0.3125$ (b) $x/\delta = 0.625$

(c) $x/\delta = 1.25$ (d) $x/\delta = 2.5$

(e) $x/\delta = 3.75$ (f) $x/\delta = 5$

Figure 7.4: Vertical profiles of non-dimensional third moment of concentration for the ground level source, at various distances downwind. Profiles were measured on the plume axis. The source diameter is equal to 3 mm.

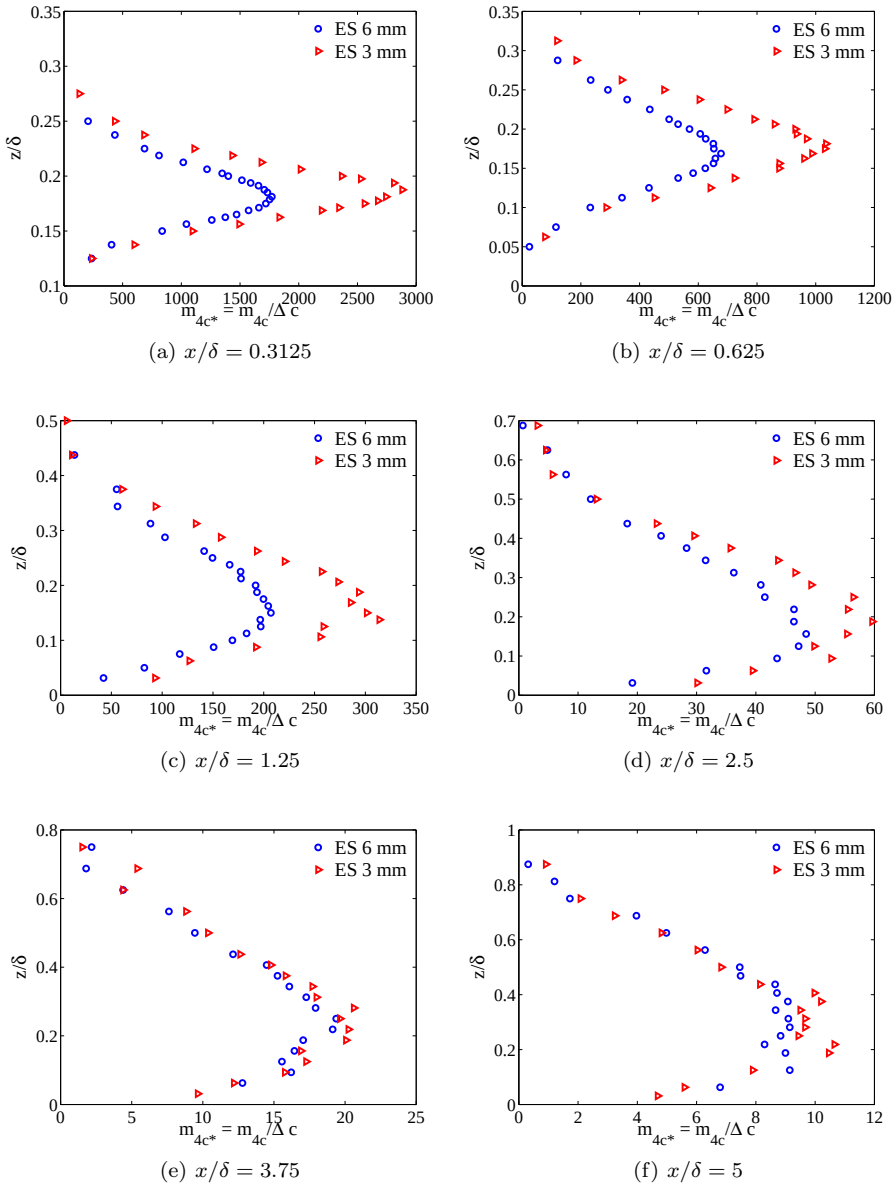

(a) $x/\delta = 0.3125$ (b) $x/\delta = 0.625$

(c) $x/\delta = 1.25$ (d) $x/\delta = 2.5$

(e) $x/\delta = 3.75$ (f) $x/\delta = 5$

Figure 7.5: Vertical profiles of non-dimensional fourth moment of concentration. Elevated sources at various distances downwind. Profiles were measured on the plume axis. Blue circles: source diameter 6 mm; red triangles: source diameter 3 mm.

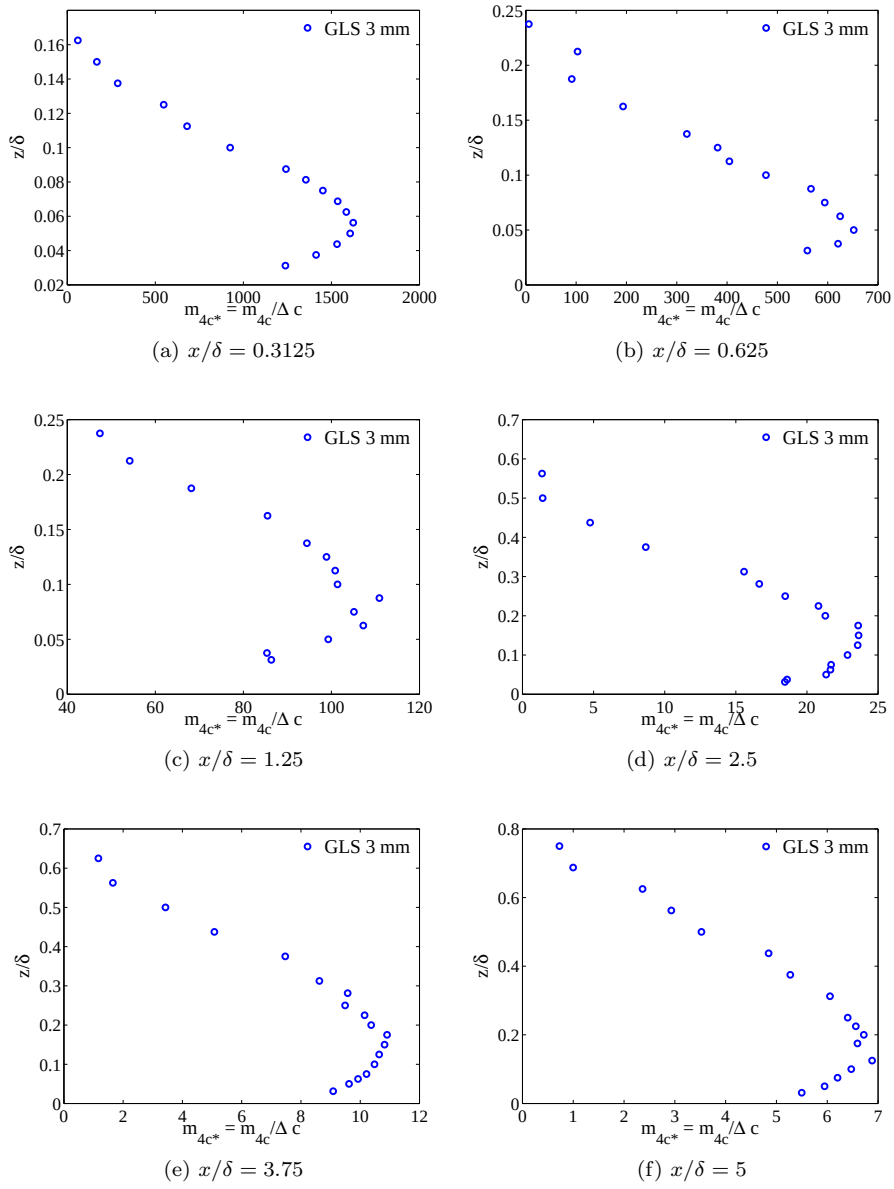

(a) $x/\delta = 0.3125$ (b) $x/\delta = 0.625$

(c) $x/\delta = 1.25$ (d) $x/\delta = 2.5$

(e) $x/\delta = 3.75$ (f) $x/\delta = 5$

Figure 7.6: Vertical profiles of non-dimensional fourt moment of concentration for the ground level source, at various distances downwind. Profiles were measured on the plume axis. The source diameter is equal to 3 mm.

Bibliography

R. Antonia, D. K. Bisset, and L. W. B. Browne. Effects of reynolds number on the organised motion in a turbulent boundary layer. *Journal Fluid Mechanics*, 213:267–286, 1990.

S. Baldi and M. Yianneskis. On the quantification of energy dissipation in the impeller stream of a stirred vessel from fluctuating velocity gradient measurements. *Chemical Engineering Science*, 59:2659–2671, 2004.

S. Baldi, A. Ducci, and M. Yianneskis. Determination of dissipation rate in stirred vessels through direct measurement of fluctuating velocity gradients. *Chemical Engineering Technology*, 27:275–281, 2004.

G. Bergametti, A. L. Dutot, P. Buat-Mnard, R. Losno, and E. Remoudaki. Seasonal variability of the elemental composition of atmospheric aerosol particles over the northwestern mediterranean. *Tellus*, 41B:353–361, 1989.

G. P. Bewley, K. Chang, and E. Bodenschatz. On integral length scales in anisotropic turbulence. *Physics of Fluids*, 24:061702, 2012.

H. H. Bruun. *Hot-wire anemometry. Principles and signal analysis*. Oxford Science Publications, 1995.

P. Carlotti and P. Drobinski. Length scales in wall-bounded high-reynolds-number turbulence. *Journal Fluid Mechanics*, 516:239–264, 2004.

M. Cassiani, P. Franzese, and Giostra U. A pdf micromixing model of dispersion for atmospheric flow. part i: development of the model, application to homogeneous turbulence and neutral boundary layer. *Atmospheric Environment*, 39:1457–1469, 2005a.

M. Cassiani, P. Franzese, and Giostra U. A pdf micromixing model of dispersion for atmospheric flow. part ii: application to convective boundary layer. *Atmospheric Environment*, 39:1471–1479, 2005b.

M. Cassiani, A. Radicchi, J. D. Albertson, and U. Giostra. An efficient algorith for scalar pdf modelling in incompressible turbulent flows; numerical analysis with evaluation of iem and iecm micro-mixing models. *J. Comput. Phys.*, 223: 519–550, 2007.

I.P. Castro and M. Dianat. Pulsed wire velocity anemometry near walls. *Experiments in Fluids*, 8:343–352, 1990.

CERC. *ADMS-Urban User Guide*. Cambridge Environmental Reasearch Consultants, 2001.

P. C. Chatwin and P. J. Sullivan. The intermittency factor of scalars in turbulence. *Physics of Fluids A*, 1:761–763, 1989.

P. C. Chatwin and P. J. Sullivan. A simple and unifying physucal interpretation of scalar fluctuations measurements from many turbulent shear flows. *Journal Fluid Mechanics*, 212:533–556, 1990.

G. Comte-Bellot. Hot-wire anemometry. *Annual Review of Fluid Mechanics*, 8: 209–231, 1976.

G.T. Csanady. *Turbulent diffusion in the environment*. D. Reidel, Dordrecht, The Netherlands, 1973.

P. De Haan and M. W. Rotach. A novel approach to atmospheric dispersion modelling: The puff-particle model. *Q. J. R. Meteorol. Soc.*, 124:2771–2792, 1998.

J. W. Deardroff and G. E. Willis. A parametrisation of diffusion into the mixed layer. *Journal of Applied Meteorology*, 14:1451–1458, 1975.

L. Djenidi, R. A. Antonia, M. Amielh, and F. Anselmet. A turbulent boundary layer over a two-dimensional rough wall. *Experiments in Fluids*, 44:37–47, 2008.

S. Du and J. D Sawford, B. L. and. Wilson. Estimation of the kolmogorov constant for the lagrangian structure function, using a second order lagrangian model of grid turbulence. *Physics of Fluids*, 7:30833090, 1995.

P. A. Durbin. A stochastic model of two-particles dispersion and concentration fluctuations in homogeneous turbulence. *Journal Fluid Mechanics*, 100:279–302, 1980.

P. A. Durbin. Analysis of the decay of temperature fluctuations in isotropic turbulence. *Physics of Fluids*, 25:1328–1332, 1982.

J. E. Fackrell. A flame ionisation detector for measuring fluctuating concentration. *J. Phys. E: Sci. Instrum.*, 13:888–893, 1980.

J. E. Fackrell and A. G. Robins. The effects of source size on concentration fluctuations in plumes. *Boundary-Layer Meteorology*, 22:335–350, 1982a.

J. E. Fackrell and A. G. Robins. Concentration fluctuations and fluxes in plumes from point sources in a turbulent boundary layer. *Journal Fluid Mechanics*, 117:1–26, 1982b.

P. Franzese. Lagrangian stochastic modeling of a fluctuating plume in the convective boundary layer. *Atmospheric Environment*, 37:16911701, 2003.

P. Franzese and M. S. Borgas. A simple relative dispersion model for concentration fluctuations in contaminant clouds. *Journal of Applied Meteorology*, 41: 1101–1111, 2002.

P. Franzese and M. Cassiani. A statistical theory of turbulent relative dispersion. *Journal Fluid Mechanics*, 571:391–417, 2007.

C. W. Gardiner. *Handbook of stochastic methods for physics chemistry and the natural sciences*. Springer, Berlin, 1983.

J. R. Garratt. *The atmospheric boundary layer*. Cambridge University Press, 1992.

F. Gifford. Statistical properties of a fluctuating plume dispersion model. *Advances in geophysics*, 6, 1959.

D. J. Hall and M. A. Emmott. Avoiding aerosol sampling problems in fast response flame ionisation detectors. *Experiments in Fluids*, 10:237–240, 1991.

J. S. Hay and F. Pasquill. Diffusion from a continuous source in relation to the spectrum and scale of turbulence. *Advances in geophysics*, 6:343–365, 1959.

T. Hilderman and D. J. Wilson. Predicting plume meandering and averaging time effects on mean an fluctuating concentrations in atmospheric dispersion simulated in a water channel. *Boundary-Layer Meteorology*, 122:535–575, 2007.

J. O. Hinze. *Turbulence*. McGraw-Hill, 1975.

H. P. A. H. Irwin. The design of spires for wind simulation. *Journal of Wind Engineering and Industrial Aerodynamics*, 7:361–366, 1981.

P. S. Jackson. On the displacement height in the logarithmic velocity profile. *Journal Fluid Mechanics*, 111:15–25, 1981.

J. Jimènez. Turbulent flows over rough wall. *Annual Reviews Fluid Mechanics*, 36:173–96, 2004.

F. E. Jorgensen. How to measure turbulence with hot-wire anemometers - a practical guide. *Dantec Dynamics*, 2002.

J. C. Kaimal and J. J. Finnigan. *Atmospheric Boundary Layer Flows, their structure and measurement*. Oxford University Press, 1994.

J. C. Kaimal, J. C Wyngaard, J. Izumi, and Cot O. R. Spectral characteristics of surface-layer turbulence. *Quarterly Journal of the Royal Meteorological Society*, 98:563–589, 1972.

Kolmogorov. The local structure of turbulence in incompressible viscous fluid for very large reynolds numbers. *Docklady ANSSSR*, 30:301–304, 1941.

P. A. Krogstad and R. A. Antonia. Structure of turbulent boundary layers on smooth and rough walls. *J. Fluid Mech.*, 277:1–21, 1994.

P. A. Krogstad and R. A. Antonia. Surface roughness effects in turbulent boundary layers. *Experiments in Fluids*, 27:450–460, 1999.

B.J. Legg, P.A. Coppin, and Raupach M.R. A three-hot-wire anemometer for measuring two velocity components in high intensity turbulent boundary layers. *J. Phys. E: Sci. Instrum.*, 17:970–976, 1984.

W. S. Lewellen and W. I. Sykes. Analysis of concentration fluctuations from lidar observations of atmospheric plumes. *J. Clim. Appl. Meteorol.*, 25:1145–1154, 1986.

D. M. Lewis and P. C. Chatwin. A new model probability density function for contaminants dispersing in the atmosphere. *Environmetrics*, 6:583, 593, 1995.

D. M. Lewis, P. C. Chatwin, and N. Mole. Investigation of the collapse of the skewness and kurtosis exhibited in atmospheric dispersion data. *Il Nuovo Cimento*, 20:385–397, 1997.

R. Lien and E. A. D'Asaro. The kolmogorov constant for the lagrangian velocity spectrum structure function. *Physics of Fluids*, 14:44564459, 2002.

L. Lourenco and A. Krothapalli. On the accuracy of velocity and vorticity measurements with piv. *Experiments in Fluids*, 18:421–428, 1995.

A. K. Luhar, M. F. Hibberd, and M. S. Borgas. A skewed meandering plume model for concentration statistics in the convective boundary layer. *Atmospheric Environment*, 34:35993616, 2000.

N. Mole and E.D. Clarke. Relationships between higher moments of concentration and of dose in turbulent dispersion. *Boundary-Layer Meteorology*, 73: 35–52, 1995.

A. S. Monin and A. M. Yaglom. *Statistical Fluid Mechanics*, volume 2. MIT Press, Cambridge, 1975.

L. Mortarini, P. Franzese, and E Ferrero. A fluctuating plume model for concentration fluctuations in a plant canopy. *Atmospheric Environment*, 43:921–927, 2009.

K. R. Mylne and P. J. Mason. Concentration fluctuations measurements in a dispersing plume at a range up to 1000 m. *Quarterly Journal of the Royal Meteorological Society*, 117:177–206, 1991.

H. A. Panofsky and J. A. Dutton. *Atmospheric turbulence: models and methods for engineering applications*. John Wiley & Sons, 1984.

F. Pasquill. Atmospheric dispersion of pollution. *Quarterly Journal of the Royal Meteorological Society*, 97:369–395, 1971.

F. Pasquill and F. B. Smith. *Atmospheric diffusion, third edition*. Ellis Harwood, (John Wiley & Sons) Chichester, 1983, 1983.

A.E. Perry, K.L. Lim, and S.M. Henbest. An experimental study of the turbulence structure in smooth- and rough-wall boundary layers. *J. Fluid Mech.*, 177:437–466, 1987.

D. Poggi, A. Poroprato, and l. Ridolfi. Analysis of the small scale structure of turbulence on smooth and roughwalls. *Physics of Fluids*, 15(1):35–46, 2003.

S. B. Pope. Consistency conditions for random-walk models of turbulent dispersion. *Physics of Fluids*, 30 (8):23742379, 1987.

S. B. Pope. The vanishing effect of molecular diffusivity on turbulent dispersion: implications for turbulent mixing and the scalar flux. *Journal Fluid Mechanics*, 359:299–312, 1998.

J. V. Postma, D. J. Wilson, and E. Yee. Comparing two implementations of a micromixing model. part i: wall shear-layer flows. *Boundary-Layer Meteorology*, 140:207–224, 2011a.

J. V. Postma, D. J. Wilson, and E. Yee. Comparing two implementations of a micromixing model. part ii: canopy flow. *Boundary-Layer Meteorology*, 140: 225–241, 2011b.

M. Raffel, C. Willert, S. Werely, and J. Kompenhans. *Particle Image Velocimetry: A practical guide*. Springer, Heidelberg, 2nd edition, 1998.

M. R. Raupach, R. A. Antonia, and S. Rajagopalan. Rough-wall turbulent boundary layers. *Applied Mechanics Reviews*, 44(1):1, 1991. doi: 10.1115/1.3119492.

M. R. Raupach, D. E. Hughes, and H. A. Cleugh. Momentum absorption in rough-wall boundary layers with sparse roughness elements in a random and clustered distributions. *Boundary-Layer Meteorology*, 120:201–218, April 2006.

A. M. Reynolds. Representation of internal plume structure in giffords meandering plume model. *Atmospheric Environment*, 34:2539–2545, 2000.

U Rizza, C. Mangia, J. C. Carvalho, and D. Anfossi. Estimation of the lagrangian velocity structure function constant c0 by large-eddy simulation. *Boundary-Layer Meteorology*, 120:25–37, 2006.

A. G. Robins. The development and structure of simulated neutrally stable atmospheric boundary layer. *Journal of Industrial Aerodynamics*, 4:71–100, 1979.

P. Salizzoni, L. Soulhac, P. Mejean, and R.J. Perkins. Influence of a two scale surface roughness on a turbulent boundary layer. *Boundary-Layer Meterorol.*, 127(1):97–110, 2008.

B. Sawford. Turbulent relative dispersion. *Annual Reviews Fluid Mechanics*, 33: 289–317, 2001.

B. Sawford. Micro-mixing modelling of scalar fluctuations for plumes in homogeneous turbulence. *Flow, Turbulence and Combustion*, 72:133–160, 2004.

B. Sawford and J. C. R. Hunt. Effects of turbulence structure, molecular diffusion and source size on scalar fluctuations in homogeneous turbulence. *Journal Fluid Mechanics*, 165:373–400, 1986.

B. Sawford and H. Stapountzis. Concentration fluctuations according to fluctuating plume models in one and two dimensions. *Boundary-Layer Meteorology*, 37:89–105, 1986.

H Schlichting and K. Gersten. *Boundary layer theory, 8th edition*. Springer, 2000.

T. P. Schopflocher and P. J. Sullivan. The relationship between skewness and kurtosis of a diffusing scalar. *Boundary-Layer Meteorology*, 115:341–358, 2005.

R.J. Smalley, R.A. Antonia, and L. Djenidi. Self-preservation of rough-wall turbulent boundary layers. *European Journal of Mechanics - B/Fluids*, 20: 591602, 2001.

L. Soulhac, P. Salizzoni, F.-X. Cierco, and R.J. Perkins. The model sirane for atmospheric urban pollutant dispersion; part i, presentation of the model. *Atmospheric Environment*, 45:7379–7395, 2011.

H. Takimoto, A. Inagaki, M. Kanda, A. Sato, and T. Michioka. Length-scale similarity of turbulent organised structures over surfaces with different roughness types. *Boundary-Layer Meteorology*, 147:217–236, 2013.

H. Tennekes. Similarity relations, scaling laws and spectral dynamics. In F.T.M. Niewstadt and H. Van Dop, editors, *Atmospheric turbulence and air pollution modelling*, pages 37–68. D. Reidel Publishing Company, Dordrecht, 1982.

H. Tennekes and J. L. Lumley. *A first course in turbulence*. The MIT Press, 1972.

A. S. Thom. Momentum absorption by vegetation. *Quarterly Journal of the Royal Meteorological Society*, 97:414–428, 1971.

D. J. Thomson. Criteria for the selection of the stochastic models od particle trajectories in turbulent flows. *Journal Fluid Mechanics*, 180:529–556, 1987.

A. A. Townsend. *The structure of turbulent shear flows*. Cambridge University Press, 1976.

D. J. Tritton. *Physical Fluid Dynamics*. Oxford Science Publications, 1988.

F. Vendel, L. Soulhac, P. Mejean, L. Donnat, and O. Duclaux. Validation of the safety lagrangian atmospheric model (slam) against a wind tunnel experiment over an industrial complex area. In *14th Conference on Harmonisation within Atmospheric Dispersion Modelling for Regulatory Purposes*, 2011.

A. Venkatram. Vertical dispersion of ground-level releases in the surface boundary layer. *Atmospheric Environment*, 26:947–949, 1992.

L. Vesely, C. Heaigermoser, D. Greco, and M. Onorato. Turbulent flow and organised motions overa two-dimensional rough-wall. *Physics of Fluids*, 21: 125107, 2009.

E. Villermaux and J. Duplat. Mixing as an aggregation process. *Physical Review Letters*, 91:184501, 2003.

R.O. Weber. Remarks on the definition and estimation of friction velocity. *Boundary-Layer Meteorology*, 93:197–209, 1999.

J.C. Weil. Updating applied diffusion models. *Journal of Climate and Applied Meteorology*, 24:1111–1130, 1985.

J. Westerweel. Fundamentals of digital particle image velocimetry. *Measurement Science and Technology*, 8(12):1379, 1997. doi: 10.1088/0957-0233/8/12/002.

D. J. Wilson, B. W. Zelt, and W. E. Pittman. Statistics of turbulent fluctuation of scalars in a water channel. *Technical report for Defence Research Establishment Suffield (DRES-CR-31-91), Department of Mechanical Engineering, University of Alberta, Edmonton, Alberta, Canada*, 1991.

A. M. Yaglom. Similarity laws for constant-pressure and pressure-gradient turbulent wall flows. *Annual Review Fluid Mechanics*, 11:505–540, 1979.

E. Yee and A. Skvortsov. Scalar fluctuations from a point source in a turbulent boundary layer. *Phys. Review E.*, 84, 2011.

E. Yee and D. J. Wilson. A comparison of the detailed structure in dispersing tracer plumes measured in grid-generated turbulence with a meandering plume model incorporating internal fluctuations. *Boundary-Layer Meteorology*, 94:253–296, 2000.

E. Yee, D. J. Wilson, and B. W. Zelt. Probability distributions of concentration fluctuations of a weakly diffusive passive plume in a turbulent boundary layer. *Boundary-Layer Meteorology*, 64:321–354, 1993.

E. Yee, R. Chan, P. R. Kosteniuk, G. M. Chandler, C. A. Biltoft, and J. F. Bowers. Incorporation of internal fluctuations in a meandering plume model of concentration fluctuations. *Boundary-Layer Meteorology*, 67:11–39, 1994.